University of Alberta

Erbium Fiber Laser Development for

Applications in Sensing

Sunita Sindhu

**A thesis submitted to the Faculty of Graduate Studies and Research
in partial fulfillment of the requirements for the degree of**

**Master of Science
in
Photonics and plasmas**

Department of Electrical and Computer Engineering

To my husband

ABSTRACT

The focus of this dissertation is the development of Erbium doped fiber laser sources for applications in dual pulse LIBS and hydrocarbon sensing in the oil industries. A single channel laser source suitable for the dual pulse LIBS is built and characterized which required both a higher energy ablation pulse and a second narrow linewidth resonant excitation pulse in the near UV wavelength range. For this source a two stage double pass erbium doped fiber amplifier is used to amplify the narrow linewidth laser pulse input from a DFB laser diode. The input pulse with the energy of 0.4 nJ is amplified to 4 µJ in the first stage amplifier and then is further amplified up to an energy of 50 µJ in a second stage amplification. The second stage amplification is carried out with the help of large mode area Er/Yb codoped fiber. The first and second stages of the amplification were thoroughly characterized by studying various parameters under different pump conditions. The frequency upconversion of the amplified laser pulse is carried out with the help of PPLN (frequency doubled) and BBO crystal (frequency quadrupled). The pulse energies of about 50 µJ for the fundamental pulse (1543 nm), 15 µJ frequency doubled (771.5 nm) and 1 µJ frequency quadrupled (385.7 nm) are achieved. The nonlinear effect of stimulated Brillouin Scattering (SBS) was observed and a suitable operating regime was established to avoid deleterious effects of SBS.

A fiber sensor based on the on the principle of Optical Low Coherence Reflectometry (OLCR) was developed based on a low coherence ASE Erbium fiber source. The system was characterized in detail and was tested in the

determination of the refractive index and physical thickness of a few liquid hydrocarbon samples e.g. hexane and chloroform, at the bottom of an industrial high pressure test cell.

Acknowledgements

Table of Contents

_____

List of Tables

LIST OF FIGURES

Acronyms

ASE   Amplified Spontaneous Emission

BBO Bismuth Borate

CCD Charge Coupled Device

CW   Continuous Wave

DFB Distributed Feedback

EDF Erbium doped Fiber

EDFA Erbium doped Fiber Amplifier

EELED Edge Emitting Light Emitting Diode

EYDF Erbium Ytterbium Doped Fiber

FBG Fiber Bragg Grating

FC Fiber Coupler

FWHM Full Width at Half Maximum

fs Femtosecond

GRIN Gradient Index

ICCD Intensified Charged Coupled Device

KDP Potassium Dihydrogen Phosphate

KTP Potassium Titanyl Phosphate

LASER Light Amplification by Stimulated Emission of Radiation

LIBS Laser Induced Breakdown Spectroscopy

LA-LIF Laser Ablation-Laser Induced Fluorescence

LCI Low Coherence Interferometry

LMA Large Mode Area

NA Numerical Aperture

MOPA Master Oscillator Power Amplifier

OLCR Optical Low Coherence Reflectometry

OCT Optical Coherence Tomography

OTDR Optical Time Domain Reflectrometry

PPLN Periodically Poled Lithium Niobate

PM Polarization Maintained

SBS Stimulated Brillouin Scattering

SM Single Mode

CHAPTER 1

INTRODUCTION

The principle of laser action was first demonstrated in 1960 using a crystal of ruby as the laser medium and since then the laser has grown from the status of a scientific curiosity to being the key to applications in a wide range of fields. Lasers have many potential applications in manufacturing industries, are an essential component of communication and holographic systems and the basis of many scientific measurement and research programs. There are different kinds of lasers with quite different characteristics, however all lasers emit radiation with special properties which enables the laser to be used in a much wider range of applications than conventional light sources. By using lasers and spectroscopy it becomes feasible to understand the complex processes occurring in the interactions of laser pulses with matter. Sensors based on lasers have been proved a valuable tool for wide range of applications. Laser Ranging Retro-reflection is used to measure the distance of the moon from the earth to cm accuracy [1]. Lasers can be used for studying the rotation of earth, for counting atoms and in isotope separation. The technique based on the pulsed photoacoustic Raman spectroscopy (PARS) [2] is used to detect the energy deposited in a gas sample by the process of stimulated Raman scattering. The position of distant object can be determined with the help of a range finder in which a signal from a laser switches on a counting circuit and the signal returned from the target terminates the counting. Optical probing of the atmosphere uses lasers for the remote

measurement of atmospheric constituents and conditions including the measurements of traces of pollutant gases, temperature, water etc [1]. The first precision measurement of ozone in the atmosphere was made using laser remote sensing [3]. The ability of laser beams to concentrate high power density of light at a focal point has opened a new path of micro Raman spectroscopic analysis, which can be used for the study of biological and biomedical samples available in very small quantities [1].

One very powerful sensor technique is laser induced breakdown spectroscopy (LIBS) which has been proven as a simple, inexpensive technique in the field of material characterization. It can be used to determine the composition of a sample, regardless of whether the sample is solid, liquid or gas. LIBS is based on the principle of atomic emission spectroscopy. In atomic emission spectroscopy the atoms can be identified by analyzing the radiation emitted by them. In this technique a laser beam is tightly focused onto the target, which causes local heating, intense evaporation and plasma formation. A LIBS system needs a short pulse, moderate to high energy laser source used as an excitation source for the formation of plasma on the surface of the sample.

LIBS was used for the first time for the detection of elemental composition of materials (gases, liquids and solids) during 1960's [4,5]. Since then, LIBS has been proven as a useful technique to determine the elemental composition of different materials. The main feature of this technique is that there is no need of sample preparation for the LIBs which further avoids contamination of the material under investigation and it can be used for any kind

of elements [6, 7]. The most common laser system used for LIBS measurements is the Q-switched Neodymium Yttrium Aluminum Garnett (Nd:YAG) laser (8). Other laser systems commonly used for LIBS measurements include gas lasers (e.g. CO_2 and excimer) and Nd:YAG or flashlamp pumped dye lasers [8]. Long pulse width and CW lasers have been used to cut, drill, modify and mark target materials. However they are not very effective in producing optically emitting plasma without producing large craters and heat affected zones. These limitations can be overcome by replacing these laser sources by short pulse lasers.

LIBS can also be combined with fluorescence spectroscopy in microfluid systems for very promising applications in the medical industry. Smart, portable and rugged LIBS sensors can be developed by replacing the conventional seed laser sources by powerful and miniaturized fiber or microchip laser sources. Due to the optical nature which enables direct non-contact and rapid analysis, LIBS has many advantages and a range of applications [9]. Despite these advantages the LIBS technique suffers from some limitations like its moderate sensitivity and relatively poor limits of detection in comparison to a number of other spectroscopic techniques [10,11]. Several approaches have been proposed to modify the experimental technique to improve the LIBS detection limits. A dual pulse approach has been found most promising as it provides better coupling of laser energy to the target and ablated material, which leads to the more efficient production of atoms in an excited state [12, 13]. In dual pulse LIBS two laser pulses are used for the plasma generation and excitation. In the most sensitive version the first laser pulse is focused onto the sample where it creates plasma and

then the second pulse is tuned to a resonant absorption line of element of interest and the emitted fluorescence spectra is recorded. This technique is called laser ablation-laser induced fluorescence (LA-LIF). Thus a narrow spectral line and tunability of the second laser pulse are the essential features of this dual pulse technique [14]. It has been demonstrated that the use of dual pulse approach enhances the emission intensities and provides lower detection limits [13]. Dual pulse LIBS can be performed by a single laser [15,16], which makes the system more compact and reduces the problems of alignment. In some cases the use of two different lasers has also been reported [17,18,19,20] which provides the flexibility with spatial arrangements of the two laser beams, their pulse energies and the time delay between the two laser pulses. A double pulse approach was first suggested by Piepmeier and Malmstadt [21] and Scott and Strasheim [22]. According to them a large portion of laser energy is absorbed by the plasma plume and the second laser pulse further excites the desired species in plasma. Most of the studies made on LIBS or Dual Pulse LIBS are laboratory based and the apparatus used was very heavy and bulky. So there is a need to transform such laboratory LIBS systems into integrated, lightweight field-deployable sensor systems.

Fibre optic technology offers the potential for designing portable LIBS sensors where fiber optic lasers can generate the required pulses and fibers can be used to collect the light signal and deliver it to the detector/spectrometer. When using miniaturized laser sensors and fibre optics it is possible to develop compact laser sensors for various analytical applications. In field portable LIBS the sample

preparation and off site analysis are unnecessary which makes the measurement less complex. Such smart, portable and rugged LIBS fiber optic sensors require powerful and miniaturized laser sources. During the last few years microchip laser have been used as an attractive alternative where compact and rugged short pulsed laser source are required [23, 24]. Diode pumped passively Q-switched microchip lasers (e.g. Cr^{4+}:Nd^{3+}:YAG laser operating at 1064 nm) are very suitable for spectroscopic applications. But for LIBS we generally need a more powerful laser source which is not possible by using microchip lasers alone. So amplification is necessary for using theses as excitation sources. Because of their excellent thermal properties due to the large surface to volume ratio, rare earth doped optical fiber are superior compared to laser crystals for use as solid state laser oscillators and microjoule to millijoule pulse amplifiers [25, 26]. W. Schade et al [27] reported the use of such small, portable and rugged LIBS fibre optic sensors for the detection of hidden explosives in anti-terror applications. They used a Cr^{4+}:Nd^{3+}:YAG microchip laser as seed laser for a fibre amplifier.

In the present work a powerful and short pulse laser system is developed which can be used in dual pulse LIBS applications. The goal of the present thesis was to develop a fiber laser system for two pulse LA-LIF based on the eye safe Er:fiber laser. The resonant emission lines which can be probed are the fourth harmonic output of the fundamental wavelength which is in the range of 1530-1560 nm. A high repetition rate and energetic fibre laser source with pulse duration of nanoseconds has been developed. For the demonstration of dual pulse LIBS a single laser source system has been used for both matter ablation and

excitation. The laser system is based on a multistage amplification of a narrow spectral line seed pulse from a fiber coupled DFB diode laser. After the first stage amplifier a 20 ns laser pulse with energy of about 4 μJ was obtained which was further amplified up to 50 μJ in a second stage amplifier.

The first stage amplification was carried out with the help of an erbium doped fiber amplifier. Since its invention the erbium doped fiber amplified has been extensively developed due to its compatibility with existing optical fiber transmission system [28]. The advantages of using an EDFA over the semiconductor laser amplifiers are high gain, low insertion loss, polarization insensitivity and low noise figure. These amplifiers are mainly used in the telecommunication industry but they can also be utilized to obtain high energy pulses for micromachining and LIBS. Mears et al [29] demonstrated that EDFA could provide gains as high as 40 dB when pumped in the range of 50-100 MW. EDFAs are made by connecting Er doped fibers with other components e.g pump lasers, isolators, couplers, circulators which are necessary for the amplifier's operation. These components usually have fiber pigtails which make it easier to integrate them in a fiber based system by fusion splicing the fibers together.

The second stage amplification was performed with the help of a large mode area Er/Yb amplifier. Variation of output pulses with repetition rate as well as SBS pulse shortening and its variation with pulse duration and repetition rate were also investigated. In order to obtain the narrow linewidth excitation pulse in the ultraviolet spectral range the output from the second stage amplifier was doubled in a 10 mm long periodically poled $LiNbO_3$ crystal and quadrupled with

the help of a BBO crystal. The laser system developed is made up of all standard telecom components which make the system more robust and relatively inexpensive.

A second laser sensor application area developed in the present thesis is the measurement of the liquid layer thickness and the refractive index in high pressure and high temperature the hydrocarbon condensation measurement systems used by the oil industries. Some applications that exhibit challenges requiring improvements to the existing equipments are lean gas condensate fluids, where the amount of liquid condensation is minimal and the standard equipment does not allow accurate quantification of the accumulated liquid. A fiber sensor working on the principle of optical low coherence reflectometry (OLCR) for measuring phase boundaries and parameters (e.g. refractive index, physical thickness etc) under real industrial conditions has been developed in the present work. Optical low coherence reflectometry is an interferometric technique based on a Michelson type interferometer. This technique allows the measurement of the amplitude and relative distance of the reflected and backscattered light wave with high accuracy. Using the OLCR technique the simultaneous measurement of refractive index and physical thickness of the liquid in a measuring cylinder was carried out with high accuracy. The fiber sensor is suitable for further development for use under the real oil industry conditions.

The rest of the thesis describes the details and results of the systems developed. Chapter 2 describes the background theory of LIBS, fibers lasers and Erbium doped fiber amplifiers. The experimental techniques and details are

presented in chapter 3. Chapter 4 include the experimental results obtained and the discussion of the results for the LIBS system. Chapter 5 describes the development of fiber senor based on the optical Low Coherence Reflectometry used for the measurement of the refractive index and thickness of the liquids. Chapter 6 presents the conclusions and suggestions for future work.

CHAPTER 2

BACKGROUND THEORY

The present chapter describes the background theory of the Laser induced breakdown spectroscopy and dual pulse LIBS which include the laser matter interaction, basic LIBS setup, laser ablation etc. The theory behind the amplification using Erbium doped fiber amplifier is also explained. It includes the rate equation for three level and two level energy description for erbium ions, absorption and emission cross section and amplified stimulated emission. The fundamental theory behind the frequency up conversion and quasi phase matching is also described.

2.1 Laser induced Breakdown Spectroscopy

The first step of LIBS is when a short and powerful laser pulse of high energy density strikes the surface of any material. The surface temperature rises quickly followed by vaporization and ionization. The coupling of the pulse energy occurs through several mechanisms including single and multi-photon absorption, dielectric breakdown, multiphoton ionization and collisional ionization [30,31]. Once the absorbed laser energy exceeds the breakdown threshold of the material, a high density plasma is generated. The dissipation rate of the energy through vaporization is slow relative to the deposition rate. Due to this difference the underlying material reaches critical temperatures and pressures before the surface vaporization. This causes the surface to explode. The plasma formation and the surface ablation takes place in the leading edge of the laser pulse so the rest of the

energy is used to generate luminous plasma. The temperature of the plasma is typically in the range of 10^4 -10^5 K and the electron number density of the atomic emission plume of the order of 10^{15} to 10^{19} cm^{-3} have been reported [32]. The lifetime of the generated plasma-plume may be from a few microseconds to several milliseconds. While LIBS has many advantages over the other atomic emission techniques, the laser matter interaction process is very complex leading to sensitivity to material surface conditions and composition [33, 34, 35].

2.1.1 Laser Ablation

Laser ablation is the removal of a portion of a sample by melting, sublimation, ionization, erosion or explosion. When a high intensity laser pulse is focused onto a sample, the intensity in the focal spot produces rapid heating and intense evaporation followed by plasma formation [36]. The laser pulse energy is coupled with the electrons directly via acceleration in the oscillating electromagnetic field and then to the solid lattice through electron-phonon and electron-ion collisions. Laser ablation results in the formation of a gaseous vapor, luminous plasma and in the production of fine particles from condensation of shock heated material. The laser ablation process is governed by a variety of nonlinear mechanisms. Once the laser beam heats the sample, the material leaves the surface of sample in the form of electrons, ions, atoms, molecules, clusters and particles. Ablation occurs when the energy deposited exceeds the critical temperature for phase transformation from a solid/liquid state to gaseous state, and the sample surface instantaneously vaporizes. When a low fluence laser pulse irradiates a sample, atoms may detach from the surface without detectable surface damage. This phenomenon is called

laser-induced desorption. When the energy absorption is strong enough it leads to breakdown of lattice bonds which is when desorption occurs [36]. However, in many cases, the absorbed energy is delocalized and the neighboring atoms or molecules are vibrationally excited. Upon relaxation, the vibrational energy will be dissipated as thermal energy in the system. On further increase of fluence, the sample reaches its melting threshold and some of the particles in the uppermost layer of the molten material have enough energy to transfer into the vapor phase. Typical laser fluence to initiate desorption is in the range of 10^6 to 10^9 W cm^{-2}. If the fluence is high enough it may lead to ionization and electron heating. Laser photons are first absorbed at the surface and free electrons, ions or atoms are excited. The laser energy is transformed into kinetics energy (for electrons) or electronic and vibrational energy (for atoms, ions and molecule).

The condition for the minimum absorbed irradiance I_{min} (W/cm^2) below which no evaporation occurs is given approximately by [37]:

$$I_{min} = \rho\, L_v\, \left(\frac{\alpha}{t}\right)^{1/2} \qquad (2.1)$$

Where ρ is the mass density of the sample (g/cm^3), α is the thermal diffusivity (cm^2 s^{-1}), t is the pulse duration (s) and L_v is the latent heat of vaporization of the target (J/g). The depth of penetration of heat at time t can be defined as the depth within which the energy of the heated material falls of 1/e of the surface value and is given for the case of ID heat diffusion by [36].

$$D = (4\alpha t)^{1/2} \qquad (2.2)$$

Where α is the thermal diffusivity given by $\alpha = \frac{K}{\rho C}$, where K is the thermal conductivity and C is heat capacity per unit mass.

The temperature at the target rises during the initial laser pulse and the temperature distribution can be calculated using the heat conduction equation [38].

$$\frac{\partial T(x,t)}{\partial t} = \frac{\partial}{\partial x}\left[\left(\frac{k}{C_P\,\rho_S}\right)\frac{\partial T(x,t)}{\partial x}\right] + \frac{\alpha}{C_P\,\rho_S}I(x,t) \qquad (2.3)$$

Where T is the temperature inside the target, x is the distance from the surface. The thermal evaporation rate J_v is the function of surface temperature and it is given as follows [39]:

$$J_v = 1.06X10^6 \exp\left(-\frac{L_v}{k_B}\left(\frac{1}{T_S} - \frac{1}{T_B}\right)\right)\sqrt{\frac{M}{2\pi T_S\,k_B}}\left(\frac{atoms}{s^{-1}}\right) \qquad (2.4)$$

Where L_v is the heat of vaporization and M is the mass of the vapour atoms. k_B is the Boltzmann constant. T_B and T_S is the boiling point temperature and the surface temperature of the sample respectively.

Laser radiation is absorbed primarily by inverse Bremsstrahlung, which involves the absorption of a photon by free electrons during the collision with heavy particles (ions and atoms). The inverse Bremsstrahlung absorption coefficient is given by [39]:

$$\alpha_{IB} = \left[QN_e\,N_o + \frac{4e^6\,\lambda^3 N_e\,Z^2\,N_i}{3h\,c^4 m_e}\left(\frac{2\pi}{3m_e\,k_B T_e}\right)^{\frac{1}{2}}\right]\left[1 - \exp\left(-\frac{hc}{\lambda k_B T_e}\right)\right] \qquad (2.5)$$

Where Q is the cross section for the photon absorption by an electron during the collision with atoms, c is the speed of light, h is the Planck's constant and Z is the charge of the ions. N_e, N_o, and N_i are the number density of electron, atoms and ions, respectively. T_e is the electron temperature. The first term on the right side is the electron atom interaction and second term is the electron ion interaction. After the end of the laser pulse, the plasma induced by the interaction continues to expand into the surrounding atmosphere. In such a case the electron number density and temperature of the plasma decreases as the plasma expands. For the nanosecond time region the later part of the laser pulse can be absorbed by the laser induced plasma which is called plasma shielding and can lead to further heating of the expansion plume. The plasma expansion will depend on the initial plasma properties and the expansion medium. The plasma expansion will be quasi-adiabatic until approximately one microsecond after the laser pulse and after that time line radiation will start to become a dominant energy loss mechanism influencing the temperature decrease. After the end of laser pulse hot electrons, atoms and ions leave the sample surface and the plasma expands. The plasma expansion can be described by the Euler equation of hydrodynamics as given by [38]:

$$\frac{\partial \rho}{\partial t} = -\frac{\partial(\rho v)}{\partial x} \tag{2.6}$$

$$\frac{\partial(\rho v)}{\partial t} = -\frac{\partial[p+\rho v^2]}{\partial x} \tag{2.7}$$

$$\frac{\partial}{\partial t}\left[\rho\left(E_d + \frac{v^2}{2}\right)\right] = -\frac{\partial}{\partial x}\left[\rho v\left(E_d + \frac{p}{\rho} + \frac{v^2}{2}\right)\right] + \alpha_{IB} I \tag{2.8}$$

13

Where ρ is the mass density, v is the velocity, E_d is the internal energy density, and p is the local pressure. This theory is valid for all pulse durations from nanosecond to femtosecond.

When ablation occurs in a gas or liquid environment the ejected mass compresses the surrounding media and produces shockwaves. The ablated mass from the sample interacts with the surrounding media which slows down the expansion of plasma. The expansion and cooling of the ablated mass thus depends also on the properties of surrounding media.

2.1.2 LIBS Setup

In order to perform LIBS the basic components needed are: (1) an energetic short laser pulse source; (2) Optics for laser light delivery and focusing; (3) Optics for capturing the light emitted by the spark and (4) a Spectrometer or detector. Figure 2.1 shows layout of a typical LIBS system. This consists of a pulsed laser source which is focused onto the sample target with the help of focusing lens. Due to laser excitation optical emission takes place which is collected with the help of collection lens. The Spectrometer and detector are used to analyze the emitted radiation in order to determine the elemental composition of the target constituents under investigation. To produce a sufficiently bright plasma a laser power is required which depends on number of factors (i.e. energy, mode quality, wavelength, pulse length, focusing geometry) and the material under investigation [40].
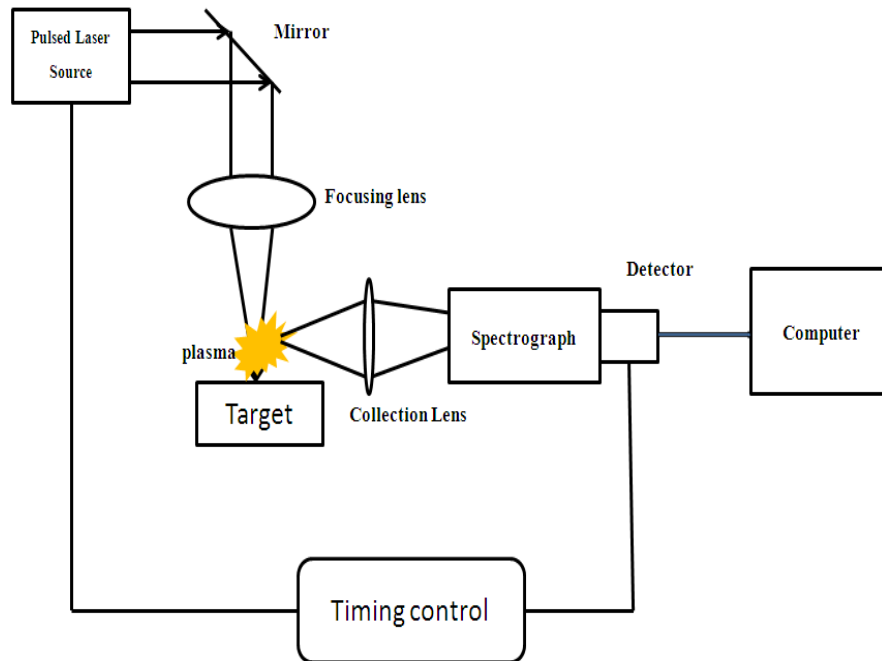
Figure 2.1 LIBS Setup

The typical threshold intensity required for nanosecond pulses is in the range of 10^9 to 10^{11} W/cm^2 (33, 34). The basic function of a laser source for LIBS is to provide sufficient and stable pulse energy to generate the plasma. A review of various laser systems used in LIBS has been reported in [41]. These include the ruby laser (693 nm with pulse duration of 20 ns); gas lasers such as the CO_2 laser (10.6um with a pulse duration of 100 ns) and the excimer lasers (193 nm [ArF], 248 nm [KrF], 308 nm [XeCl] with a pulse duration of 10-20 ns). However the Q-switched Neodymium Yttrium Aluminum Garnett (Nd:YAG) laser is the most commonly used for LIBS. LIBS have been applied under laboratory conditions for various studies. Knoop et al [42] and Caceres et al [43] reported the use of LIBS for the analysis of water and ice. LIBS has also been applied for the study of atmospheric particulars such as aerosols and pollen [44, 45], metal species in

15

plants and coals [46], soils and other natural materials [47]. Recently R.S. Harmon et al [48] demonstrated the application of LIBS for the analysis of Quartz and air under laboratory conditions. With the laser pulses of energy in the range of few mJ, plasma temperature of up to 12000 K can easily be obtained sufficient to ionize the atoms and excite the emission lines [27]. Depending on the applied laser power and the material to be analyzed, decay times are found in the order of several tens of nanoseconds to several microseconds [27].

2.1.3 Dual-pulse LIBS

For high sensitivity laser ablation laser induced-fluorescence LA-LIF a number of factors are required. These include sensing a narrow spectral line and tunability for the second pulse and a minimum ablation pulse energy of the order of 50 µJ for the first ablation pulse [14]. The basic principle of LA-LIF is shown in Figure 2.2.

First intense laser pulse

Second tunable narrow line width laser pulse

$\lambda_{emission}$

λ_{abs}

Plasma generation $\xrightarrow{\text{50 – 500 ns}}$ Plasma expands cools down to an atomic gas

A resonant absorption line is pumped by the second laser pulse
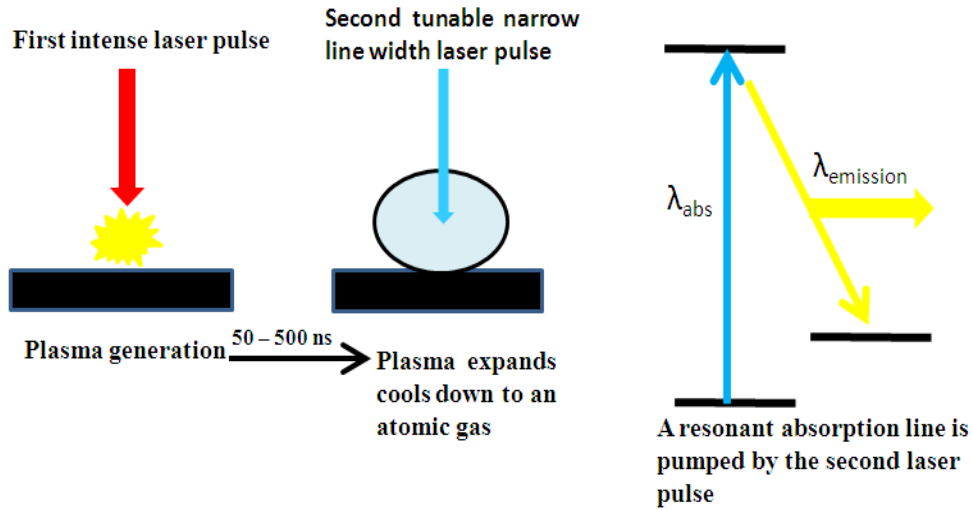
Figure 2.2 Dual Pulse LIBS

The first intense laser pulse is used to create the plasma and the second pulse is tuned to the resonant emission line of the element of interest allowing the emitted fluorescence spectra to be recorded. The element to be examined is excited with a laser pulse often at the wavelength at which the element has its largest cross-section. The excited element will de-excite after some time usually in the range of few ns to μs and emit light at a wavelength greater than the excitation wavelength. The optimal operating conditions, for which the LIF signal can be maximized for the detection of trace element, result from a compromise between the ablation fluence high enough to provide a large number of atoms to be probed, the interpulse delay (long enough for the plasma to cool enough allowing the ground state of atoms to be populated) and the optical arrangement of the experimental setup (maximize the coupling to atomic plume). The excitation laser energy of the order of 1 to 10 μJ has been reported to be enough for providing the fluorescence

signal [14]. The bandwidth of the laser source should be narrow in comparison to the line width of the atomic element of interest. The line width of the element depends on the density and the temperature but typically is much less than 0.1 nm.

The interpulse delay is an important factor in recording the LIF spectra and it should be optimized. When the second pulse intercepts the plasma too early, only a small portion of the analyte could be excited, as most atoms in the hot plasma were either in their ionized or excited state. In addition, the strong background continuum masked the enhanced signal. When the atoms were re-excited too late, the plasma has expanded and thinned out. Also some of the atoms may have combined to form molecules or condense into nanodroplets which no longer would be excited by the probe pulse [14]. The interpulse delay time changes with the change in the energy of the first pulse. A stronger pulse will create hotter plasma which in turn requires a longer time delay to reach optimum probe conditions. The delay time can vary from hundreds of ns to few µs depending on the experimental conditions. Also the resonant beam should not be tightly focused into the plasma in order that a large number of the atoms in the expansion plume are excited to maximize the fluorescence signal.

The use of Dual pulse increases the LIBS performance by directly coupling of second pulse laser energy directly to the target species of interest [14]. It has been demonstrated that the use of dual pulse approach enhances the emission intensities and provides lower detection limits, [14]. In this work a 170 µJ laser pulse was used to ablate a liquid sample in order to measure the lead content. The plasma created was re-excited by a 10 µJ laser pulse tuned to one of

the lead resonant lines. Upon optimization, the 3σ limit of detection was found to be 35±7 ppb. The selective enhancement of Pb using LA-LIF is shown in figure 2.3. The intensifier of the detector was gated on at 300 ns after the ablation with a width of 100 ns. The first excited energy level for aluminum is 25,347 cm^{-1}, whereas for lead it is significantly higher at 35,287 cm^{-1}. Thus by 300 ns the plasma plume had cooled sufficiently that only the easier to excite aluminum lines were excited leading to radiation of emission at 394.4 and 396.2 nm as observed in Figure 2.3(a). The remaining excitation of the lead species was very weak at this time, and no significant lead signal could be observed. However, when a 283 nm pulse re-excited the plasma at 300 ns after the first pulse, the lead signal was strongly enhanced. At the same time, the intensity of the Al 394/396 nm doublet remains constant (Figure 3b). Given that the aluminum species has a smaller upper level energy than lead, this result demonstrates that the enhanced lead signal was purely a resonance effect, while the thermal reheating of the plasma was insignificant.
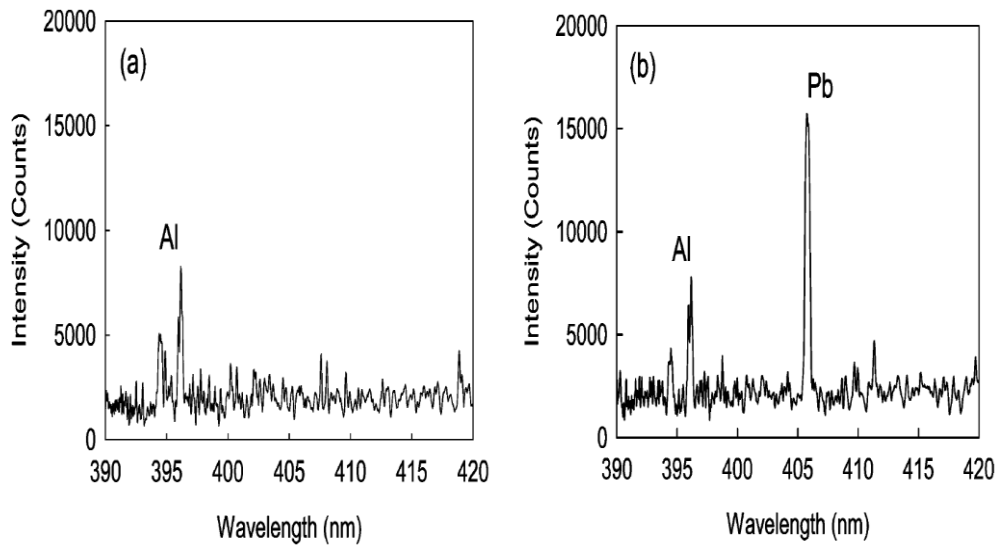
Figure 2.3 Selective enhancement of lead using LA-LIF. The sample contains aluminum and lead as analyte. The spectra were obtained by (a) LIBS and (b) the LA-LIF scheme. Only Pb atoms were excited by the LA-LIF technique [14].

Figure 2.4 shows the two main geometric configurations for the two laser pulses [49,50,51].
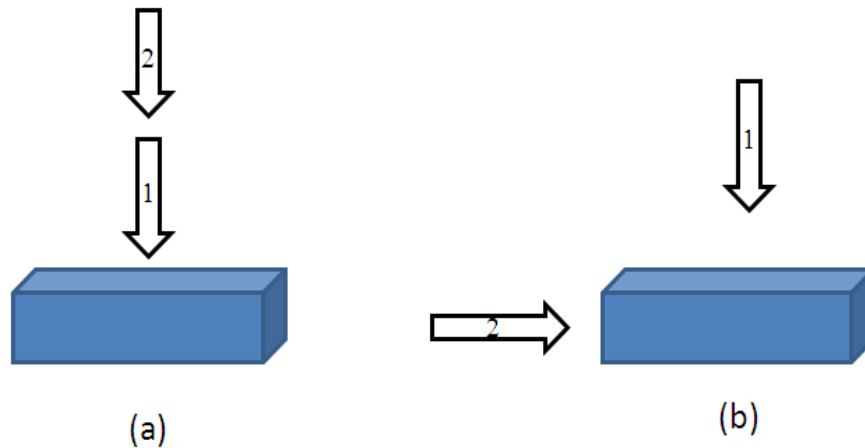
Figure 2.4 Geometric configurations for Dual Pulse LIBS configuration (a) Collinear (b) orthogonal.

In the case of collinear geometry figure 2.4 (a) both laser pulses are focused onto the sample with the same axis of propagation. Using this configuration increase in intensity of emission lines ranging from a factor of 2 up to 100 has been reported [52]. In case of orthogonal configuration Fig 2.4 (b) the first pulse is focused perpendicular to the target which generates plasma and then second pulse is directed orthogonal to the surface. Scaffidi et al [53] studied the dual pulse LIBS with the combination of femtosecond and nanaosecond laser pulses in orthogonal configuration. A large enhancement effect was observed when fs (800 nm) and ns (1064 nm) pulses were combined in the reheating mode. A Q-switched Nd:YAG laser operated at the 1064-nm fundamental wavelength was used to generate 30 mJ pulses with a 7-ns pulse width. When used for ablation the ns pulse was focused with a 50 mm focal length lens. The fs laser was a custom Ti:sapphire system with a 100-fs pulse width, operated at 800 nm. When used for ablation, a 6 mJ 100 fs pulse was focused with a 50-mm focal-length lens. They also suggested that ns-pulses are more effective in the reheating mode. Rai et al [54] used a pair of collinear pulses with an interpulse delay of 2.5 microseconds for detection of Mg in water. The setup consisted of two Q-switched, frequency doubled Nd:YAG lasers and delivered an energy of 300 mJ at 532 nm in 5 ns. Both lasers were operated at 10 Hz during this experiment and were focused on the target. With the addition of second pulse the limit of detection was reduced to 69 ppb in comparison to the 230 ppb with single ns laser pulse. Most of the studies done on Dual pulse LIBS used two pulses of same wavelength, however the use of different wavelength may lead to increase LIBS sensitivity.

St-Onge et al [20] used combination of UV pulse for ablation and an IR pulse for the reheating. UV radiations are found more effective for the material ablation because of reduced plasma shielding for the initial ablation. The IR pulse in turn is absorbed more strongly in the plasma plume leading to efficient heating and excitation of the emission lines.

2.2 Erbium doped Fiber Amplifier (EDFA)

There has always been demand for the high power pulsed laser system for industrial and scientific applications. Fiber lasers and fiber laser amplifiers have been gaining popularity as an attractive option for the pulsed laser systems due to low cost and simple construction. Fiber lasers are a solid state laser which utilizes a doped fiber as the lasing medium. The entire fiber forms the resonator length and it can be coiled or laid in a straight line which makes the packing requirements simplified. Pumping can be carried out by a laser diode where the pump wavelength propagates through the fiber. Fiber based optical amplifier are similar to fiber lasers. The optical amplifiers in the form of optical fibers doped with rare earth ions have gained popularity as suitable choices for signal amplification and as sources of radiation [55, 56]. In this case the input signal propagates through the pumped fiber and is amplified via the stimulated emission. The rare earth doped fibers have been proven to be an attractive gain media for short pulse amplification due to their suitable properties like high optical

efficiency, broad gain bandwidth, compactness, robustness and simplicity of operation [57].

Erbium doped fiber amplifiers have been extensively developed since their invention due to their compatibility with existing optical fiber system [58, 59, 60, 61]. The advantages of using an EDFA over the semiconductor laser amplifiers are high gain, low insertion loss, polarization insensitivity and low noise figure. These amplifiers are mainly used in the telecommunication industry but they can also be utilized to obtain high energy pulses for micromachining and LIBS. Mears et al [29] demonstrated that EDFA could provide gains as high as 40 dB within a pump range of 50-100 mW with low background noise. The preferable pump wavelengths for the EDFA are 980 nm and 1480 nm. 980 nm pumps provide low noise amplifier output but it requires for higher pump laser wavelength accuracy due to the narrow absorption band width while the 1480 nm pump gives better power conversion efficiency as compared to 980 nm band [62]. The pump energy excites the ions to the upper energy state and light emission occurs when the ions drop down to their lower state either by spontaneous emission or by stimulated emission. In spontaneous emission atoms return to lower state randomly and the emission leads to noise generated by the amplifier which is called amplified spontaneous emission (ASE). On the other hand stimulated emission provides the amplification of input signal.

2.2.1 Rate Equation Model for EDFA

Optical fibers are optical waveguides usually made up of silica either in pure form or with some dopants. In comparison to other waveguides fibers can be very long and flexible. The propagation of light through the fiber is based on the phenomenon of total internal reflection. Generally an optical fiber has a core surrounded by cladding. The refractive index of the cladding, n_2, is slightly lower than that of the core n_1. Such fibers are called step index fibers which are different from the graded index fibers, in which the refractive index of the core decreases gradually from the center to the core boundary. There are two important parameters of fiber called numerical aperture (NA) and fiber V number. The numerical aperture represents the light gathering capacity of any fiber and it is represented as below:

$$NA = n_1 \left[\frac{2(n_1 - n_2)}{n_1} \right]^{1/2} \tag{2.9}$$

The V parameter determines the number of modes supported by fiber and is given as:

$$V = a\, k_o NA \tag{2.10}$$

Where $k_0 = 2\pi/\lambda_0$, a is the core radius, λ_0 is the wavelength of light. One can also calculate acceptance angle of the fiber which is given by $\theta_a = \sin^{-1} NA$.

The signal loss in fiber can be defined as the ratio of the power injected into the fiber from an optical source (P_i) to the power received at the fiber end (P_o). The signal attenuation per unit length is commonly described as follows:

$$Loss = \left(\frac{10}{L}\right) \log \left(\frac{P_i}{P_o}\right) \text{(dB/km)} \qquad (2.11)$$

The most common rare earth ions used as dopant are Neodymium (Nd^{3+}) and Erbium (Er^{3+}). These kinds of optical fibers can be fabricated by the vapour deposition of rare earth at high pressure or by the impregnation and diffusion of rare earth doped solutions followed by drying [63]. Generally the concentration of rare earth materials is less than that of classical dopants [(300-1000) ppb]. The rare earth doped fiber characteristics were first studied and demonstrated in 1962 [64] and the Erbium doped fiber was first investigated by Mears and Payne [65] in 1987. Later many studies were done on the Erbium doped fiber and the first EDFA was commercialized in 1992. Er^{3+} is the ion of choice for lasing and amplification in the 1.5 µm region. Figure 2.5 shows the possible energy levels for Erbium ions as well as possible pumping bands.

19455 cm^{-1}, $^2H_{11/2}$

514nm

18797 cm^{-1}, $^4S_{3/2}$

532nm

14925 cm^{-1}, $^4F_{9/2}$

670nm

12500 cm^{-1}, $^4I_{9/2}$

800nm

10204 cm^{-1}, $^4I_{11/2}$

980nm

6756 cm^{-1}, $^4I_{13/2}$

Stimulated
emission

Spontaneous
emission

1480nm

0, $^4I_{15/2}$
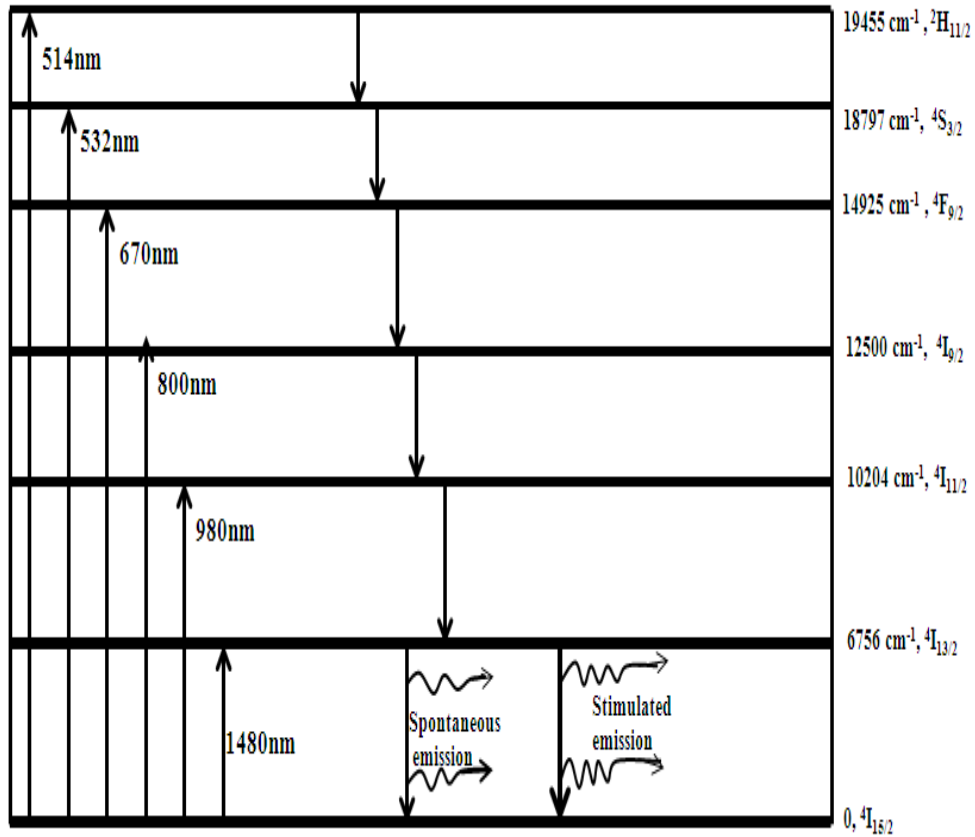
Figure 2.5: Energy Level diagram of Er^{3+} ions [63]

Erbium ions are excited to higher energy levels by absorbing photons from the pump source. From the higher energy levels the ions dissipate energy by releasing photons or converting energy into heat. As shown in figure 2.5 the energy levels are separated by energy gaps, which follow the laws of quantum physics. Energy level E1 ($^4I_{15/2}$) is the ground level and E2 ($^4I_{13/2}$) indicates the first energy level. According to ion energy structure, each energy level has a numbers of stark levels due to the local ion electric fields. Each ion experiences a different local field strength and orientation due to randomness in the glass molecular structure,

resulting in different stark splitting. The splitting causes the large gain bandwidth of rare earth doped fiber amplifier. The number of stark split lines for each level is 7 and 8 for $^4I_{13/2}$ and $^4I_{15/2}$, respectively resulting in 56 possible transitions between those lines spreading across the 1550 nm band at low temperature. As temperature increases the bands overlap and give smooth and continuous transitions. Amplification takes place due to the stimulated emission process in which a photon having energy equal to the energy difference between the two energy levels causes the atom to return to lower energy level along with the creation of another photon, which adds to the electromagnetic wave in constructive manner causing amplification. In case of Er the upper level of the amplifying transition $^4I_{13/2}$ is separated by a large gap from the next lowest level so its life time is very long and mostly radiative. Typically the lifetime is around 10 ms and it depends on the host material and erbium concentration. This long lifetime permits the inversion of the population between the two levels with a moderately weak and thus easy to realize pump source. The glass composition has an important effect on the lifetimes, radiative and nonradiative, of the excited states of Er^{3+}.

One can describe the operation of the EDFA in terms of the pump level and two lasing levels. Level 1 is the ground level, level 2 is the metastable upper laser level having lifetime τ, and level 3 is the pump level. An energy level diagram for this system is shown in figure 2.6.
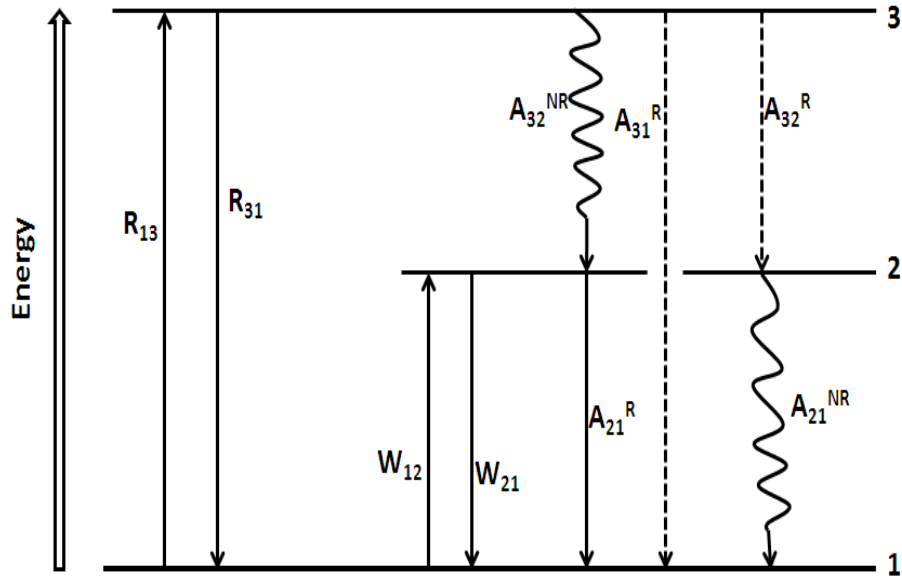
Figure 2.6 Three level energy system [63]

R_{13} is the pumping rate from level 1 to level 3 and stimulated emission rate between levels 3 and 1 is R_{31}. From the level 3 there are two possible ways of decay, i.e radiative and nonradiative (rate A_{32}^{NR}). W_{12} and W_{21} are the stimulated absorption and emission rates between level 1 and level 2. The combined spontaneous radiative and nonradiative decay from the excited state, i.e level 2 is $A_2 = A_{21}^R + A_{21}^{NR}$ where A_{21}^R and A_{21}^{NR} are the radiative and non radiative rates respectively. The spontaneous decay rates from level 2 and level 3 can be simplified as A_{21} and A_{32}.

The fluorescence lifetime τ is given by $\tau = 1/ A_{21}^R$ and. Let N_1, N_2 and N_3 be the fractional densities of populations of the atoms in level 1, 2 and 3 respectively and ρ is the total laser ion density. Therefore

$$\rho = N_1 + N_2 + N_3 \tag{2.12}$$

The atomic rate equations corresponding to these populations can be written as [63]:

$$\frac{dN_1}{dt} = -R_{13}\,N_1 + R_{31}\,N_3 - W_{12}\,N_1 + W_{21}\,N_2 + A_{21}\,N_2 \tag{2.13}$$

$$\frac{dN_2}{dt} = W_{12}\,N_1 - W_{21}\,N_2 - A_{21}\,N_2 + A_{32}\,N_3 \tag{2.14}$$

$$\frac{dN_3}{dt} = R_{13}\,N_1 - R_{31}\,N_3 - A_{32}\,N_3 \tag{2.15}$$

For the steady state condition $\frac{dN_i}{dt} = 0$ and assuming that $a = R_{31} + A_{32}$ and $b = W_{21} + A_{21}$ we get the following simplified form:

$$W_{12}\,N_1 - b\,N_2 + A_{32}\,N_3 = 0 \tag{2.16}$$

$$R_{13}\,N_1 - a\,N_3 = 0 \tag{2.17}$$

By putting $N_3 = \rho - N_1 - N_2$ and solving for N_1 and N_2 we get

$$N_1 = \rho\,\frac{ab}{b(a+R_{13}) + W_{12}\,a + R_{13}\,A_{32}} \tag{2.18}$$

$$N_2 = \rho\,\frac{R_{13}\,A_{32} + W_{12}\,a}{b(a+R_{13}) + W_{12}\,a + R_{13}\,A_{32}} \tag{2.19}$$

The pump level population is assumed to be negligible due to the fast nonradiative decay (A_{32}) toward the metastable level 2 and therefore

$$N_3 = 0 \tag{2.20}$$

By putting back the values of a and b and assuming that the nonradiative decay rate dominates over the pumping rates $R_{13, 31}$, i.e $A_{32} \gg R_{13, 31}$, we get

$$N_1 = \rho \, \frac{1 + W_{21}\tau}{1 + R_{13}\tau + W_{12}\tau + W_{21}\tau} \tag{2.21}$$

$$N_2 = \rho \, \frac{R_{13}\tau + W_{12}\tau}{1 + R_{13}\tau + W_{12}\tau + W_{21}\tau} \tag{2.22}$$

As expected one finds that $N_3 = \rho - N_1 - N_2 = 0$. Examples of pump wavelengths in this case are 980 nm, 800 nm, 650 nm and 540 nm.

In certain pumping configuration, especially in the case of 1480 nm, level 3 can be identical to level 2. So the three level energy system can be reduced to two level system where ground level is represented by level 1 and the metastable level as level 2 with a direct pump rate of R_{12}. The energy level diagram of three level system can be simplified to two level system as shown in Figure 2.7.
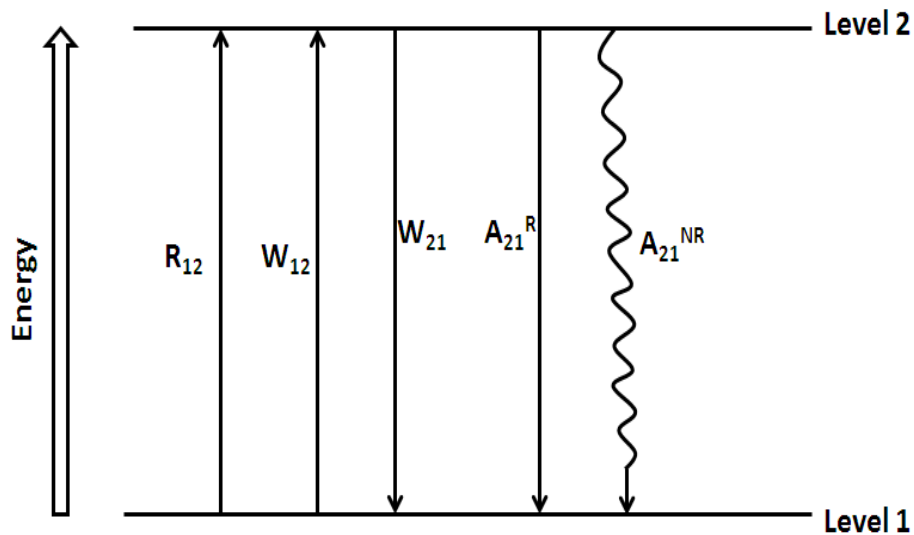
Figure 2.7: Two level Energy System [66]

The corresponding equations of population for the two level system are given as:

$$N_1 = \rho \, \frac{1 + W_{21}\tau}{1 + R_{12}\tau + W_{12}\tau + W_{21}\tau} \tag{2.23}$$

$$N_2 = \rho \, \frac{R_{12}\tau + W_{12}\tau}{1 + R_{12}\tau + W_{12}\tau + W_{21}\tau} \tag{2.24}$$

Codoping of Er^{3+} fibers with Yb^{3+} ions can significantly increase the extractable output power of such lasers and amplifiers by improving the pump absorption near 915 and 975 nm [67]. An EYDF utilizes co-dopant ytterbium ions as an intermediate medium for pump energy transfer to erbium ions for stimulated emission as shown in figure 2.8. In this system the Yb ions are first pumped at the absorption wavelength of 800-1100 nm to the $^2F_{5/2}$ state [68]. Then the energy of Yb ions is transferred to Er ions, which are excited to the $^4I_{11/2}$ state. These excited erbium ions undergo a non-radiative transition to the $^4I_{13/2}$ metastable state and form a population inversion with the $^4I_{15/2}$ state. An incident optical signal travelling through the fiber is amplified via stimulated emission between these two states.

$^2F_{5/2}$ (10245cm^{-1})

Energy Transfer

$^4I_{11/2}$ (10204 cm^{-1})

$^4I_{13/2}$ (6756 cm^{-1})

1.55μm Stimulated Emission

$^2F_{7/2}$

Yb^{3+}

Er^{3+} $^4I_{15/2}$
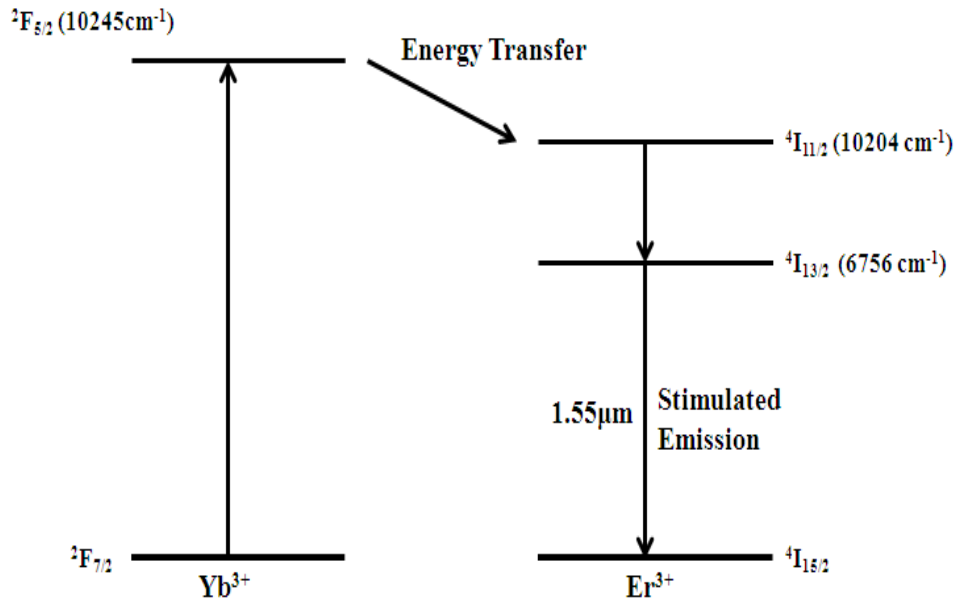
Figure 2.8 Energy levels in an EYDF

In comparison to EDF, an EYDF can achieve the same signal amplification with higher pump efficiency by using a shorter length of fiber [68]. Co-doping of Er fibers with Yb ions has also some drawbacks. Due to imperfect energy transfer process there is an unwanted spontaneous emission from excited Yb^{3+} ions in the 1μm wavelength range which is the main power-limiting factor in the Er/Yb co-doped sources [67]. In the presence of relatively high pumping power the broadband ASE tends to transform into unstable parasitic lasing or even self pulsing. This can further lead to unstable amplifier operation, gain reduction or even to active fiber damage due to giant pulse formation.

2.2.2 Absorption and Emission Cross Sections

Cross sections quantify the ability of an ion to absorb and emit light. In simple words the cross section of a particular transition between two states of an ion represents the probability for that transition to occur with the concurrent emission or absorption of light. The absorption and emission cross sections may be related to the fluorescence and absorption bandwidths, provided the spontaneous lifetime and level degeneracy are also known. The emission and absorption cross sections can be expressed as follows [69]:

$$\sigma_{21} = \frac{\lambda^2}{8\pi n^2} A_{21} \, g(\nu) \tag{2.25}$$

$$\sigma_{12} = \frac{g_2}{g_1} \frac{\lambda^2}{8\pi n^2} A_{21} \, g'(\nu) \tag{2.26}$$

Where λ is the wavelength of peak emission-absorption, $g(\nu)$ and $g'(\nu)$ are the normalized line shape functions for emission and absorption. A_{21} is the spontaneous decay rate and is equal to the inverse fluorescence lifetime. n is the refractive index and g_1 and g_2 are the level degeneracies.

The Fuchtauer-Ladenberg approach [69] was used in the first studies to calculate the cross sections for erbium-doped silica fibers, but later it was observed that the emission cross sections calculated did not agree well with the experiment [66]. A more adequate treatment for calculating the absorption and emission cross sections was provided by the McCumber theory [66].

The spectrum of Er^{3+} in the 1550 nm region mainly depends on the host glass. The peaks and valleys in the spectra have different shapes based on the location of stark levels, the intensities of the transitions between the Stark levels and on the amount of homogenous and inhomogeneous broadening of these levels. The absorption cross-section can be obtained by the simple normalized absorption measurements on a homogenous bulk glass sample. The emission cross section is relatively difficult to calculate. The emission cross section can be determined by two ways either calculating from the absorption cross section or directly measuring the small gain in a short piece of uniformly inverted Er^{3+} doped fiber. An accurate way to calculate emission cross section from the absorption cross section can be obtained through the McCumber relationship. According to McCumber the thermal equilibrium can be reached within a multistate manifold in a time short compared to overall lifetime of the manifold. This case is true in most cases, especially for that of the Er^{3+} $^4I_{13/2}$ to $^4I_{15/2}$ transitions. The McCumber relationship is given as [70]:

$$\sigma_{21} = \sigma_{12}\ e^{(\varepsilon - h\nu)/kT} \hspace{3cm} (2.27)$$

Where σ_{21} is the emission cross section and σ_{12} is absorption cross section. And ϵ represents the mean energy of the $^4I_{13/2}$ to $^4I_{15/2}$ transition. This relation shows that the emission and absorption cross sections are equal only at one frequency corresponding to the mean energy ϵ. For frequencies higher than the crossing point, the absorption cross section is larger than the emission cross section and

vice versa for frequencies below the crossing point. This has been verified experimentally in case of Er^{3+} [66].

Miniscalco's and Quimby [71] used the McCumber theory to determine the absorption and emission cross sections in their work. The experimental results obtained were in good agreement with the theory as shown in figure 2.8.
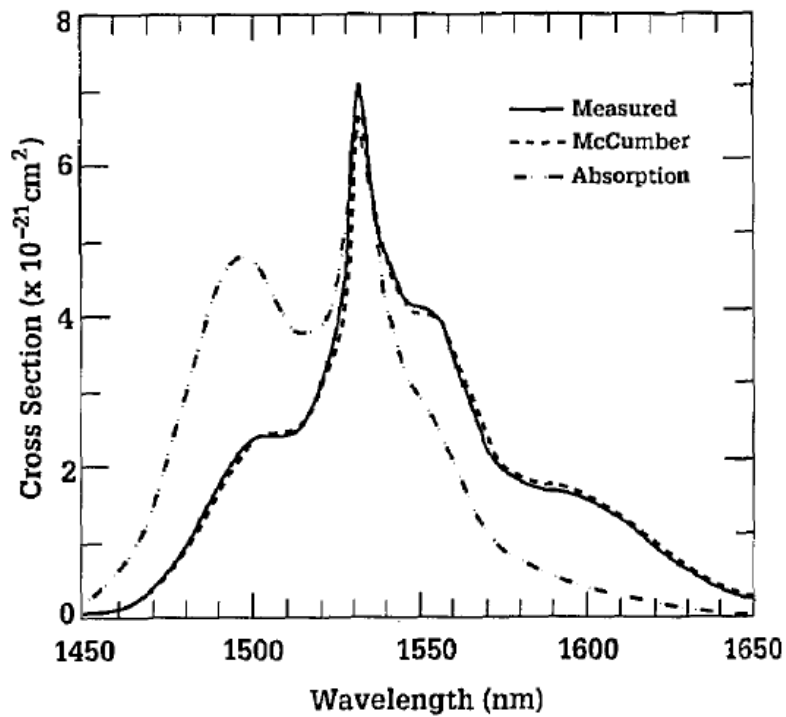
Figure 2.9: Comparison of the shape of the measured stimulated-emission cross section with that calculated from the absorption cross section using the McCumber theory. The absorption spectrum used is also included [71].

The ratio of absorption and emission cross sections at a particular frequency is important in determining the gain for a piece of fiber with a given inversion.

Table 2.1 shows the absorption and emission cross-sections for various hosts for the transitions between the levels $^4I_{13/2} \leftrightarrow {}^4I_{15/2}$.

Host Glass	Wavelength (nm)	Peak Absorption cross section ($\times 10^{-21}$ cm^2)	Peak Emission cross section ($\times 10^{-21}$ cm^2)
Al-P silica	1531	6.60	5.70
Silicate L-22	1536	5.80	7.27
Fluorophosphate L11	1533	6.99	7.16
Fluorophosphate L14	1532	5.76	5.79
Fluorozirconate F88	1531	4.98	4.95
GeO$_2$-SiO$_2$	1530	7.9±0.3	6.7±0.3
Al$_2$O$_3$- SiO$_2$	1530	5.1±0.6	4.4±0.6
GeO$_2$- Al$_2$O$_3$-SiO2	1530	4.7±1	4.4±1

Table 2.1 Peak absorption and emission cross sections for $^4I_{13/2} \leftrightarrow {}^4I_{15/2}$ transition in Er^{3+} at the indicated wavelengths for various glass hosts [66].

2.2.3 Amplified Spontaneous Emission

Another important factor in the case of Erbium doped fiber amplifier is the spontaneous emission of photons. In spontaneous emission the excited ions spontaneously relax from the upper state to the ground state by randomly emitting a photon that is uncorrelated with the signal photons. These emitted photons are amplified along with the signal while travelling through the fiber and stimulate the emission of more photons uncorrelated with the original signal. This parasitic process can occur at any frequency within the fluorescence spectrum of the amplifier transitions and reduces the gain of the amplifier. It is usually referred as ASE (amplified stimulated emission) which limits the total gain available from the amplifier. The ASE can travel in both directions i.e copropagating and counterpropagating with the pump. The backwards ASE at Z=0 is more intense in comparison to the forward ASE at Z=L because the starting section of the fiber with a forward pump is more inverted than the end section.

2.2.4 Configurations of EDFA

To date EDFAs have been studied in various configurations which can be single stage EDFA and Cascaded EDFA. In the single Stage EDFA only one EDF is used as an active material. The single stage geometry can be further divided as single pass and double pass EDFA. Fig 2.10(a) and 2.10(b) show the single pass and double pass configuration for single stage EDFA.
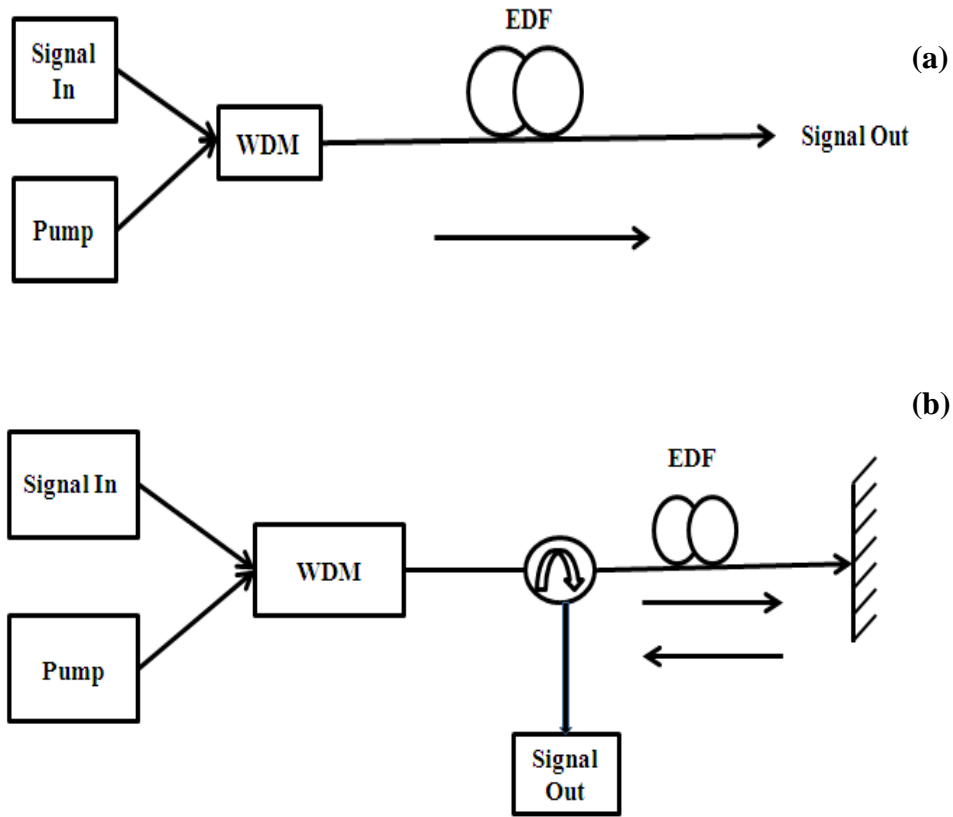
Figure 2.10 EDFA Configurations: (a) Single stage single pass (b) Single stage double pass.

In the single pass configuration the signal passes only once through the active medium (EDF). A WDM (wavelength division multiplexing) combiner can be used to combine the pump and input signal. All the components have single mode fiber pigtails and are spliced together. Fig.2.10 (b) shows the double pass configuration and in this the signal passes two times through the active material.

For the double pass, some reflecting surface is needed to reflect the signal back so that it can again pass through the EDF. Rosolem et al [72] demonstrated the double pass configuration by using a single commercial EDFA for S-band [1490-1520 nm] applications. Naji et al [73] showed that the double pass EDFA gives a better performance for small signal input powers of less than 3 µW and the single pass EDFA performs better for higher signal powers of greater than 3 µW. Cascaded stage amplifiers can be obtained by combining two stages of EDFA or three stages of EDFA. Hidehiko Takara et al [74] reported the highly efficient amplification of ultrashort optical pulses with a two stage Er doped optical fiber amplifier that included an optical gate to effectively reduce the ASE. A gain of 49 dB, an amplified peak power of 105 W and 1.05 nJ pulse energy was achieved. The generation of high peak power pulses using a cascade of three stage erbium doped fiber amplifiers has been reported by B Desthieux et al [75]. The cascade amplifier chain consisted of two high efficiently single mode EDFAs followed by a multimode EDFA. A polarization independent isolator and an acousto-optic modulator were used for the ASE isolation between the different stages. At low repetition rates, peak powers of 111 kW and energies of 0.5 mJ were obtained.

Also EDFAs can be differentiated on the basis of coupling of the pump into the fiber. Three different configurations are shown in figure 2.11.
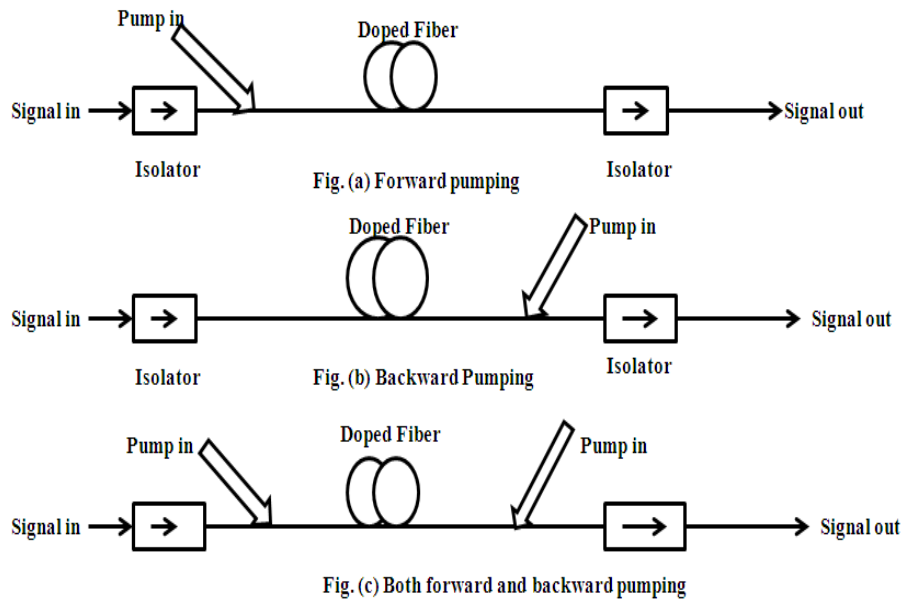
Figure 2.11 Schematic of EDFA configuration utilizing (a) forward pumping, (b) backward pumping, and (c) both forward and backward pumping [63].

Figure 2.11(a) shows the forward pumping configuration in which both pump and signal move in the same direction i.e. forward direction through the doped fiber. This configuration is also called co-propagating configuration. The forward pumping provides better noise performance. In the backward pumping scheme figure 2.11 (b), the pump light and signal travel in opposite direction and it is also known as counter propagating configuration. This arrangement provides higher gain and higher saturation power. Figure 2.11 (c) shows the bidirectional configuration which is more complicated but it can provide the advantages of both backward and forward pumping.

2.2.5 Characteristics of Erbium doped Fiber Amplifier

The performance of EDFA is defined by the amplifier gain, saturation and noise properties. In ideal conditions the EDFA should provide the highest gain possible (with the pump power available), have the highest saturation output power and lowest noise possible. There are several physical effects and device constraints which can limit the performance of EDFA. The most important limitation is the principle of energy conservation i.e the maximum signal energy that can be extracted from the fiber amplifier cannot be more than the pump energy that is stored in it. For a CW, i.e steady state laser, the energy conservation principle can be expressed in the terms of photons flux (number of photons per second) given as below [63]:

$$\Phi_S{}^{out} \leq \Phi_P{}^{in} + \Phi_S{}^{in} \tag{2.28}$$

Where $\Phi_P{}^{in} = P_P{}^{in}/ h\nu$ is the input pump photon flux, and $\Phi_S{}^{in,out} = P_S{}^{in,\ out}/ h\nu$ is the flux of the signal photons input and output from the amplifier. $P_P{}^{in}$, $P_S{}^{in}$ and $P_S{}^{out}$ are the powers of input pump, input signal and output signal respectively.

The inequality in the equation reflects the fact that not all the pump photons are converted into signal photons by the amplifier which is due to several possible effects: (a) some photons can be absorbed; (b) pump photons can be lost due to various causes and (c) a fraction of the pump energy is lost due to spontaneous emission and is not converted into signal energy. The equality means

that all the pump photons absorbed are converted into signal photons by the amplifier. The above equation can be written in terms of power as follows:

$$P_S^{out} \leq P_S^{in} + (\lambda_P / \lambda_S) \, P_P^{in} \qquad (2.29)$$

It is clear from the above equation that the maximum output signal power extracted from the amplifier depends on the wavelength ratio of pump to signal. For any pumping scheme we have $\lambda_P < \lambda_S$ and generally we have $(P_S^{in} / P_P^{in}) \ll 1$ that means $(P_S^{out} / P_P^{in}) < 1$ i.e the power conversion efficiency is less than unity. The power conversion efficiency depends on the pump bands and the highest value is theoretically obtained with the two level pumping scheme, where the ratio λ_P / λ_S is the closest to unity. We can write the above equation in terms of amplifier gain G as follws:

$$G = P_S^{out} / P_S^{in} \leq 1 + (\lambda_P / \lambda_S)(P_P^{in} / P_S^{in}) = 1 + (\Phi_P^{in} / \Phi_S^{in}) \qquad (2.30)$$

This equation implies that the maximum possible amplifier gain corresponds to the regime where each pump photon is converted into one signal photon.

The Gain $G \rightarrow 1$ for $P_S^{in} \gg (\lambda_P / \lambda_S) \, P_P^{in}$, which corresponds to a condition of saturated gain medium transparency.

The upper limit for the amplifier gain can be reached only if all pump photons are actually absorbed by the amplifying medium. The absorption by amplifying medium is limited by the finite number of rare earth ions existing in the medium. The maximum signal gain for a three level laser medium of length L is given by the small signal gain

$$G = P_S^{out} / P_S^{in} = \exp(\sigma_e N_2 L) \qquad (2.31)$$

Where σ_e is the emission cross section and N_2 is the concentration of rare earth ions in the excited state in the condition of full inversion. In conclusion the maximum possible amplifier gain and the output signal power are given by

$$G \leq \min \{\exp(N_2 \sigma_e L), 1 + (\lambda_P / \lambda_S)(P_P^{in} / P_S^{in})\} \qquad (2.32)$$

$$P_S^{out} \leq \min \{P_S^{in} \exp(N_2 \sigma_e L), P_S^{in} + (\lambda_P / \lambda_S) P_P^{in}\} \qquad (2.33)$$

2.3 Frequency Upconversion:

Non-linear properties in the optical region have been demonstrated the first time by harmonic generation by Franken and coworkers in 1961 [76]. They focused a ruby laser with a wavelength 694 nm into a quartz sample and they got output of ultraviolet light with twice the frequency of the ruby laser. Nonlinear optical phenomena are called "nonlinear" because they occur when the response of a material system to an applied optical field depends in a nonlinear manner on the strength of the optical field. In order to describe the phenomenon in more detail let us consider the relation between dipole moment per unit volume, or polarization *P(t)*, of a material system and the strength *E(t)* of an applied optical field given as

$$P(t) = \epsilon_0 \chi E(t) \qquad (2.34)$$

Where χ is called the polarizability or dielectric susceptibility of the medium and ϵ_0 is the permittivity of free space. With high intense laser radiation this relation needs to be generalize as follows;

$$P = \epsilon_0 \left(\chi^{(1)} E + \chi^{(2)} E^2 + \chi^{(3)} E^3 + \text{----------} \right) \qquad (2.35)$$

Where $\chi^{(1)}$ is same as χ and the quantities $\chi^{(2)}$ and $\chi^{(3)}$ are known as the second- and third-order nonlinear optical susceptibilities. If the field is low then only the first term need be considered as was the case before the invention of the laser and for this reason the description of optics before the laser was known as linear optics. As the electric field strength is increased the higher order terms becomes more significant. A nonlinear medium is a medium whose polarization is described by the equation 2.35. Let us consider

$$E = E_0 \cos\omega t \qquad (2.36)$$

By putting this value in Eqn.2.36 we get

$$P = \epsilon_0 \chi^{(1)} E_0 \cos\omega t + \epsilon_0 \chi^{(2)} E_0^2 \cos^2\omega t + \epsilon_0 \chi^{(3)} E_0^3 \cos^3\omega t + \text{- - - - - -} \qquad (2.37)$$

Using the trigonometric relations we get

$$\cos^2\omega t = (1+\cos 2\omega t)/2; \text{ and } \cos^3\omega t = (\cos 3\omega t + 3\cos\omega t)/4 \qquad (2.38)$$

We get

$$P = \tfrac{1}{2} \epsilon_0 \chi^{(2)} E_0^2 + \epsilon_0 (\chi^{(1)} + \tfrac{3}{4} \chi^{(3)} E_0^2) E_0 \cos\omega t +$$

$$\tfrac{1}{2} \epsilon_0 \chi^{(2)} E_0^2 \cos 2\omega t + \tfrac{1}{4} \epsilon_0 \chi^{(3)} E_0^3 \cos 3\omega t + \text{-----} \qquad (2.39)$$

The first term is a constant term which represents the dc electric field in the medium. The second term is the linear polarization; the third term oscillates at frequency 2ω and is called the second harmonic polarization and the fourth one is called third harmonic and so on. Second harmonic generation is also called

frequency doubling in which photons interacting with a nonlinear material are combined to form new photons with twice the frequency. In most crystalline materials, the nonlinear polarizability $\chi^{(2)}$ depends on the direction of propagation, polarization of the electric field and the orientation of the optic axis of the crystal. In such crystalline materials the vectors P and E are not necessarily parallel the coefficient χ must be treated as tensors and we get a relation as given below:

$$P_i^{(2)} = \epsilon_0 \sum \chi_{ijk}^{(2)} E_j E_k \qquad (2.40)$$

Where i, j, k represents the coordinates x,y,z.

Because of symmetry second harmonic generation can't occur in an isotropic medium such as liquids or gases or in centro-symmetric crystals. In the case of anisotropic crystals such as uniaxial crystals both quadratic and cubic terms are present. However the cubic term can generally be neglected in comparison of second order term and we can write:

$$P = \epsilon_0 \chi^{(1)} E + \epsilon_0 \chi^{(2)} E^2 \qquad (2.41)$$

And the medium is said to have second order linearity. The efficiency of second harmonic generation not only depends on the intensity of the excited radiation but also on its direction of propagation in crystals. The phase relationship between fundamental frequency and generated harmonics is very important [77,78]. Let us consider a plane wave and second harmonic wave that are propagating along a material of length L in the z direction as shown in Fig. 2.12.
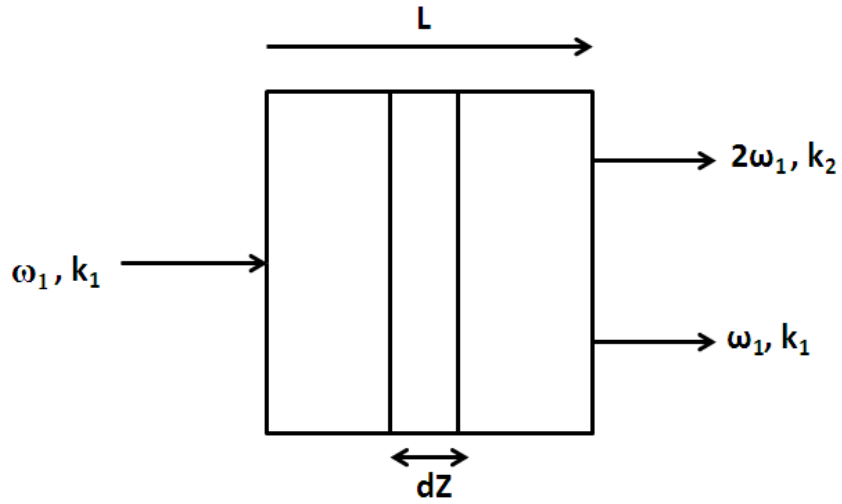
Figure 2.12 Second Harmonic generation

The second harmonic generation efficiency of the material can be expressed as below [1]

$$\eta \propto \frac{\sin^2(\frac{2k_1 - k_2)L}{2})}{(\frac{2k_1 - k_2}{2})^2} \tag{2.42}$$

It is clear from the equation 2.43 that the conversion efficiency will be maximum when the term

$\frac{\sin^2(\frac{2k_1 - k_2)L}{2})}{(\frac{2k_1 - k_2}{2})^2}$ is maximum. Figure 2.13 shows the variation of second harmonic

efficiency with $2k_1 - k_2$.
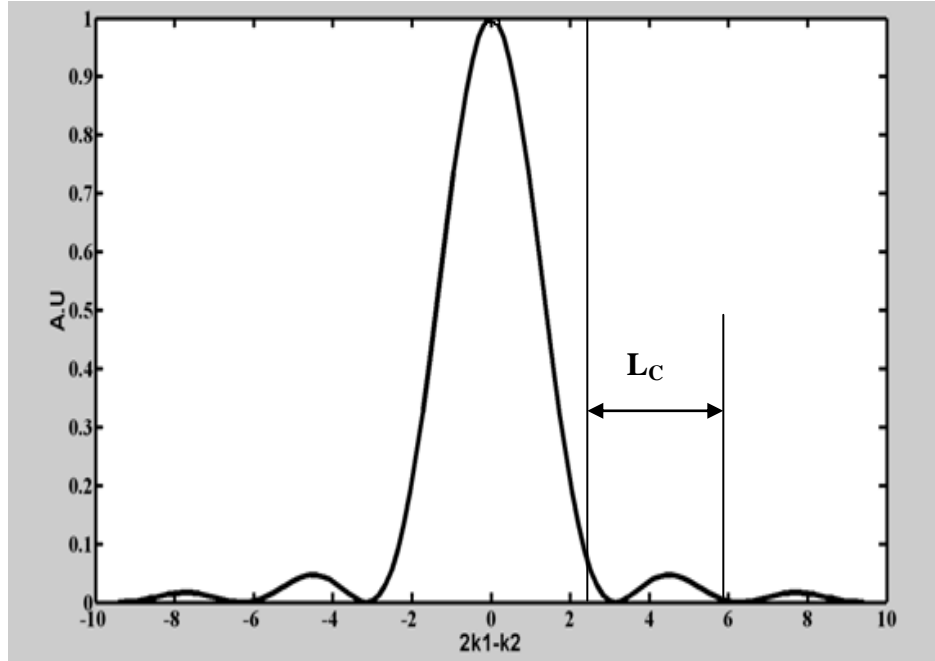
Figure 2.13 Variation of efficiency with $2k_{1-}\ k_2$

Clearly the efficiency is maximum when the interference term $\dfrac{\sin^2(\frac{2k_1-\ k_2\ )L}{2}}{(\frac{2k_1-\ k_2}{2})^2}$ is

maximum, i.e

$$\text{When} \quad \frac{(2k_1-k_2)}{2}L = 0 \qquad (2.43)$$

$$\text{i.e.} \quad 2k_1 = k_2 \qquad (2.44)$$

Thus for efficient frequency doubling this relation must be satisfied. This condition is called the phase matching criterion.

$$\text{Since } k_2 = 2\ \omega \frac{\eta_{2\omega}}{c} \text{ and } k_1 = \omega \frac{\eta_\omega}{c} \qquad (2.45)$$

Perfect phase matching is given by the equation 2.47

$$\eta_{2\omega} = \eta_\omega \qquad (2.46)$$

47

where $\eta_{2\omega}$ and η_ω are the refractive indices at ω and 2 ω respectively.

The coherence length, L_C, shown in figure 2.13 represents the maximum crystal length that is useful in generating second harmonic signal. Coherence length can be expressed as in equation 2.47 [1]

$$L_C = \frac{\pi}{2k_1 - k_2} = \frac{\lambda}{4\,(\eta_\omega - \eta_{2\omega})} \tag{2.47}$$

For phase matching the refractive index should be same at both wavelengths which is difficult to fulfill as most of the materials show some sort of dispersion in the refractive index. Birefringent materials can fulfill the condition of phase matching as they have different refractive indices for different polarization of light. A light wave entering inside the birefringent material is divided into two rays: ordinary ray (whose refractive index is independent of direction propagation) and extraordinary ray (whose refractive index depends on the direction of propagation). For the phase matching condition we need to choose a material in which the refractive index for the extraordinary ray at 2 ω is equal to that of the ordinary ray at ω or vice versa. Typically phase matching is attained either by angle tuning or temperature tuning the crystal. The method of angle tuning involves precise angular orientation of the crystal with respect to the propagation direction of the incident light. For the negative uniaxial crystal the refractive index for the ordinary ray is greater than the extraordinary ray and in this case the phase matching condition can be given as below [79]:

$$\sin^2 \theta = \frac{\frac{1}{n_0\,(\omega)^2} - \frac{1}{n_0\,(2\omega)^2}}{\frac{1}{n_e\,(2\omega)^2} - \frac{1}{n_0(2\omega)^2}} \qquad (2.48)$$

Where $n_0\,(\omega)$ and $n_0\,(2\omega)$ is the refractive index for ordinary ray at fundamental and second harmonic frequency respectively. The $n_e\,(2\omega)$ is the refractive index for extraordinary ray at second harmonic frequency and θ is the phase matching angle. For some crystals, notably lithium niobate, the amount of birefringence is strongly temperature-dependent [80]. As a result, it is possible to phase-match the mixing process by holding θ fixed at 90 degrees and varying the temperature of the crystal. The most commonly used crystals for frequency doubling are BBO (β-barium borate), KDP (potassium dihydrogen phosphate), KTP (potassium titanyl phosphate) and $LiNb_3O_4$ (lithium niobate). These crystals have the necessary properties of being strongly birefringent which is necessary to obtain phase matching. They also have specific crystal symmetry, transparent for both the impinging laser light and the frequency doubled wavelength, and have high damage thresholds which make them resistant against the high-intensity laser light.

2.4 Quasi-phase-matching

Quasi-phase-matching can be used when the normal phase matching technique cannot be implemented. Instead of a homogeneous nonlinear crystal material, a material with spatially modulated nonlinear properties is used. The idea is essentially to allow for a phase mismatch over some propagation distance, but to

reverse the phase of the nonlinear interaction at positions where the interaction would start to take place with the wrong phase and reverse the direction of conversion. The basic principle of quasi-phase matching is illustrated in Fig. 2.14, which shows both a single crystal of nonlinear optical material (part (a)) and a periodically poled material (part (b)).
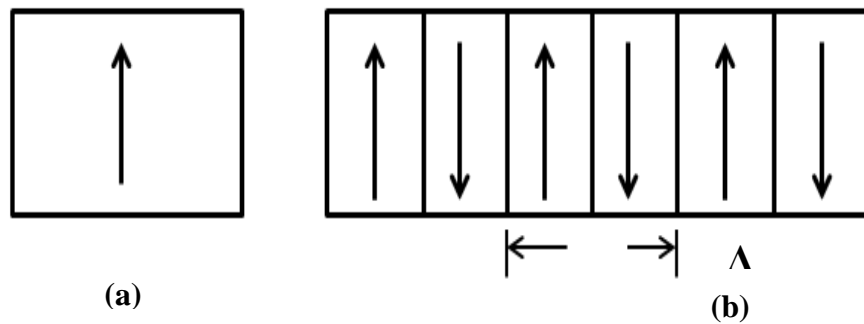
Figure 2.14 Schematic representations of a second order non linear optical material in the form of a (a) homogenous single crystal and (b) a periodically poled material in which the positive c axis is alternates in orientation with period Λ.

A periodically poled material is a structure that has been fabricated such that the orientation of one of the crystalline axes, often the c axis of a ferroelectric material, is inverted periodically as a function of position within the material. An inversion in the direction of the c axis has the consequence of inverting the sign of the nonlinear coupling coefficient $d$eff. This periodic alternation of the sign of d_{eff} can compensate for a nonzero wave vector mismatch Δk.

Periodically poled Lithium Niobate (PPLN) is the most commonly used crystal for the frequency doubling from the IR range to visible range due to its high optical nonlinearity and temperature phase matching. During the

manufacturing of PPLN the orientation of the c-axis of the Lithium Niobate crystal is periodically inverted which would generate the photons that are 180^0 out of phase with the generated photon that would have been created at that point in the crystal if it had not been inverted. By choosing the correct periodicity with which to flip the orientation of the crystal the newly generated photons will add constructively to the previously generated photons. As a result of this the number of photons generated will continue to grow over an interaction length of many times the original coherence length as the light propagates through the PPLN causing a higher conversion efficiency of input to generated photons. The period with which the crystal needs to be inverted is called poling period and it depends on the wavelength of the light (input and generated) and the temperature of the PPLN. The idea of quasi-phase-matching was first proposed by Armstrong et al [81], who suggested slicing a nonlinear optical medium into thin segments and rotating alternating segments by 180 degrees. The more recent techniques which have been developed involve the growth of crystals with a periodic alternation in the orientation of the crystalline c axis or allow the orientation of the c axis to be inverted locally in an existing crystal. Yamada et al. [82] demonstrated a very promising approach of use of a static electric field to invert the orientation of the ferroelectric domains in a thin sample of lithium niobate. In this technique, a metallic electrode pattern in the form of long stripes is deposited onto the top surface of a lithium niobate crystal, whereas the bottom surface is uniformly coated to act as a ground plane. A static electric field of the order of 21 KV⁄mm is then applied to the material, which leads to domain reversal only of the material

directly under the alternating top electrode stripes. Such crystals are now manufactured routinely and are readily available commercially.

2.5 Stimulated Brillouin Scattering (SBS)

Stimulated Brillouin Scattering (SBS) is a nonlinear process that can occur in single mode optical fibers where light is backscattered from a copropagating acoustic wave and the interference between the incident and backscattered wave leads to a growth in the acoustic wave amplitude. The SBS Stokes wave propagates only backwards in the case of fibers. Once the Brillouin threshold is reached significant backscatter of incident energy can occur. In a classical view, the process of SBS is a nonlinear interaction between the pump and the backscattered field, called the Stokes fields, through an acoustic wave. The interaction of the pump field and the Stokes field generates an acoustic wave through the process of electrostriction [79]. The acoustic wave in turn modulates the refractive index of the medium. This pump induced index grating scatters the pump light through Bragg diffraction and the scattered light is downshifted in frequency because of the Doppler shift associated with the grating moving at the acoustic velocity v_A. In a quantum mechanical view, the scattering process is an annihilation of a pump photon and creation of a Stokes photon and an acoustic phonon simultaneously. In the process, both the energy and the momentum should be conserved. The frequencies and the wave vectors of the three waves are related by

$$\Omega_B = \omega_P - \omega_S \qquad (2.49)$$

$$K_A = K_P - K_S \qquad (2.50)$$

Where ω_P, ω_S and Ω_B are the frequencies and K_P, K_S and K_A are the wave vectors of the pump, Stokes and Acoustic waves respectively. The Brillouin shift is given by

$$\Omega_B = v_A K_A \approx 2v_A K_P \sin(\theta/2) \qquad (2.51)$$

where is v_A is the speed of acoustic wave in fiber and θ is the angle between the pump and Stokes fields. In a single-mode optical fiber, SBS occurs only in the backward direction with the Brillouin frequency shift given by

$$\nu_B = \frac{\Omega_B}{2\pi} = \frac{2 n_P v_A}{\lambda_P} \qquad (2.52)$$

Where n_P is the effective mode index at the pump wavelength in vacuum λ_P. If we use $\nu_B = 5.96$ km/s and $n_P = 1.45$ for silica fibers, then we obtain $\nu_B = 11.1$ GHz at $\lambda_P = 1.55\mu m$.

When the acoustic waves decay in time as exp (- Γ_B t) with a damping constant of Γ_B, the Brillouin gain has a Lorentzian spectrum of the form [79]

$$g_B(\Omega) = g_P \frac{(\frac{\Gamma_B}{2})^2}{(\Omega - \Omega_B)^2 + (\frac{\Gamma_B}{2})^2} \qquad (2.53)$$

where the peak value of the Brillouin-gain coefficient occurring at $\Omega = \Omega_B$ is given by

$$g_P \equiv g_B(\Omega_B) = \frac{2\pi^2 n^7 p_{12}^2}{c \lambda_P^2 \rho_0 v_A \Gamma_B} \qquad (2.54)$$

and where P_{12} is the longitudinal elasto-optic coefficient and ρ_0 is the material density. The full width at half maximum (FWHM) of the gain spectrum is related to Γ_B as $\Delta\nu_B = \Gamma_B/2\pi$.

In the case of a pump laser with a Lorentzian spectral profile of width Δv_p , the gain spectrum is still given by equation 2.53 but the peak value of Brillouin gain is reduced by a factor $1 + \frac{\Delta v_p}{\Delta v_B}$ [83]. The Brillouin-gain spectrum for silica fibers can differ significantly from that observed in bulk silica because of the guided nature of the optical modes [84]. The Brillouin gain spectrum of a fiber also depends considerably on details of the fiber design and the presence of dopants in the fiber core. Under CW or quasi-CW pump conditions, for the purpose of estimating the Brillouin threshold the pump depletion can be neglected and the Brillouin threshold, where a significant fraction of the input radiation is backscattered, is found to occur at a critical pump power P_{cr} given approximately by [85]

$$P_{cr} = \frac{21 A_{eff}}{g_B (\Omega_B) L_{eff}}$$ (2.55)

where the peak value of the Brillouin gain given by Equation 2.54 and A_{eff} is the effective core area and L_{eff} is the effective fiber length defined as follows

$$L_{eff} = [\, 1 - \exp(\alpha L)]/\alpha$$ (2.56)

Where L is the length of the fiber and α is the fiber loss.

The effective Brillouin gain can be reduced by many factors in practice e.g the SBS gain decreases by a factor of two times and threshold increases by two times when the state of polarization of the pump field becomes completely scrambled because of birefringent fluctuations [86]. The medium response in the SBS case is governed by the phonon lifetime T_B with a typical value of <10 ns in silica fibers. The quasi-CW regime is valid only for pump pulses of widths 100 ns or more.

When the pulse width is of the order of 10 ns, it is necessary to consider the dynamics of the acoustic mode participating in the SBS process which can lead to transient spikes and dips in the backscattered stokes radiation.

2.6 Optical Low Coherence Reflectometry (OLCR)

Low coherence interferometry (LCI) is a type of interferometry technique based on low-coherent light sources [87]. Partially coherent light is defined as light with a short coherence length, but having high spatial coherence. A low-coherence light source can be composed of superposition of different wavelengths rather than a single wavelength. The coherence length is a measure of the light beam's temporal coherence and is inversely proportional to its frequency content or bandwidth. LCI allows the precise measurement of the amplitude and the relative phase of reflected or backscattered light. A Michelson optical interferometer consists of a light source, a beam splitter which splits the light into a reference arm and a measurement arm and a light detector. The measurement beam is reflected from the specimen with different delay times. The reflected beam depends on the various refractive indexes in the different layers of the specimen. The reference mirror is positioned on a movable delay line and the light reflected from this mirror will produce a variable time delay reference pulse. The light from the reference mirror and the light from the specimen which consists of multiple partial reflections at multiple delay times are then correlated and detected. After signal processing the optical distance of the reflecting regions in the specimen are determined. The technology has developed with several different nomenclatures.

OTDR is the optical time domain reflectometry and this involves optical ranging with femtosecond laser pulses and nonlinear cross correlation techniques. OCT is optical coherence tomography and this technique is used to construct a two dimensional, transverse image of the sample from a series of one dimensional scans. OCDR is optical coherence domain reflectometry or Optical low-coherence reflectometry (OLCR). It is a one dimensional optical ranging technique where the amplitude and longitudinal delay of backscattering from a sample is resolved using low-coherence Michelson interferometer. Optical low-coherence reflectometry (OLCR) was developed about 15 years ago [88], and has since become a widely-used tool for measuring optical reflectivity as a function of distance. The OLCR technique has gained popularity since its invention and has applications in various fields. The OLCR technique was initially used for the reflection measurements in telecommunications devices with micron resolution [89, 90, 91]. Danielson and Whittenberg [97] developed a new type of all fiber reflectometer with micrometer resolution. Their technique used a scanning Michelson interferometer with a broadband light source and cross-correlation detection. Youngquist et al [92] developed optical coherence reflectometry as a new optical evaluation technique to determine the positions and magnitudes of reflection sites with miniature optical assemblies. Their instrument consisted of a Michelson interferometer with a short coherence length laser diode operating at 830 nm. The all fiber implementation of OLCR Michelson interferometer has been described in detail by Novak et al [93]. OLCR is now a well-established tool for detecting, localizing, and quantifying reflecting discontinuities and

irregularities in optical waveguides and circuits. Among the various high-resolution coherent techniques, such as those based on optical frequency scanning, OLCR offers advantages in both theoretical performance and practical implementation [94]. This technique can resolve surfaces spaced by less than 10µm [95] and can detect optical power reflectivities as low as -136 dB [96].

The present work based on the simultaneous measurement of both the physical thickness and group index of reasonably transparent objects. OLCR can provide the thickness measurements with accuracies of less than 0.1 µm [97] and group index measurements with accuracies on the order of 10^{-5} to 10^{-7} [98] depending on the sample size. In the recent years it has been possible to build low-coherence interferometers based on optical fibers, optical fiber couplers and the super luminescent diode light sources. The development and availability of super luminescent light emitting diode (SLD) made the low-coherence reflectometry practical in a fiber-optic systems [99,100]. Also the development of fiber optic devices such as couplers played an important role in the development of fiber optic based devices.

2.6.1 Basic Set Up of OLCR

The basic setup of OLCR is shown in figure 2.15 with the device under test (DUT) placed in one of its arms.
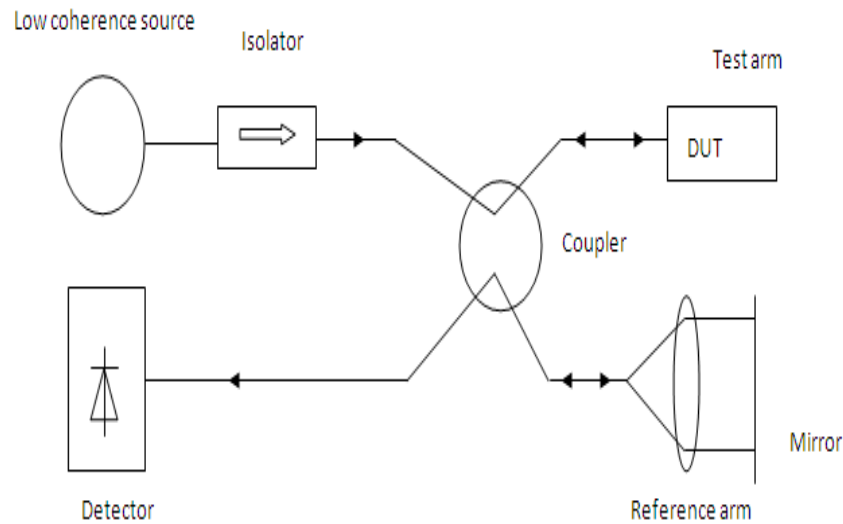
Figure 2.15 Simplified OLCR arrangement

The low coherence source is coupled into a fiber and divided into two parts in a 3-dB coupler as shown in the figure 2.15. Half of the signal goes into device under test (DUT) arm, while the other half is launched into free space towards a mirror on the scanning translation stage called reference arm. When the optical path lengths to the mirror equals the optical path length to a reflection in the DUT, the signals from the two arms add coherently to produce coherence fringes called a coherence spike at the detector located on the fourth arm of the coupler. When the optical path length difference becomes larger than the coherence length of the source, the interference signal no longer exists. The amplitude of the coherence signal is proportional to the reflection coefficient of the feature in the DUT. Translating the mirror allows the reflectivity profile of the DUT to be mapped. The optical delay (light propagation time) in the reference arm can be varied by

58

movement of the reference mirror. The reflected signals from each arm travel back through the coupler, where they are recombined and received at the photodiode. By the nature of the coupler, half of the reflected power will be directed back to the source where it is attenuated by the isolator. From the arrangement shown above, an interference signal will appear at the photodiode if the difference in optical length between the reference and test arms is less than a coherence length. The coherence length of the system is determined by the spectral width of the source according to the equation 2.58.

$$L_c = \frac{\lambda^2}{n\,\Delta\lambda} \qquad (2.57)$$

where n is the refractive index of the test material, λ is the average source wavelength, and $\Delta\lambda$ is the source spectral width. The incident power on the detector leads to a photocurrent which is described by the following:

$$I = R\left[P_{REF} + P_{DUT} + 2\sqrt{P_{REF}\,P_{DUT}}\quad \cos(\phi_{REF}(t) - \phi_{DUT}(t))\right] \qquad (2.58)$$

where R is the responsivity of the photodiode, P_{REF} is the reflected reference signal with optical phase of $\phi_{REF}(t)$, and P_{DUT} is the reflected test signal with phase $\phi_{DUT}(t)$.

One assumption made for deriving the photocurrent expression is that the polarization states of the reference and test reflected signals incident upon the photodetector are parallel to each other. This matched state maximizes the interference signal created from the combined reflected power. Conversely, signals received at the photodiode having orthogonal states of polarization will

create no interference signal even when the optical length of the two arms is within the coherence length, L_C, of the source. According to the photocurrent equation, when the optical length difference of the two arms is greater than a coherence length, the phases of each path are uncorrelated, varying randomly with respect to one another.

2.6.2 Low-Coherence Source

The Michelson interferometer arrangement can be operated using virtually any type of optical source. However, for OLCR the use of a source possessing wide spectral width properties, and thus a short coherence length is required. An additional consideration when selecting a low coherence source is that of optical power. To help resolve weakly reflecting surfaces in the test arm, higher incident power typically results in a stronger interference signal. Therefore, an increase in overall sensitivity of the OLCR system is observed. OLCR sources must also have very low internal reflections. Most commonly used are the semiconductor edge-emitting light emitting diode (EELED), with an output of approximately 100 μW of power with a spectral width of 50 nm. EELEDs are capable of coupling more low-coherence power into a single mode fiber at 1.3μm and 1.55 μm than surface-emitting LEDs (97). This combination provides an approximate 16 μm resolution in a fiber at 1550 nm and relatively good measurement sensitivity with respect to the low-cost nature of EELEDs. One possible problem with the use of a standard EELED is the introduction of sidelobes to the OLCR measurement trace. These

sidelobes are introduced due to the strong internal reflections from the end facets of the diode and range from -30 to -55 dB.

Another commonly used source in OLCR is the erbium-doped fiber amplifier (EDFA). The amplified spontaneous emission (ASE) output of the EDFA can provide in excess of 10 mW optical power with a spectral width of approximately 20 nm. This high output power makes the EDFA a better choice over the EELED when greater reflection sensitivity is desired. In addition, the operation of the EDFA leads to better suppression of measurement sidelobes. The few disadvantages in using an EDFA are the decrease in resolution, due to a more narrow spectral width, and the significantly higher cost when compared to the EELED. These considerations, along with the desired measurement sensitivity, are usually the basis for the final decision of which low-coherence source one chooses.

CHAPTER 3

EXPERIMENTAL METHODOLOGIES FOR DUAL PULSE LIBS

This chapter describes the equipment and experimental techniques used to develop a fiber laser system for dual pulse LIBS applications with a tunable narrow linewidth pulse. Details of laser diodes, fibers, and other components used for functioning of erbium doped fiber amplifier are described. Signal amplification using the large mode area fiber and the frequency doubling and quadrupling techniques are also explained. The methods used for signal analysis of the data will be outlined.

3.1 Experimental Set up of the Fiber Laser System

The layout of the fiber laser system developed for this project is shown in figure 3.1. The system consisted of a seed laser source followed by a double pass amplifier and then a single pass large mode area fiber laser. A directly modulated 1545 nm distributed feedback laser (DFB) diode with an output of 20 mW was used as a seed laser source. A 1480 nm laser diode was used as a pump for the double pass amplifier and combined with the seed laser pulse through a wavelength division multiplexing (WDM) coupler. The output of the WDM was spliced to a single mode Er fiber through a 3 port circulator. The far end of the fiber was spliced to a 1544 nm fiber Bragg grating. The other port of the circulator was spliced to an ASE Band pass filter. A polarization controller was spliced to the ASE filter to control the polarization state of the output radiation.

The output from the first stage amplifier was then passed through the large mode area (LMA) PM Er/Yb doped fiber for further amplification. The other end of the LMA Er/Yb fiber was angle cleaved to reduce the feedback. We found that without angle cleaving the fiber end was damaged after some time. The amplified output was frequency doubled using a PPLN crystal and then quadrupled with a BBO crystal. Then the fundamental and quadrupled pulses were focused onto the target material for the demonstration of dual pulse LIBS.
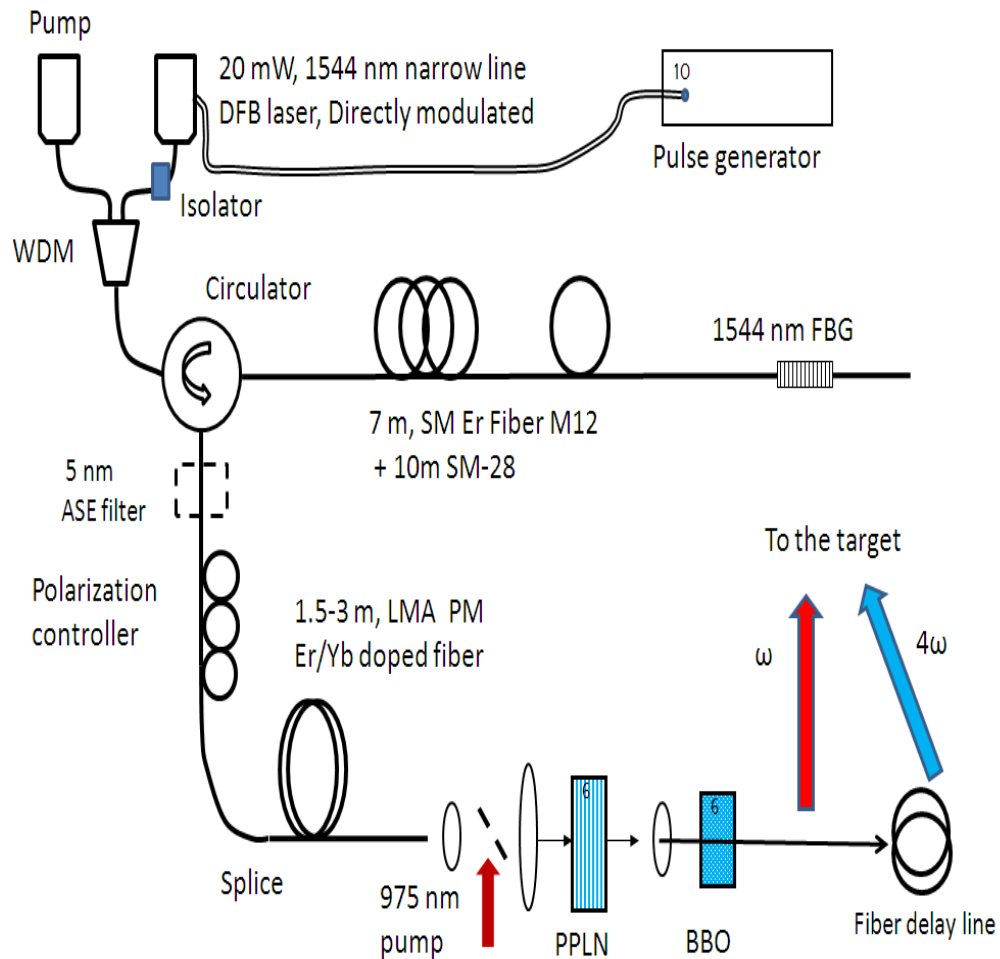
Figure 3.1 Experimental Setup

3.1.1 Seed Laser Diode

A 1550 nm GaInAsP DFB laser diode (Model # CQF935/708) [101] was used as the seed laser source. The laser diode has a polarization maintaining (PM) fiber pigtail which makes coupling seed signal into the fiber more efficient. It also has a built-in optical isolator and thermoelectric cooler and a spectral linewidth of 1MHz. Specifications for the laser diode are given in Table 3.1.

Temperature (C)	-5	25	70
Threshold Current I_{th} (mA)	19.4	19.3	19.4
Slope efficiency E_C (mW/A)	234.1	246.1	252.5
Series Resistance (Ohm)	4.3	4.4	4.5
Operating current I_{OP} (mA)	104.3	100.4	98.4
Peltier Current I_{pelt} (mA)	400	46	-536
Monitoring current I_{mon} (μA)	543	520	509
Operating Voltage V_{OP} (V)	1.30	1.29	1.29
Peltier Viltage V_{pelt}(V)	-0.86	-0.13	1.23
Wavelength temperature tunability (nm/C)	0.07	0.07	0.07

Table 3.1 Operating specifications for DFB laser diode from OEQuest for three different temperatures.

The central wavelength is 1545.34 nm with the maximum output power of 20 mW.
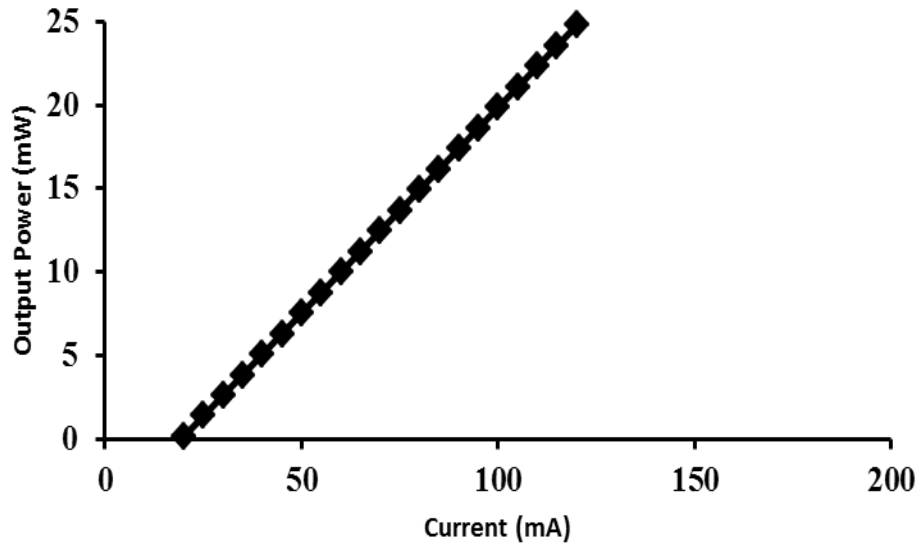
Figure 3.2 Measured output power vs current for the DFB laser diode (at a temperature of 25 C).

Figure 3.2 shows the measured variation of output power vs current for the DFB laser diode. The maximum usable output power is about 20 mW as we can operate up to a current of about 100 mA according to the operating specifications. The power versus current plot was in good agreement with the specification sheet of laser diode provided by the manufacturer. An HTC-1500 [102] temperature controller was used for controlling the temperature of the seed laser diode. Features such as adjustable thermistor current, buffered thermistor resistance measuring, variable current limiting and an indicator system to indicate acceptable operating thermistor resistance were present. The temperature and resistance curve was plotted (figure 3.3) using the standard formula for NTC thermistor given as below

$$R = R_0 \exp[\beta(\tfrac{1}{T} - \tfrac{1}{T_o})] \qquad\qquad (3.1)$$

Where R_0 is the thermistor's nominal resistance at room temperature, T_0, β is the thermistor's material constant in K and T is the thermistor's actual temperature in Celsius. Using R_0 =10kOhm, T_0 = 25C and β = 3960K, provided by the manufacturer specification, the temperature vs resistivity curve is given as in figure 3.3.
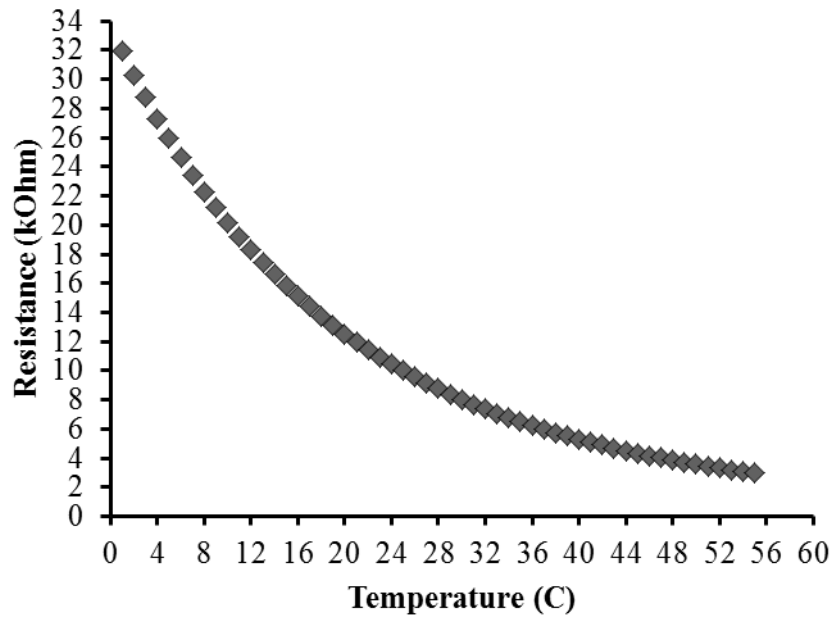
Figure 3.3 Temperature curve for the laser diode

The DFB laser diode was modulated using a Trapezoid function generator using the schematic as shown in figure 3.4. This function generator can provide the change in pulse width and also change of pulse rise time. A Schottky diode was connected in reverse bias to avoid any damage to the seed laser diode in case of

voltage reversals. With the help of function generator we could set the pulse width

ranging from 20 ns to 2 μs at different repetition rates as shown in figure 3.5.
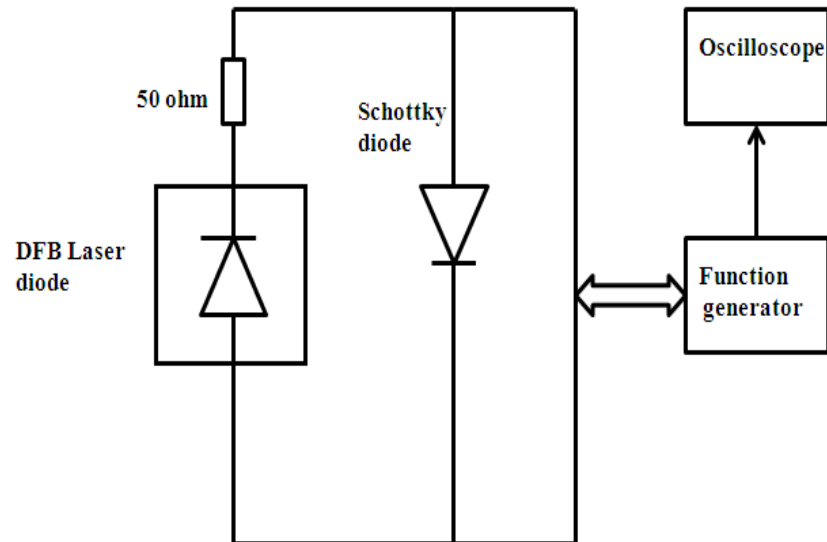
Figure 3.4 Modulation of DFB laser diode
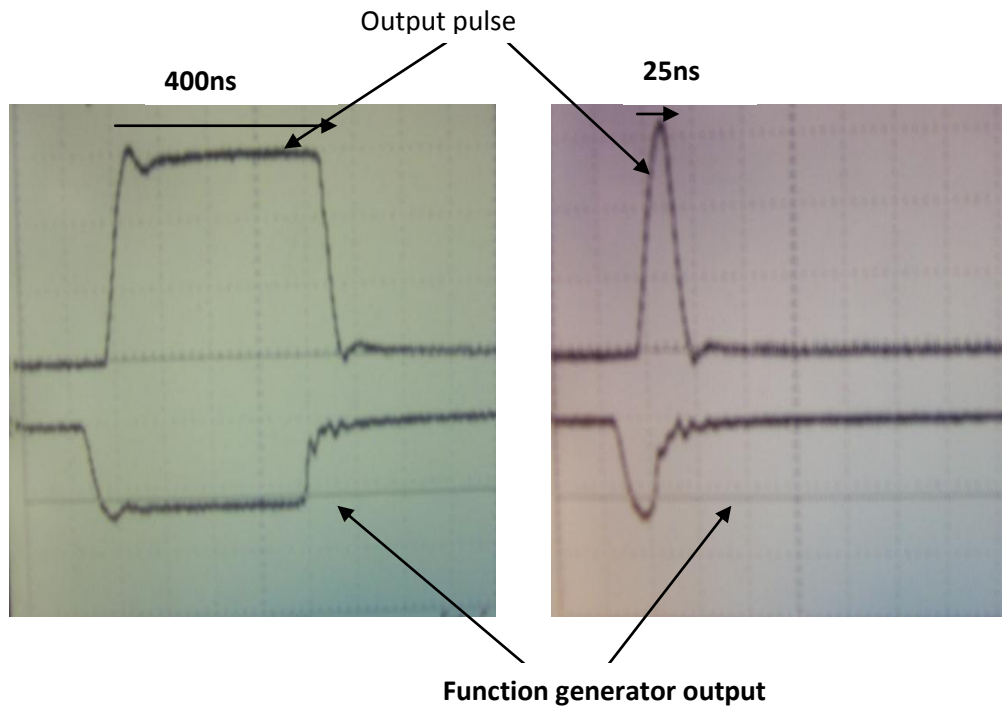
Figure 3.5 DFB laser diode output measured by an optical photodiode compared to the function generator pulse used (The function generator pulse has been inverted in the oscilloscope).

3.1.2 Pump Diode

Initially a 980 nm laser diode (with maximum output power = 115 mW) was chosen as a pump for the first fiber amplifier but later it was replaced with the 1480 nm laser diode. Advantages of the 1480 nm laser included the higher output power of 250 mW as opposed to 115 mW. In addition, the 1480 nm wavelength has higher optical conversion efficiency than 980 nm, since the 980 nm must excite the erbium ions to a higher energy level than the 1480 nm. This energy difference is dissipated and does not contribute to stimulated emission. Therefore,

it is expected that more output energy can be obtained using the 1480 nm pump. The pump laser diode specifications are given in the Table 3.2 [103].

Part Number	FOL1404QQO
Operating Power (typical)	250 mW
Maximum Operating Current	1300 mA
Maximum TEC Current	3.4 A
Thermistor Resistance at 25^0C	10 KOhm
Thermistor B coefficient	3900 K
Peak Optical Output (Specific)	1460-1480 nm

Table 3.2 Specifications of the 1480 nm diode pump employed

A separate current driver and temperature controller were used for powering of this laser diode. The output power was measured versus drive current and plotted for the pump diode as shown in figure 3.6. The resulting curve corresponds closely to the specifications provided by the manufacturer.

3.1.3 Erbium doped Fiber

Metrogain^{TM} 12 [104] fiber was used as the first stage gain medium for the laser system. This fiber provides high output efficiency. The absorption and gain curves versus wavelength for the M-12 fiber are shown in figure 3.7.
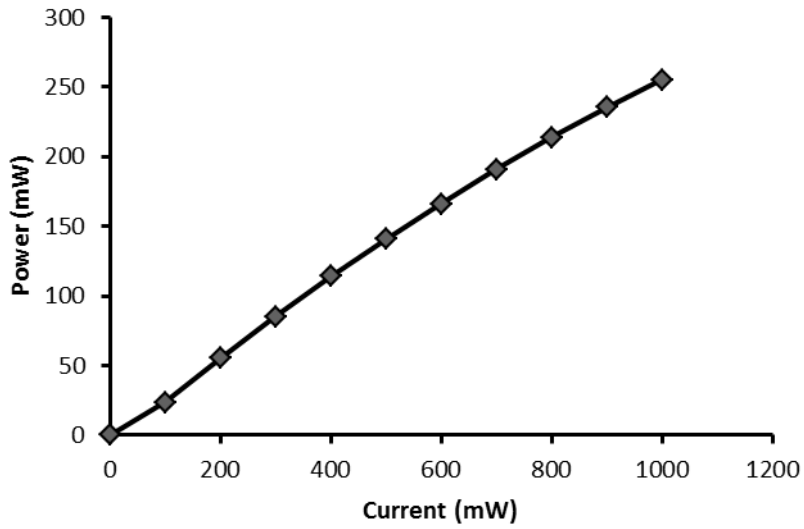
Figure 3.6 Measured output power as a function of current for the 1480nm pump laser diode.
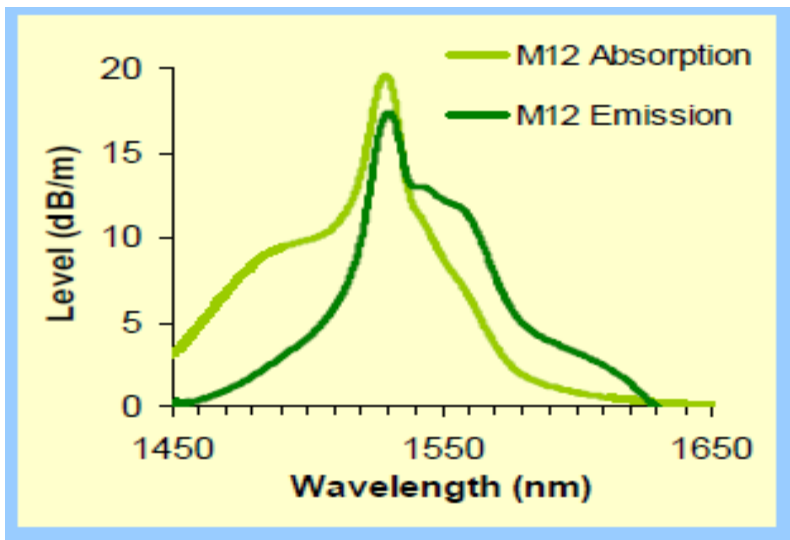
Figure 3.7 Manufacturer specifications of absorption and emission curves for the Metrogain M-12 fiber [104].

The Specifications for the M-12 fiber are given in Table 3.3.

Numerical Aperture	0.21-0.23
Absorption at pump wavelength of 980 nm	11-13 dB/m
Fiber diameter	125±1 μm
Coating diameter	245 μm (nominal)
Mode Field Diameter at 1550 nm	6.2 μm

Table 3.3 Manufacturer specifications for the Metrogain M-12 fiber

M-12 offers more than twice the levels of pump absorption in comparison with the commonly used M-5 fiber which has an absorption of 5 dB/m at 980 nm pump. This reduces the gain-length and material cost required. In fact, highly effective EDFAs have been manufactured with as little as 3 meters of M-12. The M-12 with short gain-length can be combined with an optional reduced diameter, 80 μm fiber. This reduction in fiber diameter causes a proportional reduction in bend-induced stress, enabling the form-factor of the EDFA to be reduced without compromising the reliability or lifetime of the device. For the current laser system first we tried the 3 m length of the M-12 fiber but couldn't get enough gain so later the fiber length was increased to 7 m.

3.2 First Stage Amplifier

The first stage amplification is carried out in a double pass Erbium doped fiber amplifer (EDFA). The pump laser diode and seed laser diode were combined with the help of a WDM combiner. Two isolators were introduced into the circuit one after the seed laser diode and the other after the Er doped fiber. Isolators were used to remove any feedback or back reflection. A 1550 nm 3-port circulator (Model # 6015-3) [105] was used. The output of WDM was spliced to the one port of circulator and the other port of the circulator was spliced with the 7 m of single mode M-12 Erbium doped fiber. The 3-Port PM Circulator is a polarization-maintaining fiberoptic circulator. It is a compact, high-performance lightwave component that routes incoming signals from port 1 to port 2, and incoming port 2 signals to port 3. Light entering port 2 experiences a large amount of loss at port 1 and light entering port 3 experiences a large amount of loss at ports 1 and 2. This device provides high polarization extinction ratio (PER), optical isolation, low insertion loss, and excellent environmental stability. The far end of the M-12 fiber was spliced with the 1544 nm fiber Bragg grating (FBG) (Model # OEFBG-100) [106]. This FBG has a bandwidth of about 2 nm and gives a reflectivity greater than 90%. The transmission curve provided by the manufacturer is shown in figure 3.8.
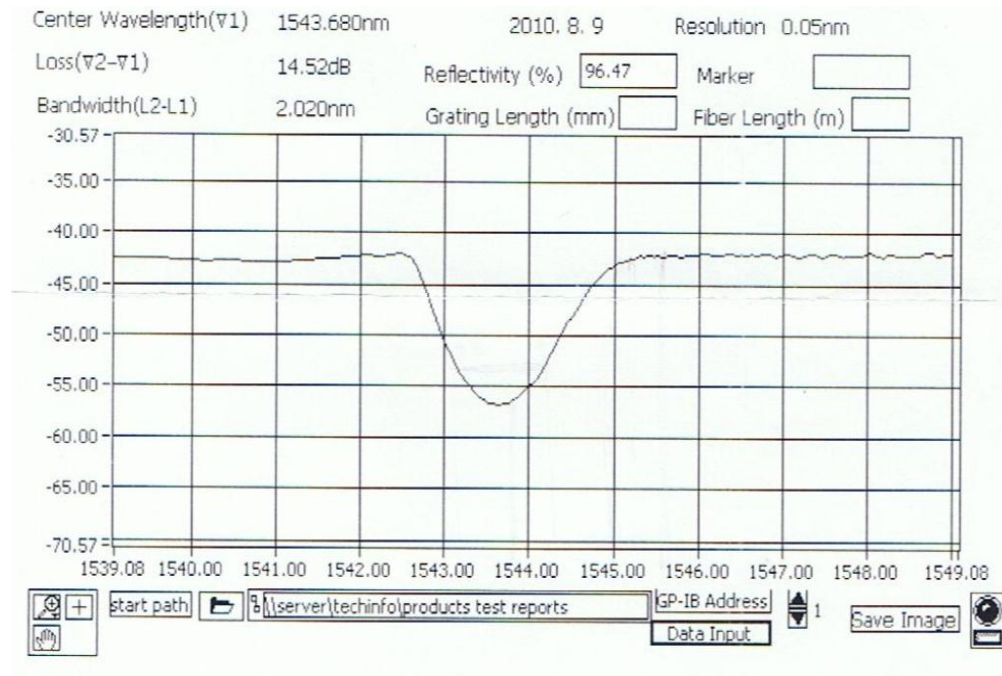
Figure 3.8 Transmission curve for 1544 nm fiber Bragg grating (FBG) [106].

The FBG reflects the signal back into the erbium fiber and so the signal passes through the erbium fiber twice and efficient amplification is achieved. The third port of the circulator is monitored for the amplified output.

In case of fiber gain length of 7 m an output of about 4 μJ was obtained after the double pass through the erbium doped fiber for an injected pulse length of 25 ns and pulse energy of 0.40 nJ. This is not sufficient energy for the frequency doubling stages so an additional amplifier stage is required. For the second stage amplification large mode area, polarization maintaining Er/Yb doped fiber was used. But before feeding the output of first stage amplifier into the second stage the ASE needed to be minimized. With the help of FBG reflector in the first amplifier stage, the ASE already was reduced to a large extent but for further reduction by a 5 nm band pass filter (Part # BPF-1545-B-1-0-5-13.5) [107]

73

with the center wavelength at 1545 nm was used between the first and second amplifier stages. To maintain the polarization between both amplifier stages a fiber polarization controller (FPC560) [105] was spliced onto the output end of the band pass filter. This polarization controller utilizes stress induced birefringence to create three independent fractional wave plates to alter polarization in the single mode fiber. Single mode fiber is looped into three independent spools creating three independent fractional wave plates. The amount of birefringence induced in the fiber is a function of the fiber cladding diameter, the spool diameter, the number of fiber loops per spool, and the wavelength of the light. The fast axis of the fiber, which is with the electric field vector in the plane of the spool, is adjusted with respect to the transmitted polarization vector by manually rotating the paddles. The first paddle acts like a quarter wave plate which can transform the input polarization state into a linear polarization state, the second paddle is a half wave plate and it would rotate the linear polarization state. The third paddle behaves like quarter wave plate which would transform the linear state into an arbitrary polarization state. Therefore by adjusting each of the three paddles complete control of output polarization state over a broad range of wavelength is achieved. All the fiber splicing has been performed with the help of fusion splicer (Fiberlign QFS-1001) [108]. For protecting the splices the heat shrinking protection sleeves were used around each spliced joint.

3.3 Second Stage Amplifier

For second stage amplification, double clad large mode area polarization maintaining (LMA-PM) Er/Yb codoped fiber with a length of about 3m was used as the gain medium. The fiber core/cladding diameters (numerical apertures NA) are 25/300 μm (0.10/0.46) with a nominal absorption of 25 dB/m at 1550 nm. The pump laser was a fiber coupled diode laser (part # LIMO25-F200-DL) [109] with CW output at 976 nm. The pump diode has a fiber output with the core diameter of 200 μm and numerical aperture of 0.22. The high power laser diode driver LDD100-3 [109] was used to drive the pump laser diode. Besides controlling the current of the laser diodes, the LDD100-3 also features a built-in controller for thermoelectric coolers (Peltier elements). Laser diode current as well as current limit and temperature of the heat sink can be set on the front panel. The power-current characteristics for this pump diode were measured and are shown in figure 3.9.
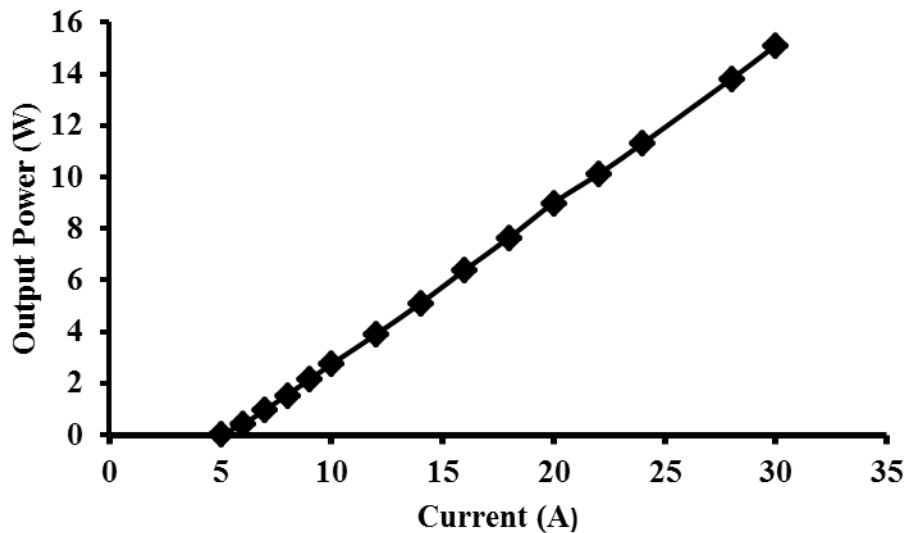
Figure 3.9 Output power versus Current for the LIMO pump laser diode

The pump radiation was coupled into the active fiber by a collimating lens and through a dichroic mirror (DM) 45^0 as shown in the figure 3.10. The outer end of the fiber was angle cleaved at an angle of 10^0 to avoid unnecessary reflection and facet damage.
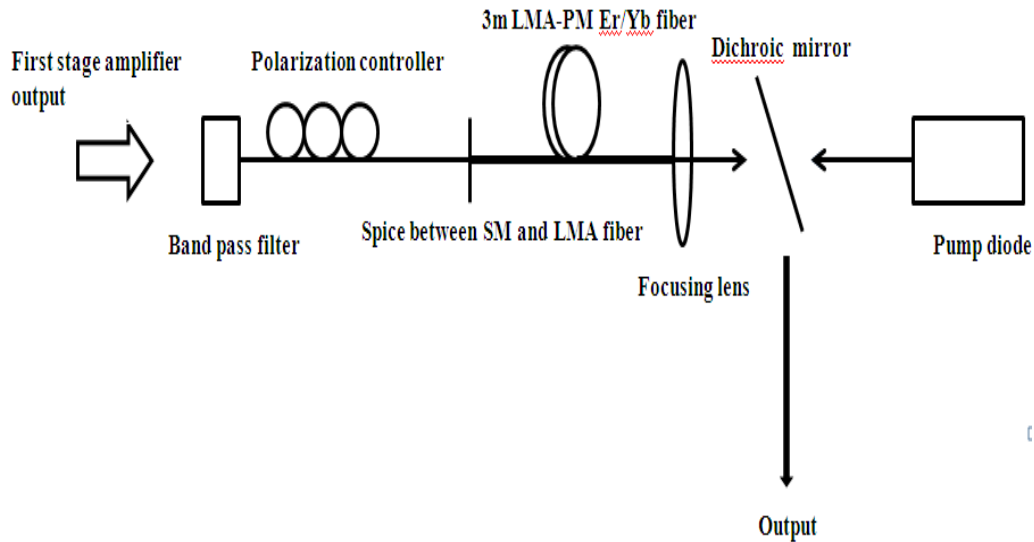
Figure 3.10 Schematic layout of the second Stage Amplifier

The coupling between single mode fiber and the large mode area fiber proved to be difficult. First we tried to butt couple both fibers, but the transmission was very small and not stable. Then to reduce the buildup of extra ASE from the input facet of the LMA fiber, it was first spliced with the single mode fiber. To do this the large mode area fiber was tapered to the diameter of the single mode fiber and then cleaved as shown in figure 3.11. The tapering of the LMA fiber was done with the help of fiber splicer with an arc current of 22 mA for 2.5 s. After tapering the LMA fiber was cleaved at the point where the diameter of the LMA fiber was

same as that of SM fiber. After cleaving the both fibers were fusion spliced with the help of splicer.
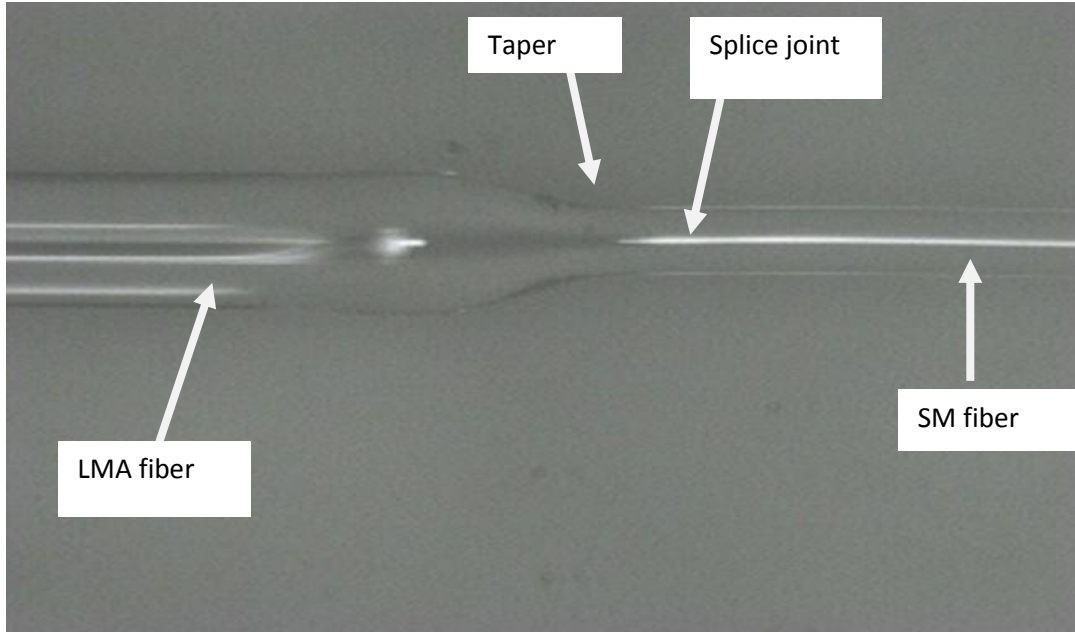
Figure 3.11 Splice between large mode area fiber and single mode fiber.

3.4 Frequency Upconversion

The amplified signal was frequency doubled by focusing onto a PPLN crystal with the help of a 5 cm lens. The PPLN crystal that was used for the second harmonic generation was purchased from the Thorlabs and had five regions each with different poling periodicity (PP). Thus the crystal can be used to frequency double a range of wavelengths by varying the PP region and the temperature used. The PPLN crystal has length of 10 mm and an operating temperature of   160-200°C. The technical specifications for the PPLN crystal used are given in table 3.4.

Thickness	0.5 mm±0.05 mm
Width	10 mm±0.5 mm
Length	10 mm±0.2 mm
Periods	18.20, 18.40, 18.60, 18.80, 19.00 μm
Periodically poled gratings	5; each grating is 0.5mm wide with individual periods as listed above. Each poled grating is separated by 0.2mm wide regions of unpoled material
Reflectivity	AR coated to less than 1% reflectivity at 1540-1660nm/770-830nm on both factets.
Maximum operating Temperature	220 ^{0}C
Maximum Ramp Rate	10 ^{0}C/min

Table 3.4 Specifications of PPLN Crystal

The detailed layout of the PPLN is shown in the figure 3.12.
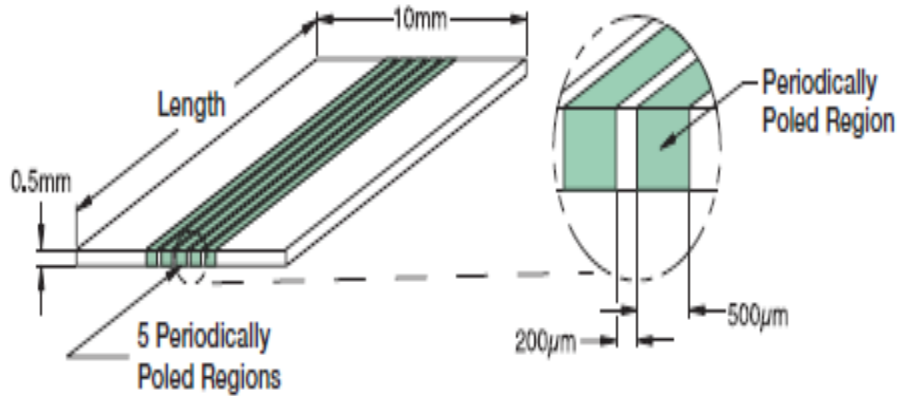
Figure 3.12 Details of the PPLN crystal used for frequency doubling

The PPLN crystal was mounted on a lab made crystal holder. The crystal holder also had a heater made in lab which was used to heat the crystal to the desired temperature. The details of the crystal holder and heater are given in next chapter. For monitoring the temperature a thin film platinum thermistor was glued to the corner of the crystal holder. The temperature-resistance curve for the thermistor is shown in figure 3.13. The temperature of the crystal was recorded by measuring the resistivity of the thermistor using a digital multimeter.
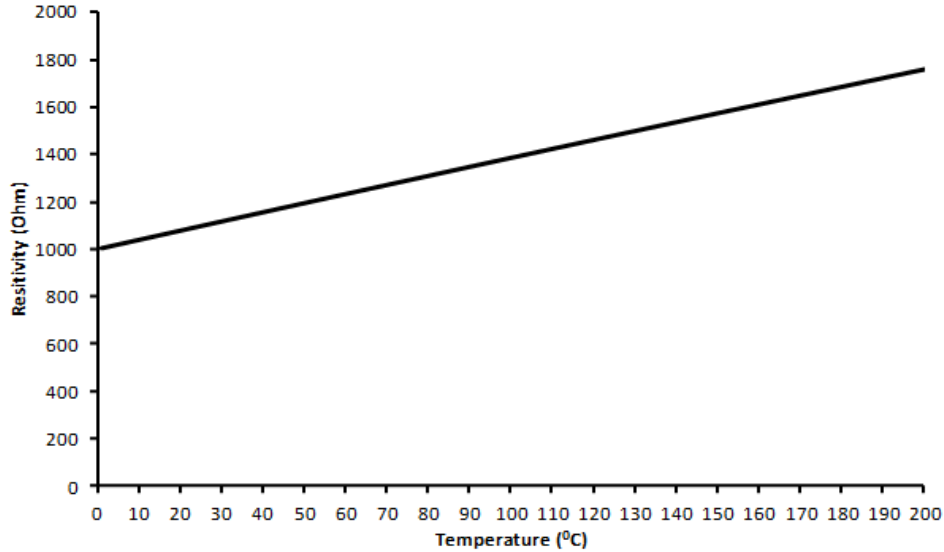
Figure 3.13 Temperature-Resistance curve for thin film Pt Thermistor

The frequency doubled output was further focused onto a BBO crystal for frequency quadrupling. The BBO crystal has a size of 8x8x1.5 mm and it was cut for type 1 second harmonic generation of 800 nm at theta of 29.2 degrees. It had AR coating at 808 nm and 400 nm on both sides. It was mounted in a one inch anodized Al holder with manual adjustment of the phase matching angle.

3.5 LIBS Setup

The experimental set up used for performing the LA-LIF experiments is shown in figure 3.14. The fundamental pulse (1545 nm) was used for the ablation and plasma formation. Then the resonant pulse (fourth harmonic pulse) with energy of about 1 μJ was focused onto the target material. The emitted signal was imaged onto the entrance slit of a 1/4 m, f/3.9 imaging spectrometer (Oriel MS260i) [110]

equipped with an intensified charge coupled device (ICCD) camera (Andor iStar DH720) [111]. A grating with 2400 lines mm^{-1} was employed for spectral dispersion in the spectrometer giving an instrument resolution of 0.45 nm for a slit width of 300 μm which was typically used. A pair of off axis parabolic mirrors was sued for the focusing the emitted signal into the spectrometer. The target chosen for ablation is a thin substrate mounted on a rapidly rotating computer hard drive which was continuously rotating at 5400 rpm.
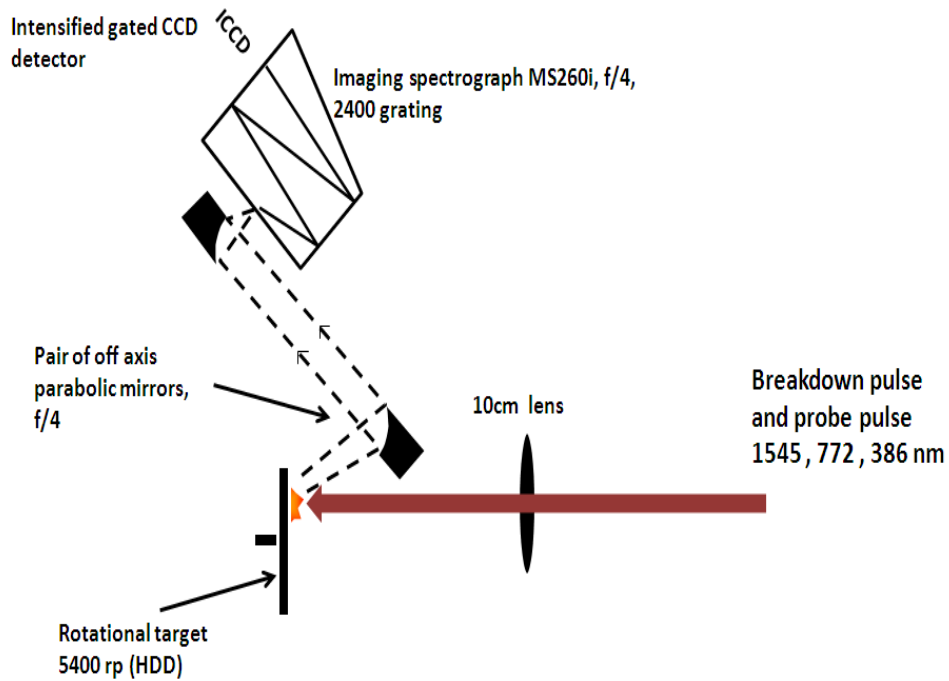
Figure 3.14 LA-LIF Setup

CHAPTER 4

RESULTS AND DISCUSSION FOR DUAL PULSE LIBS

The main objective of this work was to develop the required fiber laser system for smart, portable and rugged LIBS fiber optic sensors. The reported laser system is made up of all standard telecom components which make the system robust and inexpensive. The laser system is based on multistage amplification of a narrow spectral line seed pulse from a fiber coupled DFB diode laser. After the first stage amplifier a 20 ns laser pulse with energy of about 4 µJ was obtained which was further amplified up to 50 µJ in a second stage amplifier. The description of the laser system along with experimental setup has been discussed in detail in chapter 3. The input and output characteristics of first stage and second stage amplifiers will be discussed in detail in this chapter. This chapter also includes a detailed discussion of frequency doubling and quadrupling and their use in LA-LIF.

4.1 First Stage Amplifier

The experimental schematic for the first stage amplifier is shown in figure 3.1. The first step was to characterize the seed laser diode. The amplified output power was studied with respect to input seed laser diode power at different pump power levels. Amplified spontaneous emission (ASE) was also estimated. The narrow line width 1545 nm (line width 1 MHz) fiber pigtailed DFB laser diode was used as the seed source. The seed laser diode was directly modulated with the help of a function generator as described in the section 3.1.1. Laser pulses with widths from 20 ns to 2 µs could be obtained at different pulse repetition rates. The DFB laser

diode provided a pulse energy of 0.40 nJ for a pulse width of 20 ns at a repetition rate of 20 KHz. The seed laser diode was later combined with a 1480 nm pump laser diode through a 1480-1550 WDM coupler for injection into the first amplifier stage. The other end of the WDM coupler was fusion spliced with the 7 m of single mode Erbium doped fiber (M-12). An isolator was also spliced between seed laser diode and the WDM coupler to avoid any parasitic feedback. 10 m length of single mode fiber was also spliced onto the far end of the Er doped fiber to increase the fiber length and enhance the SBS effect. It was observed that there was a large amount of ASE present in the output power. Thus there was need to filter the ASE before coupling the output of the first stage amplifier to the second stage amplifier.

4.1.1 First stage Single pass amplifier

Before splicing the DFB seed laser diode with an isolator its output power at different function generator voltage was recorded with the help of power meter. The pulse energy was estimated from the measured output power and the repetition rate and is shown in figure 4.1.
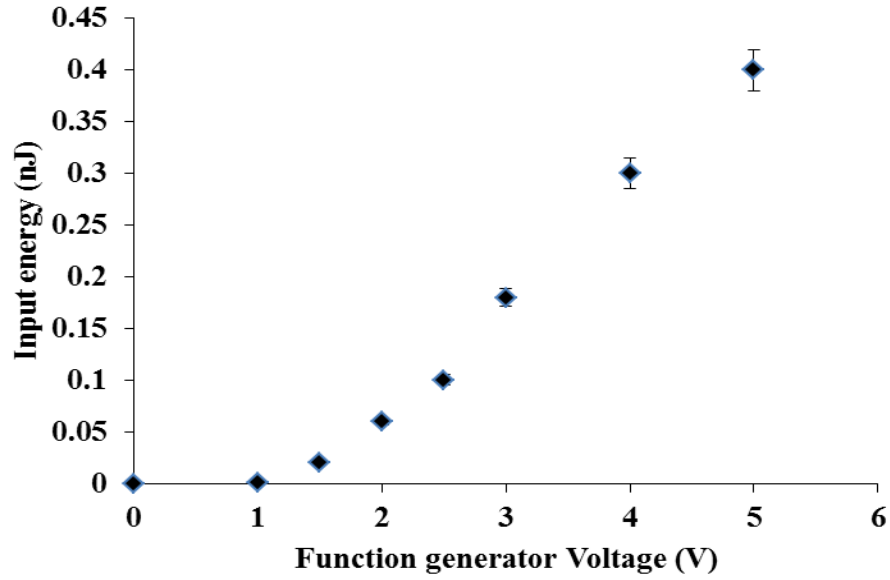
Figure 4.1 Variation of pulse energy with different function generator voltages into the single pass first stage amplifier for a 20 ns pulsewidth at repetition rate of 20 KHz.

The layout diagram for studying the output spectrum of the single pass amplifier is shown in figure 4.2.
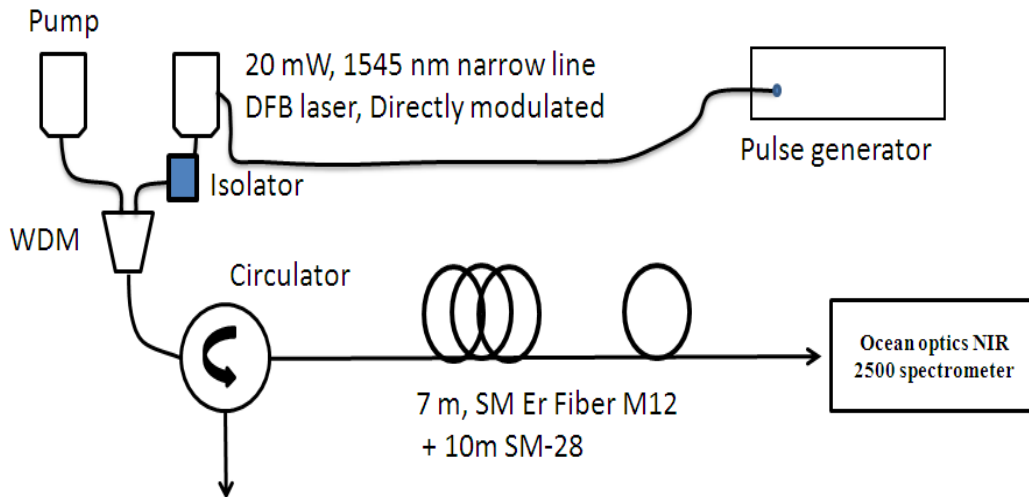
Figure 4.2 Experimental layout for recording the output spectrum of the single pass amplifier.

A circulator was spliced between WDM coupler and the M-12 fiber. The free end of the SM fiber was directed into an Ocean Optics NIR 2500 [112] spectrometer to record the output spectrum. The ocean optics spectrometer used has an optical resolution of 9.5 nm with 25 μm slit width. The pump current was kept at 450 mA (100 mW) and the repetition rate was kept at 12 KHz with a pulse duration of about 400 ns. The input seed pulse magnitude was increased by changing the function generator voltage and the corresponding changes in the output spectrum were recorded which are shown in figure 4.3.
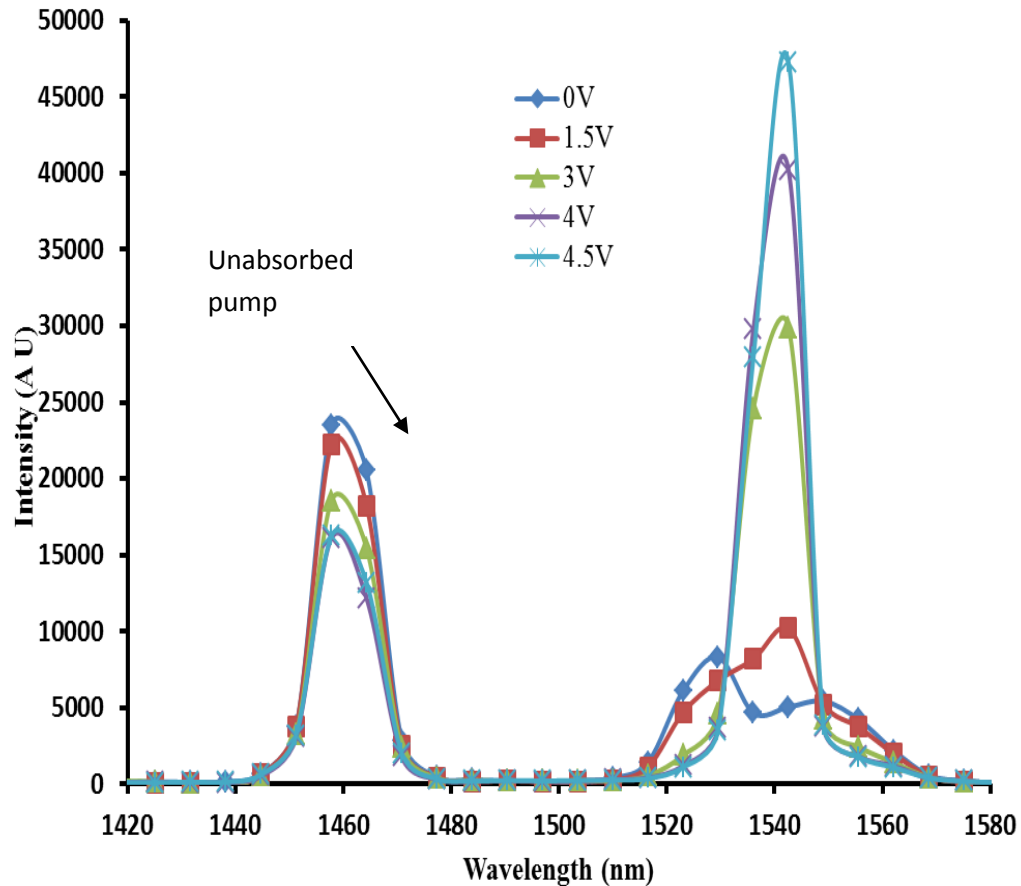
Figure 4.3 Output spectrum at different input signal levels as a function of the function generator voltage.

It is clear from the figure 4.3 that as the input voltage of the function generator increases the corresponding output also increases and the amount of unabsorbed pump drops. When the function generator voltage is 0 V, there is no input pulse so we have only unabsorbed pump and the 1545 nm output is not observable. At this time we have only broad ASE as output centered at 1530 nm. As the input voltage increases the amplified pulse appears and increases. For 2 V, E_{in} =0.06 nJ in energy the pump peak has dropped and there the output pulse appears at 1545 nm. At this stage the surrounding ASE is suppressed by the amplified seed pulse. When the function generator voltage is 3 V, a strong output pulse is observed at 1545 nm and the surrounding ASE and the pump peak have dropped more. With further increase of the function generator voltage to 4 V, the 1545 nm pulse grows even more. The measured output linewidth corresponds to the optical resolution of the spectrometer. The output pulse spectrum also depends on the input seed pulse width and the repetition rate in time. As the pulse width is decreased for a given driver voltage the narrow width output pulse is found to decrease in energy and the remaining pump energy in the 1480 nm peak becomes bigger.

After the single pass measurements the double pass first stage amplifier was implemented by splicing a 2 nm FBG with the free end of the SM fiber as shown in figure 3.1. In order to improve the efficiency of the EDFA various system configurations have been proposed to increase the EDFA gain and to reduce the noise figure [113, 114] and the techniques based on double pas amplification have been found to be quite efficient to improve the features related to the amplifier gain [115, 116]. Several devices can be used to reflect the optical

signal, such as fiber Bragg gratings (FBG), fiber mirrors and Faraday rotator mirrors [117, 118]. In the present work, initially a lens and a mirror combination was used to reflect the signal back into the Er fiber. A 15 mm focal length aspheric lens with IR coating was used to focus the light onto an Al mirror. The reflected signal traveled back into the Er fiber and the output was observed through the third port of the circulator. Later the lens and mirror combination was replaced with a 2 nm fiber Bragg grating with centre wavelength at 1544 nm. But it was observed that still there is some portion of ASE present along with the main pulse after the second pass of the amplifier. Another band pass filter was spliced onto the output end of the circulator to remove some of this ASE signal. The typical oscilloscope trace of the output of the first stage amplifier at a repetition rate of 10 KHz and pulse duration of under 20 ns (FWHM) is shown in figure 4.4. The bandwidth of the oscilloscope is about 60 MHz. The reflective-EDFA scheme can also be an effective means of cancelling out any polarization dependency of the amplifier characteristics caused by polarization hole burning and polarization dependent gain if it adopts a Faraday rotating mirror [119]. However this was not done in the present case.
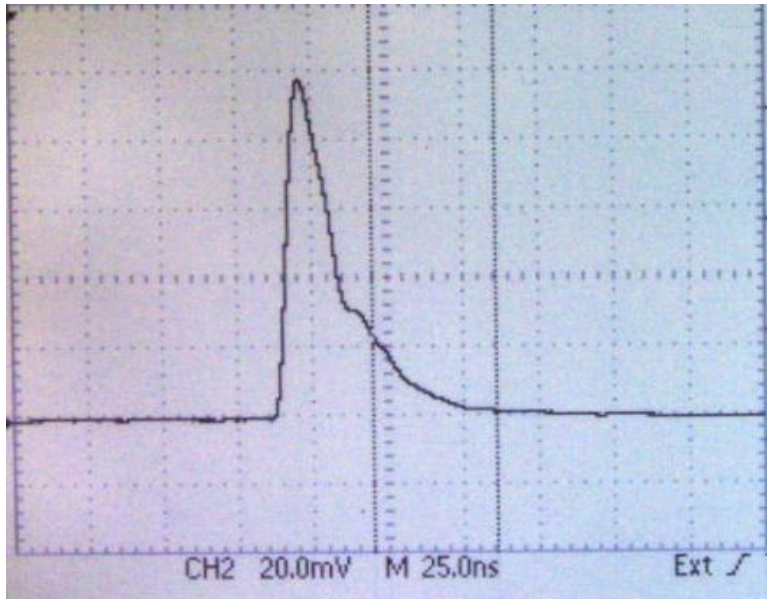
Figure 4.4 Oscilloscope trace of the output pulse of the first stage amplifier measured with a high speed InGaAs photodiode, the vertical scale is 20 mV/div and the horizontal scale is 25 ns/div.

4.1.2 Build Up of ASE

The presence of ASE in the output of the first stage amplifier can effectively reduce the signal gain so it needs to be filtered before going to the second stage amplifier. Band pass filters have been widely used for the filtering of ASE [120, 121]. Recently S S Pathmanathan et al [122] has demonstrated that an average improvement of 14 dB across the signal wavelength range at the input signal power of -50 dBm upon implementation of tunable band pass filter. In the present work it has been found that the use of band pass filter between two stages effectively reduces the ASE. To estimate the ASE an InGaAs photodiode with 300 ns rise time (Edmund Optics Part # MT55-754) was used to measure the output pulses and the output of the photodiode was connected to the oscilloscope

to display the laser pulse. The oscilloscope trace of the first stage amplifier at different conditions is shown in figure 4.5.
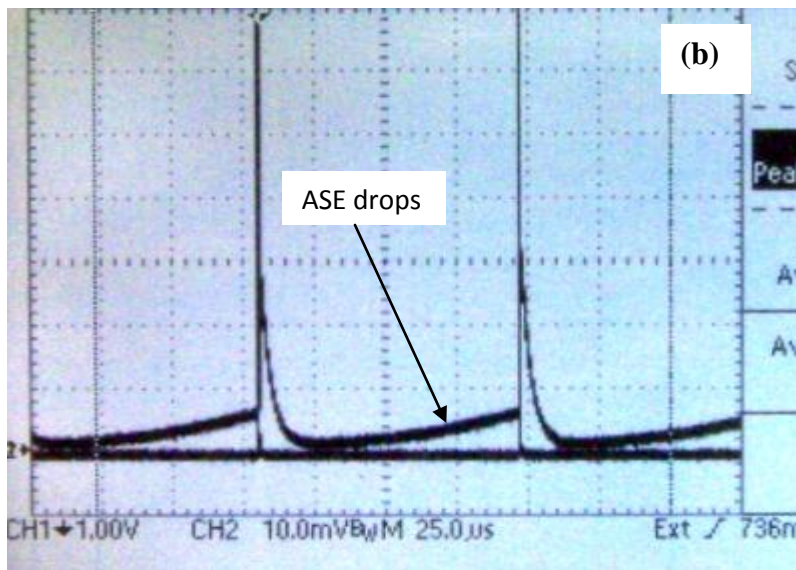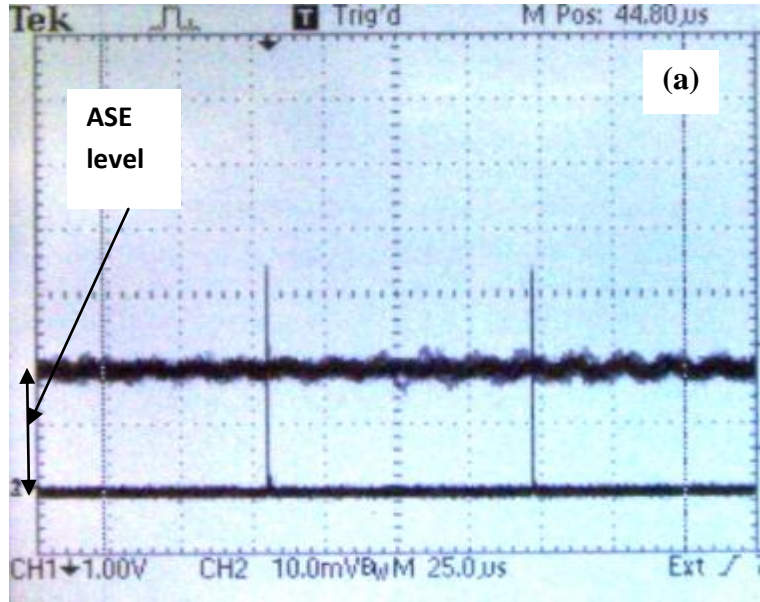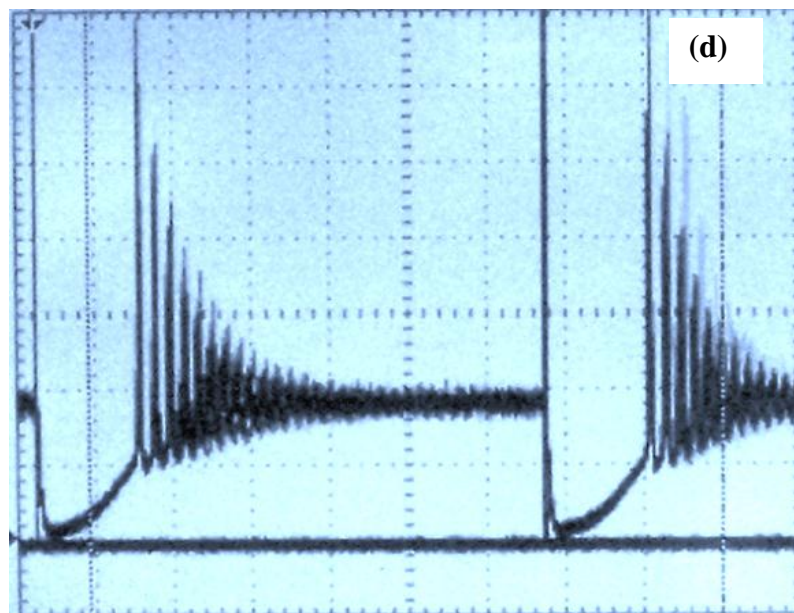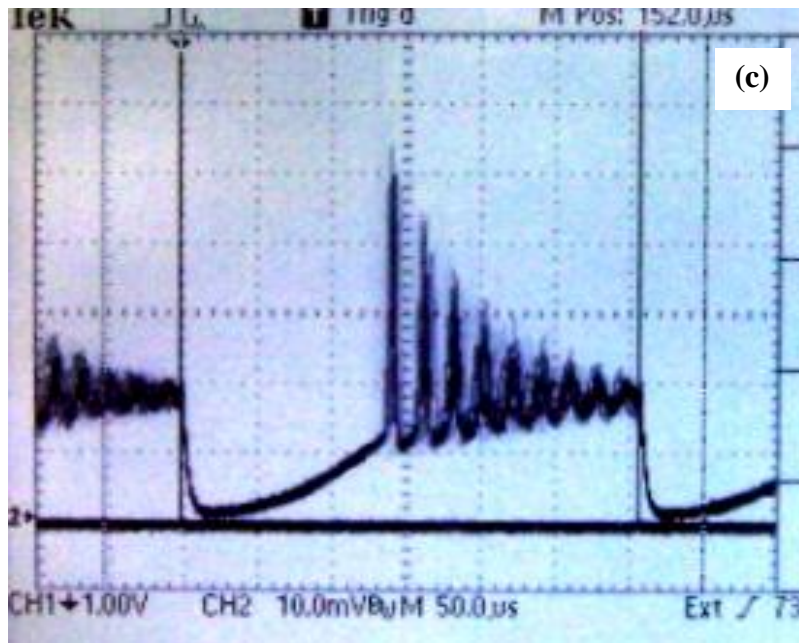
Figure 4.5 Oscilloscope trace of the of the first stage amplifier at different repetition rate (a) 0 KHz i.e. without seed pulse giving only ASE, the horizontal scale is 25 μs/div; (b) at 10 KHz, horizontal scale is 25 μs/div; (c) 3.5 KHz, horizontal scale is 50 μs/div; (d) 1.5 KHz, horizontal scale is 100 μs/div. The vertical scale for all cases is 10 mV/div, the input pulsewidth was 25 ns, the output pulse energy was about 5 μJ with the pump current of 450 mA (120 mW). The bandwidth of the oscilloscope is 60 MHz.

Figure 4.5 (a) shows the oscilloscope trace when there is no seed pulse and we have only ASE and as the seed pulse is injected (Fig. 4.5(b)) the ASE level drops a lot and it was estimated that still the 1/6 the of the total pulse energy is ASE. The output pulse was studied as a function of repetition rate and it was found that as the repetition rate is reduced then relaxation oscillations start to build up as shown in figure 4.5 (c) and 4.5 (d). It has also been observed that as the pump current was increased the oscillations start to build up with high pump current. So the pump current was kept at the value lower that value of about 450 mA. The repetition rate was also fixed at 10 KHz to avoid these oscillations. The variation of the short pulse output power of the first stage amplifier along with the estimated ASE power as a function of pump power is shown in figure 4.6.
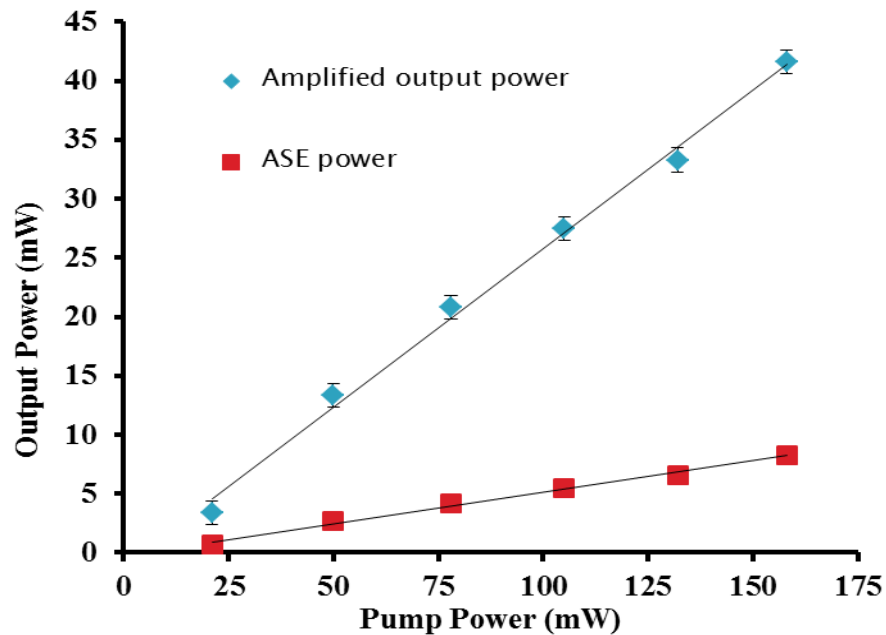
Figure 4.6 Variation of short pulse output power with pump power at fixed input energy of 0.40 nJ for the first stage double pass configuration with ASE filters at a repetition rate of 10 KHz.

It was observed that the ASE and the amplified output power linearly depend on pump power. The input seed pulse energy is kept constant at ~ 0.40 nJ. The maximum output power obtained for the final double pass first stage amplifier is about 50 mW with pulse width of 20 ns at repetition rate of 10 KHz. The full pulse energy every 0.1 ms pulse energy was estimated using this output power and the repetition rate and it is found to be about 5 µJ. The ASE was measured to be about 1/6 of this value and so we had about 4 µJ in the amplified output pulse. The double pass gain of the first stage amplifier is was thus found about 40 ± 3 dB.

This 40 dB gain is in good agreement with the reported values of the typical EDFA gain with the fiber lengths of 10-14 m where the a value of 35 - 42 dB [123, 124] was reported.

4.1.3 SBS Pulse Generation

For sub microsecond pulses with single spatial mode and very narrow line width, scaling to high pulse energies has been difficult in fiber amplifiers due to limitations primarily from the stimulated Brillouin scattering (SBS) effect [125, 126] and potential high intensity damage in the fiber. In the present set up after replacing the mirror with the fiber Bragg grating SBS pulse generation was also observed. The typical layout of the fibers and pulse generation is shown in figure 4.7.
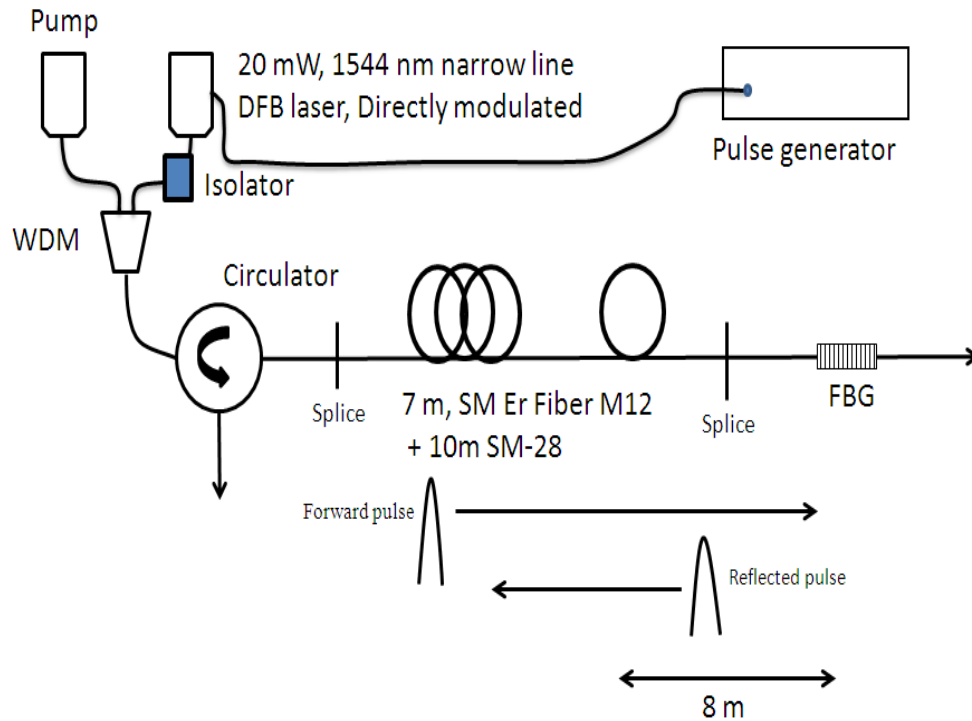
Figure 4.7   Layout of the SBS generation in the fiber.

In our case the total length of the fiber between the circulator and FBG is about 19 m (7 m EDF + 10 m SMF + 2 m fiber pigtails). The SBS pulse was generated when the amplified pulse was travelling towards the circulator in the backward direction after reflected from the FBG at a distance of approximately 8 m as shown in figure 4.7. An example of an oscilloscope trace of the output of the first stage amplifier with a delayed SBS pulse reflection is shown in figure 4.8. The SBS pulse is very narrow (about few ns) and exhibit large amplitude fluctuations.
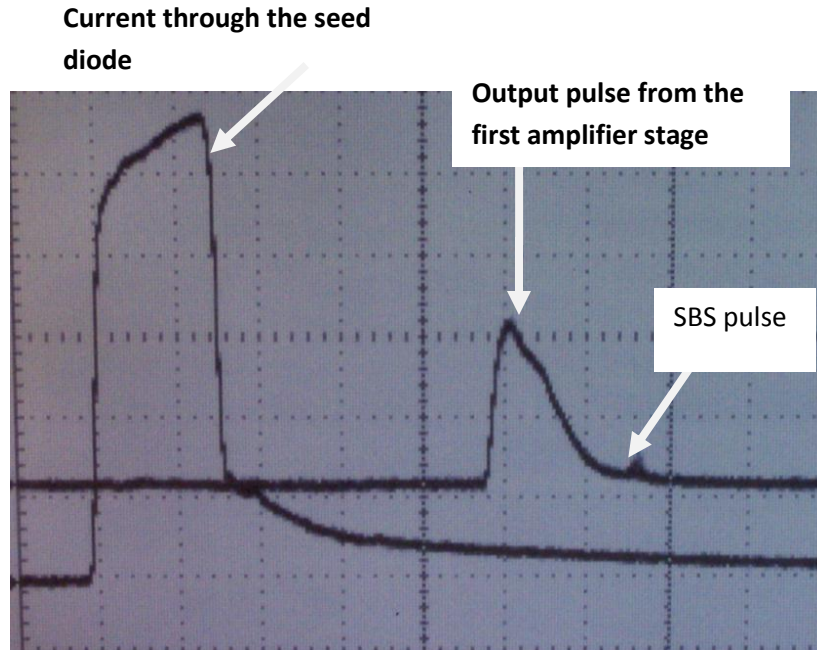
Figure 4.8 First stage amplifier output with SBS pulse with the pulse generator voltage of 5 V, pump current 450 mA and at a repetition rate of 4 KHz. The horizontal scale is 50 ns/div.

The Brillouin threshold is found to occur at a critical pump power which can be approximated by [127].

$$P_{cr} \approx \frac{21\, A_{eff}}{g_B\, L_{eff}} \tag{4.2}$$

where g_B is the peak value of the Brillouin gain and A_{eff} is the effective core area and L_{eff} is the effective interaction length which is lesser of the source coherence length, pulse duration and fiber length. In our case the maximum value of the L_{eff} is determined by the length of the fiber used in the first stage amplifier and is equal to 19 m. For the typical fibers used in 1550 nm optical

communications we have $g_B= 5\text{x}10^{-11}$ m/W and $A_{eff} = 50$ µm^2. In our case the effective interaction length is calculated as

$$L_{eff} = \frac{\tau_p\, c}{n} \tag{4.3}$$

Where τ_p is the pulse width, c is the velocity of light and n is the refractive index. For a laser pulse width of 20 ns we get the effective length of about 5 m. By putting all the values in equation we get P_{cr} = 150 W. The energy of the output pulse of first stage amplifier is about 4 µJ, so peak power is 200 W for a pulse width of 20 ns which is more than the SBS threshold. The temporal resolution of photodiode was measured with femtosecond light source (Spectra Physics Hurricane Mai-Tai tunable laser). The response of the photodiode for a fs pulse is shown in figure 4.9 with a pulsewidth of approximately 600 ps (FWHM) and a rise time of around 400 ps (10-90%). The bandwidth of the oscilloscope is about 1 GHz.
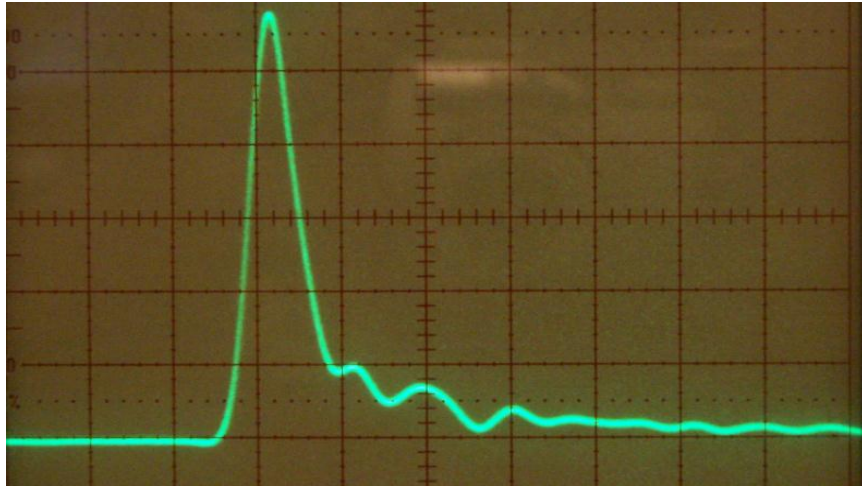
Figure 4.9 Temporal response of InGaAs photodiode, Horizontal scale is 1 ns/div and vertical scale is 20 mV/div.

The output pulse shown in figure 4.8 is much longer than the response time of photodiode so we observed the real pulse shape. As one can see from the equation 4.2 that the SBS pulse formation can be controlled by varying the pulse length. The variation of SBS pulse with the pulse duration of the seed pulse has been studied and is shown in figure 4.10.

(a)

500mV

(b)

20nS

500mV

(c)
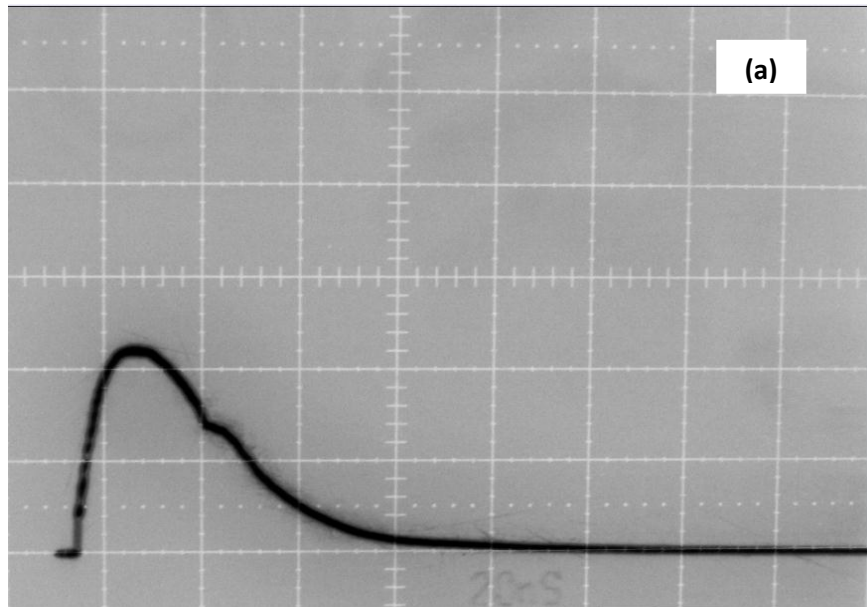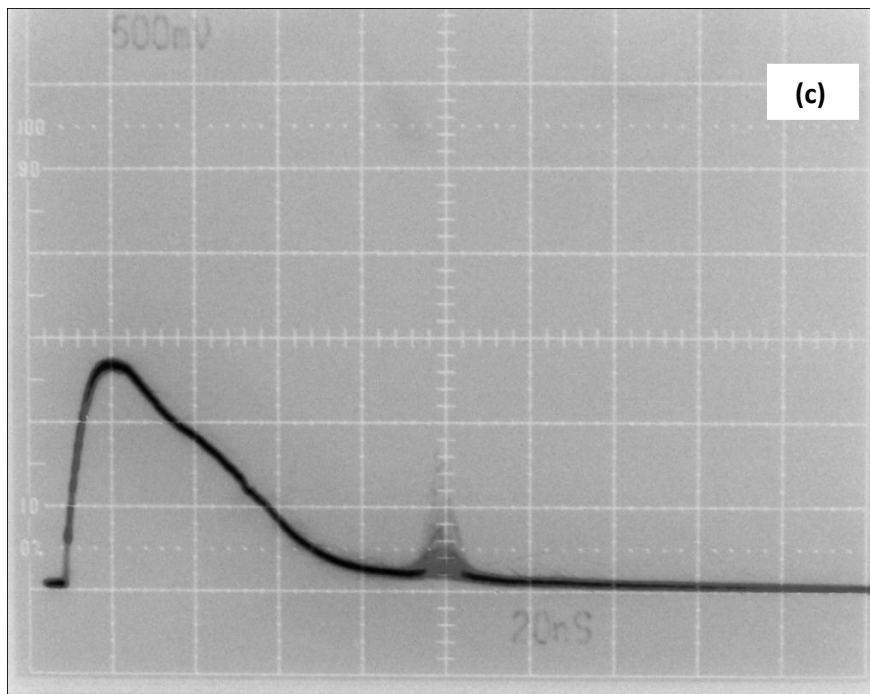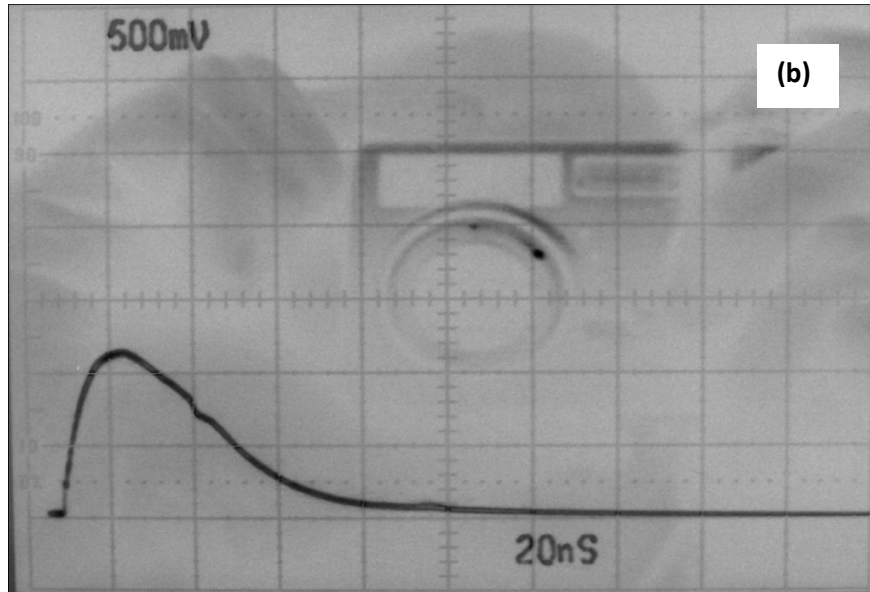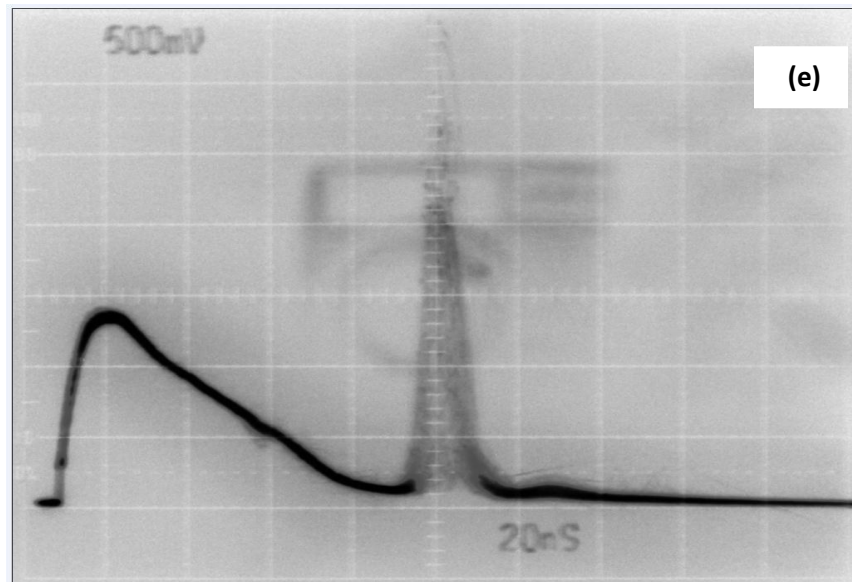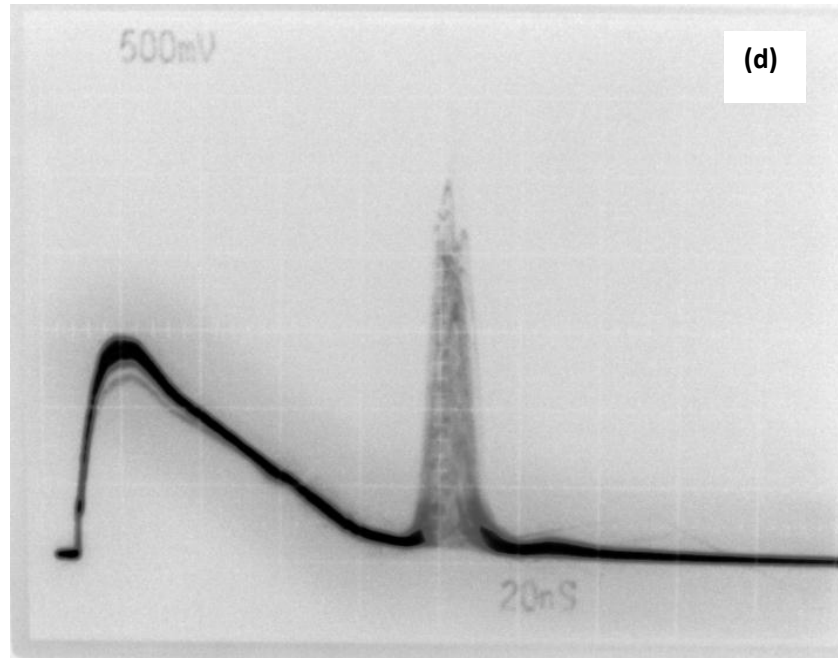
20nS

Figure 4.10 Measured output pulse for the double pass amplifier showing the late time SBS pulse as a function of the durations of current pulse through the seed diode (a) 60 ns; (b) 70 ns; (c) 80 ns; (d) 100 ns; (e) 120 ns; at the repetition rate of 3.2 KHz. Scale: 20 ns/div.

It is clear from the figure 4.10 that as the seed pulse duration is increased the SBS

pulse becomes more and more prominent. It can be justify from the equation 4.3

as the pulse duration is increased the interaction length increases which in turn decrease the SBS threshold power. SBS builds up strongly in the fiber for narrow linewidth pulses of long pulse duration [128]. Figure 4.11 shows the variation of SBS pulse with the repetition rate at fixed pulse duration.
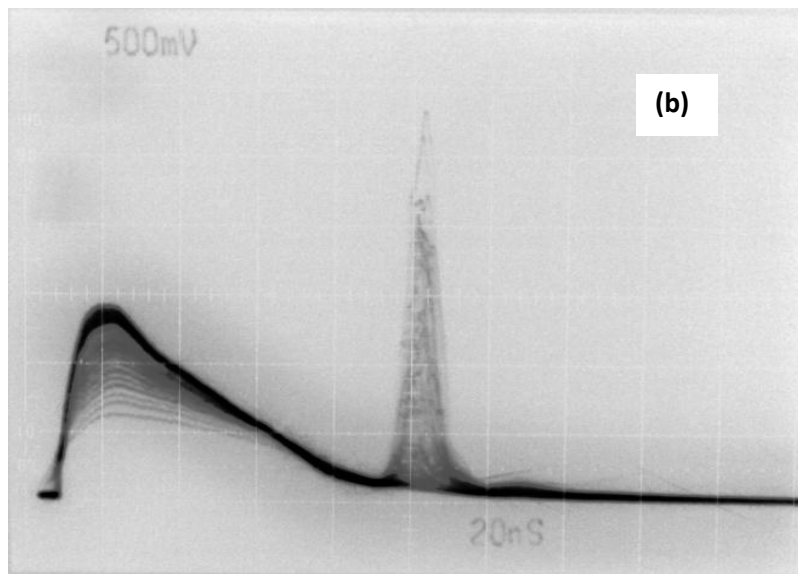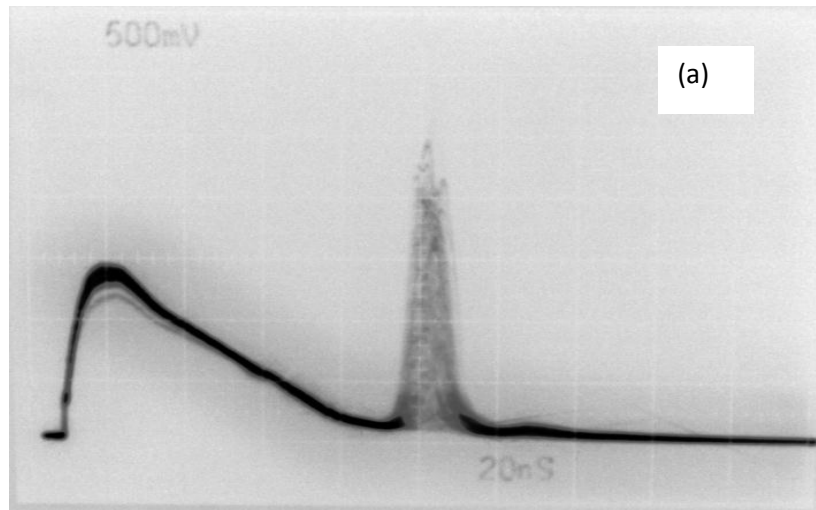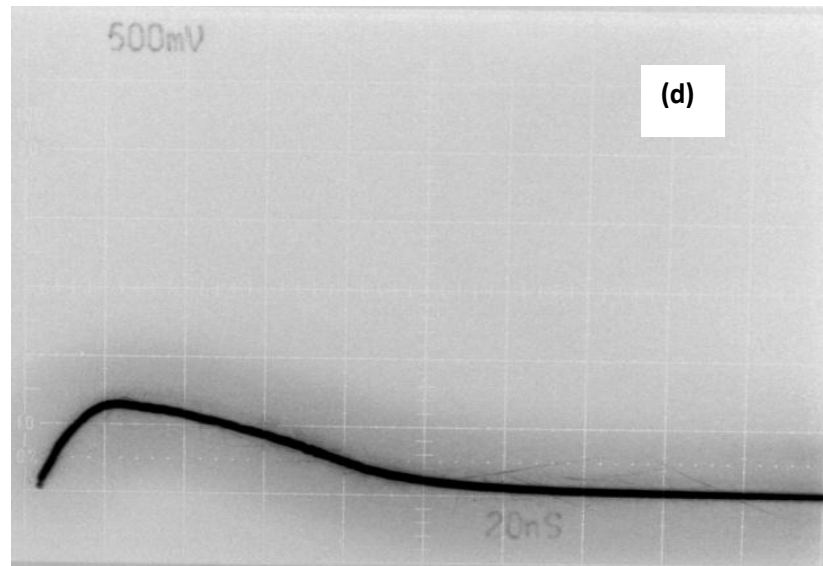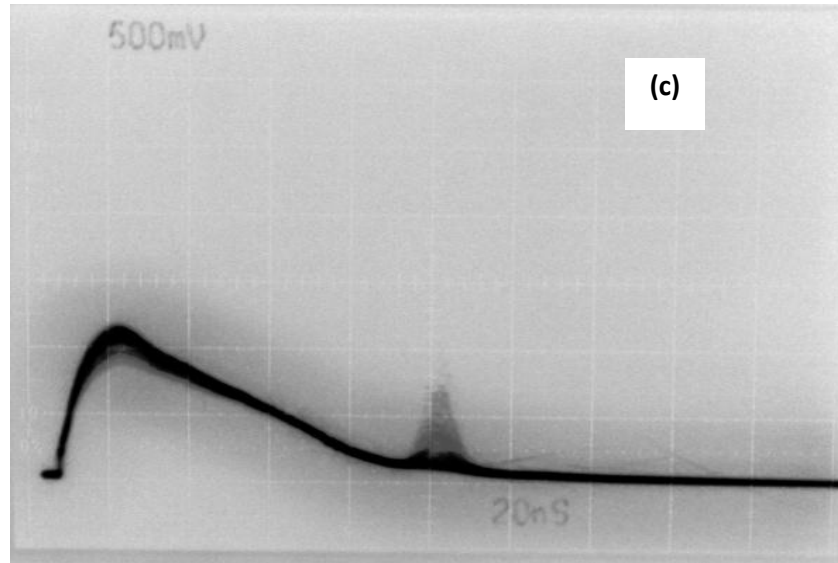
Figure 4.11 SBS pulse at different repetition rates (a) 4 KHz; (b) 5 KHz; (c) 6.5 KHz; (d) 10 KHz, at a seed pulse current driver width of 120 ns. Horizontal Scale: 20ns/div, vertical scale 500 mV/div.

It was observed that as the repetition rate increases the SBS pulse drops and at a repetition rate of 10 KHz it has almost disappeared. As the repetition rate is increasing the output pulse also drops and becomes broader. It is because as the repetition rate increases the gain and the intensity drops due to a reduced amount

of stored energy between extraction pulses. It is known that the peak power of the laser pulses can be increased by pulse compression via SBS [129]. In the present work to achieve more peak pulse power, first we tried to work with the SBS pulse. But after some time damage was observed in the fiber which can be due to the high intensity SBS pulse. The main drawback of pulse compression with the SBS is poor pulse stability, the temporal jitter in the precise pulse repetition rate and the frequent damage owing to occasional higher power pulses with a peak power exceeding the silica damage threshold [130]. Keeping these drawbacks in consideration the pulse width and the repetition rate were optimized so that the SBS pulse is suppressed and we have only the amplified 1545 nm seed pulse.

4.2 Second Stage Amplification

The output from the first stage amplifier was combined with the power amplifier for further amplification. The laser pump diode for this amplifier is a fiber coupled laser diode as described in section 3.2.5. The experimental schematic used for the second stage amplifier is shown in figure 3.9. The output of the first stage amplifier is first passed through a 5 nm band pass filter and the output of the band pass filter is fusion spliced to the manual polarization controller. For the second stage amplification 3 m of LMA-PM Er/Yb fiber was used as the gain medium. The large mode area fibers allow near single mode operation in multimode fiber and are crucial for obtaining the highest possible peak powers and pulse energies in fiber systems [131]. Also the large mode area core designs

facilitate higher pulse energy and power handling (e.g. larger area reduces facet damage threshold), reduce nonlinearity (increased thresholds with mode areas), have high energy storage, facilitate efficient pump absorption and can reduce device lengths. In the present work the large mode area fiber was spliced with the output end of the polarization controller. This time the splice joint was kept in the air to avoid the excessive heat build up by the surrounding materials due to leakage of unabsorbed pump. A coupling lens of focal length   8 mm was used to couple the pump light into the fiber through a dichroic mirror. The output of the second stage was displayed onto the oscilloscope with the help of photodiode and the typical output pulse is shown in figure 4.12.
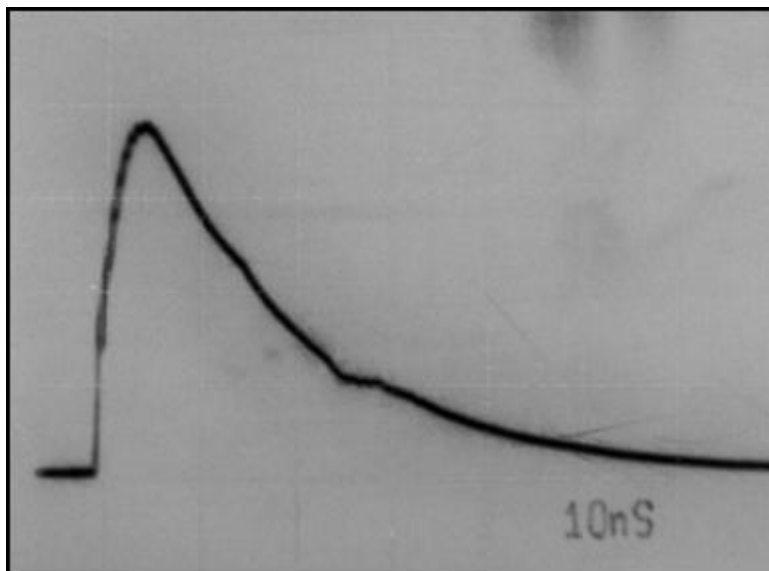
Figure 4.12 Oscilloscope trace of the second stage amplifier with the input pulse energy of 4 μJ from the first stage amplifier with the 1480 nm pump current of 450 mA. The pump current for the second stage was 17.5 A and repetition rate was 10 KHz. Horizontal time scale is 10 ns/div.

The output pulse was about 16 ns FWHM and its amplitude increased with the pump current, but after a certain value of pump current of around 18 A it started to reduce. The pump current and pump temperature were optimized for the maximum output power.

The output pulse power was recorded at different repetition rates and the pulse energy was calculated from the output power. The output pulse energy as a function of repetition rate is shown in figure 4. 13.
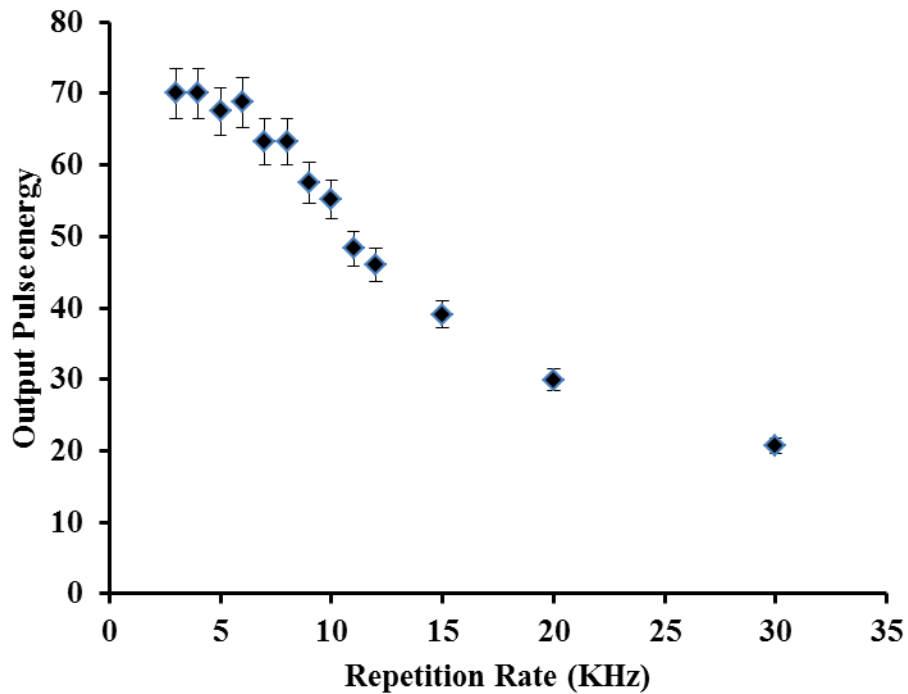
Figure 4.13 Amplified Pulse energy versus Repetition rate with the input pulse energy of 4 µJ from the first stage amplifier and the pump current for the first and second stage was 450 mA and 17.5 A respectively.

It is clear from the figure 4.13 that the pulse amplitude is higher at low repetition rate in comparison to high repetition rate. But on the other hand at low repetition rate we observed formation of SBS pulses as described in the section 4.1.3. Cames et al [132] also reported the same trends for variation of gain with the repetition rate. They observed an exponential decrease of the gain after 10 KHz. In their work they discussed two stage optical amplifiers. The first stage used a reflective configuration where a signal is amplified twice in the same EDF and the second stage worked as a high power amplifier. The input pulse had a duration in the range of   1 to 50 ns, with wavelength equal to 1549.1 nm. With an input pulse power of 1.5 mW, the amplifier provided 70 mW in output power at a repetition rate of 1 KHz.

For these measurements the pump current was 17.5 A and the temperature of the pump laser diode was set at 22.3^{o}C. Although a filter was used to reduce the ASE at the output of first stage, still there was some ASE left which was further amplified in the second stage amplifier. The ASE fraction in the output power was estimated with the same technique as explained for the first stage amplifier. The maximum output power after the second stage amplifications was measured using a power meter and it was about 550 ± 30 mW at 10 KHz. At this point the ASE was estimated about 1/6 of the total power value. In output we expected that we had about 90 ± 30 mW at 10 KHz power in ASE and unabsorbed pump. Thus the amplified short pulse output power is about 460 ± 50 mW at 10 KHz. Thus the total energy was estimated to be about 46 ± 5 µJ at the repetition rate of 10 KHz for an output pulse duration of 16 ns. The gain for the second stage amplifier is

about 11 ± 3 dB. The overall gain of the both stages is about 51 ± 3 dB. H Takara et al [133] reported the an overall gain of 49 dB in a two stage EDFA with a peak pulse energy of 1.05 nJ and peak pulse power of 105 W. With almost the same experimental layout a gain of 47 dB has been reported by Cames et al. [132].

4.3 Frequency Upconversion

Frequency doubling was achieved with the help of a PPLN crystal (Thorlabs). The crystal was already mounted on a copper base for easy handling. According to the specification of the crystal, it can be heated up to 180^0C to achieve the quasi phase matching condition. For heating the crystal a homemade crystal holder was employed as shown in figure 4.14. Teflon was used to make the crystal holder so that it could be heated up to 200^0C. The crystal holder was mounted on a translational stage which provided the horizontal, vertical and rotational movements for the crystal. The crystal mounted on the copper clip was placed on a one Ohm resistor inside the holder and voltage was applied across the resistor to heat the PPLN crystal. The voltage and current through the resistor was increased slowly so that crystal heated up very slowly. According to the manufacturer's specification the crystal shouldn't be heated or cooled down at a rate greater than 10^0C/min. For monitoring the temperature a thin film Pt thermistor was glued on the corner of the copper clip. As the temperature gradient of copper is very small then the temperature difference between copper clip and the crystal is also very small. An aluminum foil was glued on the edge of the crystal holder as shown in

the figure 4.14 to physically enclose the crystal and avoid any physical damage to the crystal.
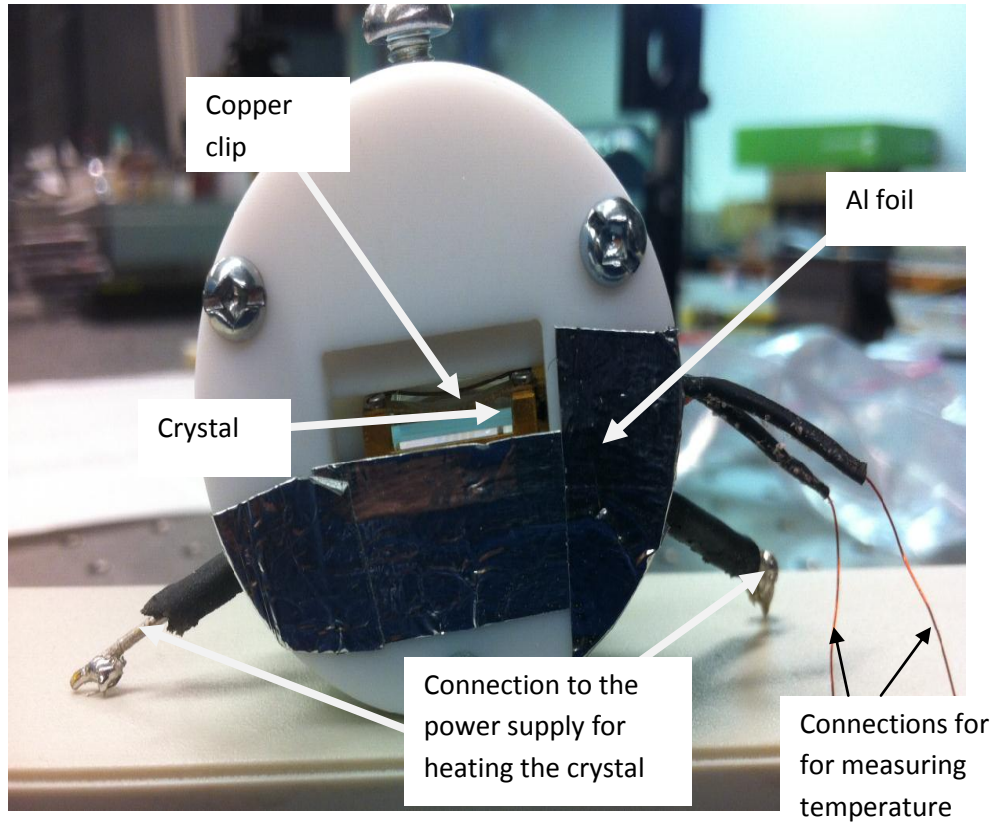
Figure 4.14 PPLN crystal holder with the heater

The output of the second stage amplifier was focused onto the PPLN crystal with the help of a 5 cm biconvex lens and the second harmonic output power was measured with the help of power meter. The temperature of the crystal was slowly increased and the corresponding change in output power was observed.

It was observed that as the temperature increased the output power of the second harmonic also increased. In our case we obtained maximum output at around 90°C. To block the fundamental pulse from the frequency doubled pulse a 3 mm

thick bandpass filter, RG9, from Schott Glass Technologies Inc. was used. This filter has exceptional properties for separation of frequency doubled pulse from the fundamental pulse. The transmission curve provided by the manufacturer for the RG9 filter is shown in figure 4.15.
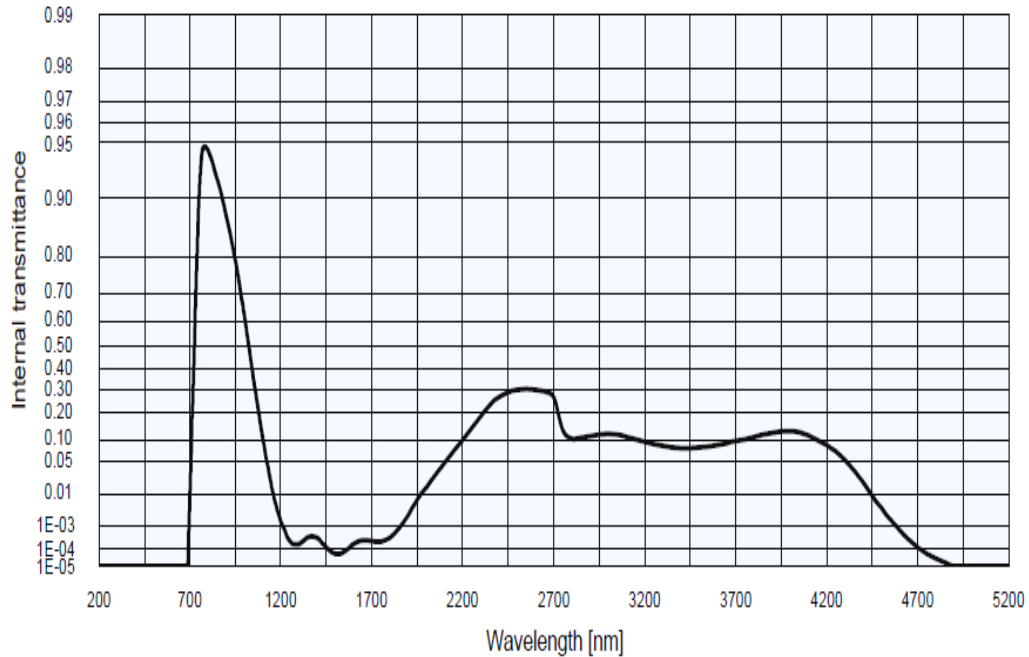
Figure 4.15 Transmission curve for a 3 mm thick the RG9 filter provided by the manufacturer (Schott Glass Technologies Inc.)

As the PPLN crystal has five separate conversion regions as explained in section 3.2.6, we selected the region with the best efficiency and then tuned it to the maximum second harmonic output by changing the temperature. Due to the time lag of the temperature tuning the fine adjustment was performed by mechanical tilting. By optimizing all the conditions we obtained about 15 μJ frequency doubled energy at a repetition rate of 10 KHz with fundamental pulse energy of

about 46 μJ at repetition rate of 10 KHz giving a conversion efficiency of 30%. The spectrum of the frequency doubled output pulse is shown in figure 4.16. The measured linewidth is due to the instrument resolution which is about 0.1 nm in this case.
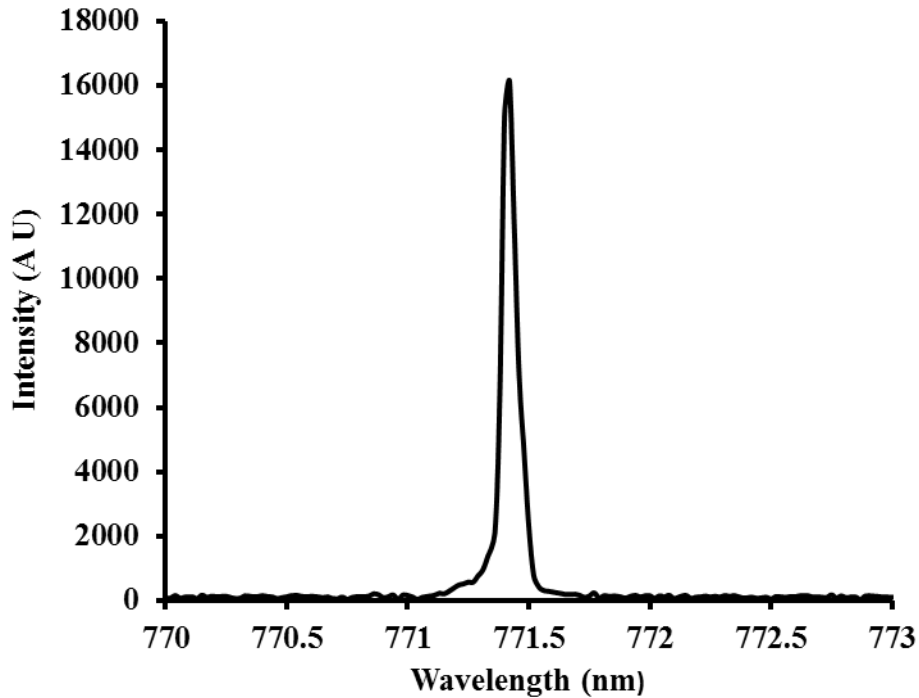
Figure 4.16 Frequency doubled pulse after passing through 10 mm long PPLN crystal temperature tuned at 90 C centered at 771.42 nm with the fundamental pulse energy of 50 μJ at a repetition rate of 10 KHz.

PPLN has been successfully demonstrated to give high efficiency second harmonic generation in a number of previous reports [134,135]. The theoretical value of the intensity of second harmonic pulse can be calculated using the following equation [136]:

$$I\left(2\omega\right) = \frac{2\pi^2\ L^2\ d_{eff}^2\ I^2\left(\omega\right)}{\lambda_F^2\ n_1^2\ n_2\ \varepsilon_0\ c}\ \text{sin}\ c^2\left(\frac{\Delta kL}{2}\right)\qquad(4.4)$$

Where $I\left(2\omega\right)$ is the intensity of second harmonic generated, $I\left(\omega\right)$ is the intensity of the input beam, d_{eff} is the effective nonlinear coefficient for the quasi phase matched LiNbO$_3$, Δk is the phase mismatch term, L is the length of the PPLN sample, λ_F is the wavelength of fundamental beam, n_1 and n_2 are the refractive indices of the PPLN crystal at the fundamental and the second harmonic wavelengths, respectively, ε_0 is the dielectric permittivity of the free space and c is the velocity of light in free space. For the first order collinear interaction the phase matching is achieved when Δk =0. For our calculations we consider L=10 mm (length of the PPLN crystal provided by the manufacturer), d_{eff} = 16.5 pm/V [136] for quasi phase matching, λ_F = 1545 nm, n_1, n_2 = 2.2. The beam spot diameter was estimated by measuring the ablation crater at the focal point of the focusing lens. This value is close to the value of beam diameter given by the estimation using geometrical optics approach, using the ratio of the focal length of the collimated lens which couples the pump radiation into the LMA fiber (8 mm) and the focusing lens which focuses the fundamental beam onto the PPLN crystal (50 mm). The beam spot diameter estimated this way was about 200 μm and the peak input power calculated for this case was 1.8 KW.

By using these values in equation (4.4) the energy efficiency is calculated to be about 40%. The experimentally measured frequency conversion efficiency of 30 ± 5 % is in good agreement with the theoretically calculated value. The difference in both values can be attributed to the non-uniform beam

diameter through the crystal length and loss of fundamental light while coupling into the AR coated PPLN crystal. Also the conversion efficiency is in good agreement with the already reported values in the literature for similar laser setups.

M A Arbore et al [137] reported efficient doubling of passively mode locked femtosecond erbium laser pulses. Quasi-phase matched second harmonic generation in periodically poled lithium niobate was used to generate 8.1 mW of 190 fs, 90 pJ pulses at 777 nm with the conversion efficiency of about 25%. The length of the PPLN crystal was 1.1 mm long and the fundamental pulse was focused with an achromatic doublet. The quasi phase matching condition was observed at around 80^0C which is near to the temperature observed in our setup. In an another experiment Gen et al [138] demonstrated the generation of quasi phase matching second harmonic generation in a 10 mm long PPLN crystal which generated 90.6 mW at 775.9 nm with a single pass efficiency of 14.7%. The pump source was built around a master oscillator power amplifier (MOPA) architecture which included two parts. One was a ring fiber structure and the other was an Er/Yb doped double clad fiber amplifier pumped by a stack of 980 nm diode lasers. Driven at full power, the MOPA system produced maximum output power of 2.18 W over a tunable wavelength range 1535-1570 nm. It has also been demonstrated that the efficiency could be improved if the two PPLN crystals were used in place of one crystal [139]. In that experiment they observed that the doubling efficiency was enhanced with two crystals due to the presence of the second harmonic light from the first crystal acting as a seed for the second.

The frequency doubled output from the PPLN crystal was further focused onto the BBO crystal for frequency quadrupling as explained in the section 3.2.6. For focusing the frequency doubled output into the BBO crystal different coupling lens were tried and it was found that with a 10 cm biconvex lens the output was maximum. The frequency quadrupled output was measured with the help of an 818-UV Low-Power UV Enhanced Silicon (Si) Photo detector [140]. The photodiode was connected to the oscilloscope to display the output waveform. After focusing the light onto the BBO crystal, it was rotated until the phase matching angle was achieved and the output was maximum. The frequency quadrupled energy was estimated by using the total area under the curve for the output waveform displayed on the oscilloscope and the manufacturers reported detector sensitivity. The estimated output energy after frequency quadrupling was about 1μJ. The frequency quadrupling conversion efficiency is thus about 7% which is in good agreement with the efficiency reported in literature for the BBO crystal. The conversion efficiency of about 6.4% has been reported by Fan et al. [141]. In their work, an efficient, all-solid-state 335.5-nm source based on a frequency quadrupled, Q-switched, diode-pumped Nd:YVO$_4$ 1342-nm laser was demonstrated. A 63 mW average output power at 335.5 nm was obtained with a BBO crystal at the absorbed pumping power of 6.3 W and the pulse repetition rates of 10 kHz. The single pass frequency conversion efficiency was 6.4% for frequency quadrupling.

The output spectrum of the frequency quadrupled output was recorded with the help of a 0.35 m McPherson monochromator which has a 1200 lines/mm

grating and an adjustable slit with a slit width which can be varied from 5 to 4000 microns. The monochromator has an effective aperture of f/4.8 and dispersion of 2 nm/mm when using a 1200 lines/mm grating and was equipped with a model 789A scan controller from McPherson. The detector used was a cooled charge-coupled device (CCD) array (ST6-SBIG, Santa Barbara Instrument Group), the detector size is 8.6x6.5mm and the pixel size is 23x27 μm. In our case we used the minimum slit width of 5 microns. An example of the spectrum of the frequency quadrupled output is shown in figure 4.17.
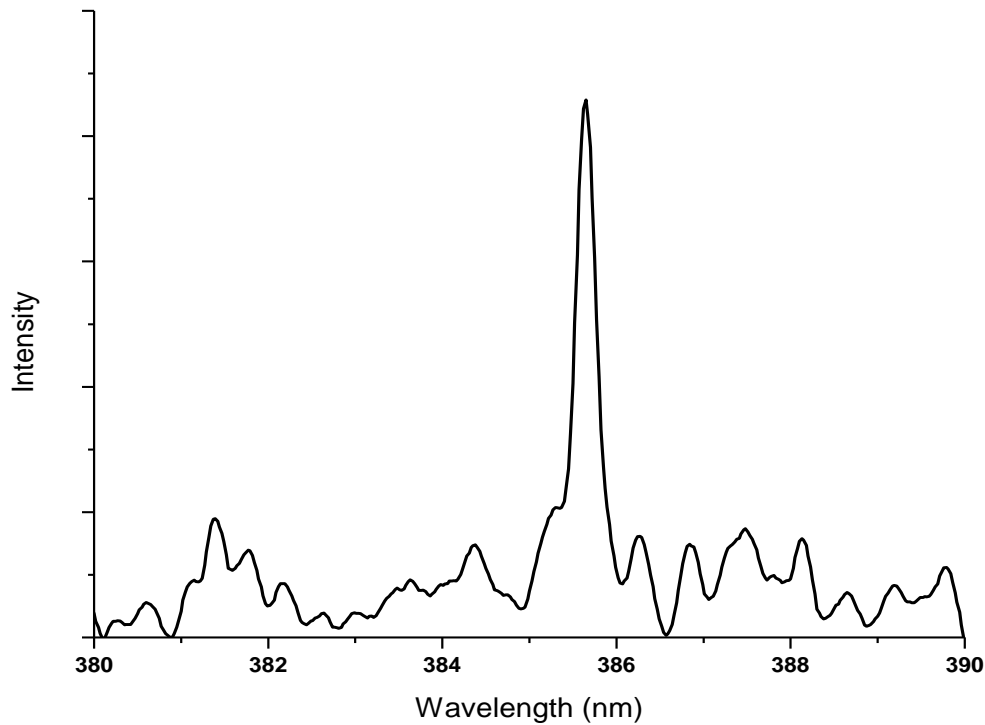
Figure 4.17 Frequency quadrupled output spectrum with the input frequency doubled pulse energy of 15 μJ after passing through BBO crystal (the data from the CCD array was smoothed using FFT filtering).

4.4 Wavelength Tuning of the pulse

There is a linear relationship between temperature and the center wavelength of a laser diode. As the temperature increases the center wavelength of the laser diode increases. This characteristic is useful in spectroscopic applications where the wavelength of emission of the laser diode can be accurately temperature tuned to the specific properties of the material with which it is interacting. The aim of the temperature tuning in our setup is to tune the seed laser diode so that the frequency quadrupled laser wavelength is equal to the resonance wavelength of some useful element. This way we can perform dual pulse LIBS for the detection of elements. The wavelength tuning of the seed laser diode was performed by changing the temperature of the seed laser diode. To measure the output spectrum the frequency doubled laser pulse was used. The frequency doubled laser light was coupled into a long fiber and the output light from the other end of the fiber was focused into the McPherson monochromator. Then the temperature of the seed laser was changed by the temperature controller of the seed laser diode and corresponding shift in the wavelength was recorded. The shift in the center wavelength of frequency doubled pulse with temperature is shown in figure 4.17. From figure 4.18 one can see that the wavelength of the second harmonic pulse changes from 771.11 nm to 771.96 nm which corresponds to the tuning range of the seed laser diode from 1542.22 nm to 1543.92 nm. This is the limit of the tuning as beyond this range the output intensity dropped to large extend. The wavelength shift of the fundamental pulse with the temperature is shown in figure 4.19. The observed temperature tunability from the figure 4.19 for the

fundamental pulse is about 0.08 ±0.004 nm/C which is in reasonable agreement with the value of wavelength temperature tunability (0.07 nm/C) given in the specification sheet for the seed laser diode.
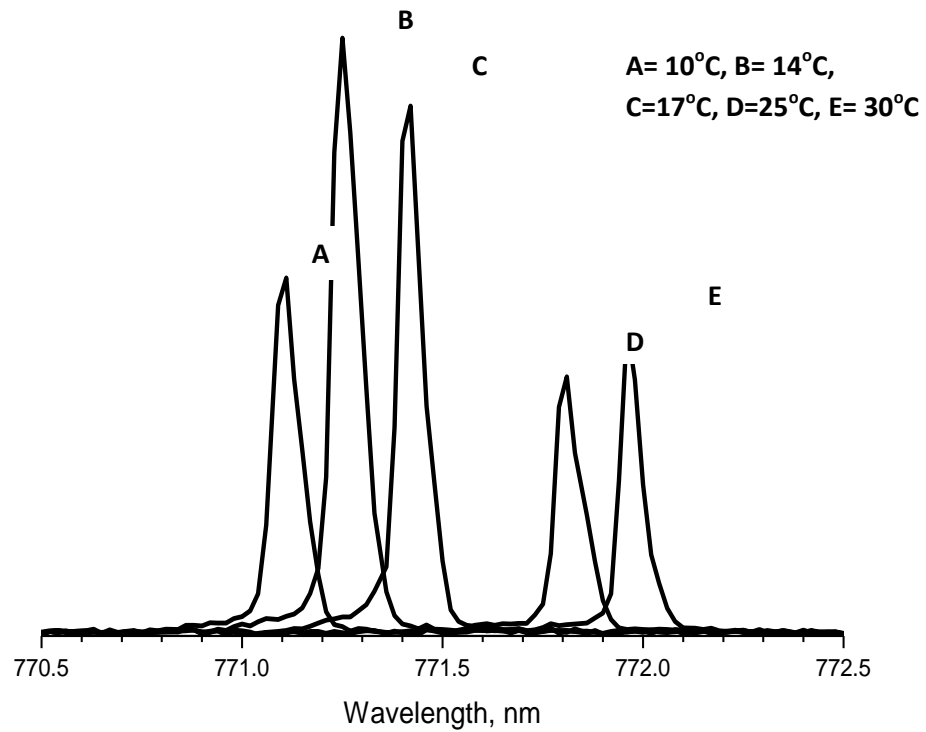
Figure 4.18 Wavelength shift the frequency doubled pulse with temperature
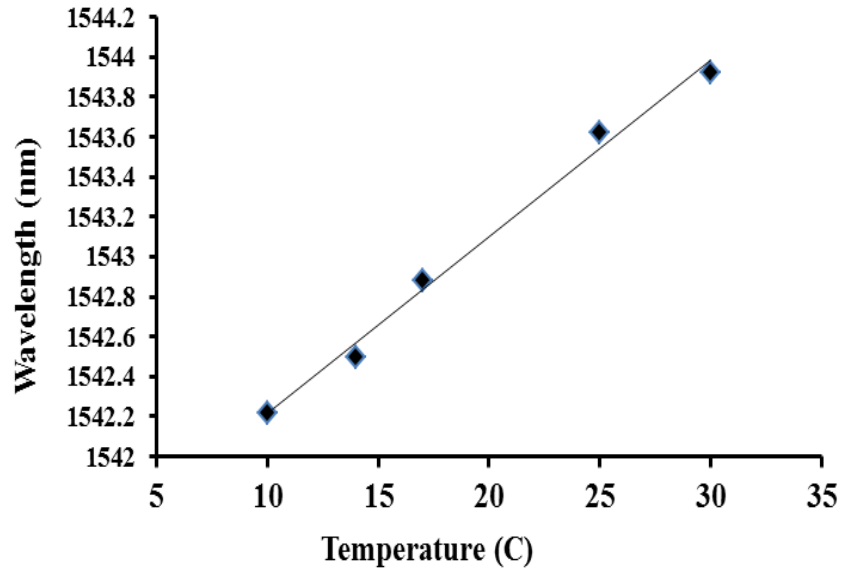
Figure 4.19 Wavelength tuning of the Seed laser diode Shift of the wavelength with temperature with the fundamental pulse energy of 50 μJ and repetition rate of 10 KHz.

At the edge of this tunability range it is possible to tune the seed laser diode so that the frequency quadrupled output is equal to the resonance absorption line of Fe i.e 385.63 nm. As explained in section 3.1.5 the fiber Bragg grating used in the experimental setup is quite narrow, with a bandwidth of 2 nm which makes the wavelength tuning range also narrow. In the pulsed operation the linewidth becomes broader because of the time bandwidth product. The time–bandwidth product of a pulse is the product of its temporal duration and spectral width (in frequency space). The minimum possible time–bandwidth product is obtained for bandwidth-limited pulses. For example, it is ~ 0.315 for bandwidth-limited sech^2-shaped pulses and ~ 0.44 for Gaussian-shaped pulses. So for a given pulse

115

duration, there is a lower limit for the spectral bandwidth. This limitation is essentially a property of the Fourier transform. As the fundamental pulse (probe pulse) is shortened to a few ns, so according to time-bandwidth product its bandwidth must increase to the range of a GHz.

Other C- band tunable laser diodes are available with a tunability of 40 nm from 1528 nm to 1563 nm which gives 20 nm tunability at frequency doubled and 10 nm at frequency quadrupled wavelengths. Thus by using such a wide range tunable source one could increase the number of elements which could be detected with the LA-LIF setup.

4.5 LIF Results

To show the applicability of the present setup for the LA-LIF application, first the fundamental pulse was tested for the ablation of the different targets. The amplified output energy obtained in present work was sufficient for the ablation of different target materials that were tried. It was found that the output laser pulse could ablate iron, copper, rubber and aluminum. For the test of ablation a short focal length lens (18 mm) was employed for focusing light onto the target surface and then the target was moved transversely in front of the laser beam. Later it was found that the back reflection from the target which initiates the generation of SBS damaged the LMA fiber end (where the LIMO diode pump laser entered) and it was cleaved again. The mode quality of output pulse was improved by suppressing the higher order modes by making a figure 8 shaped loop of the LMA

fiber which introduces the bending losses for the higher order modes. Some of the ablated material pictures are shown in figure 4.20.
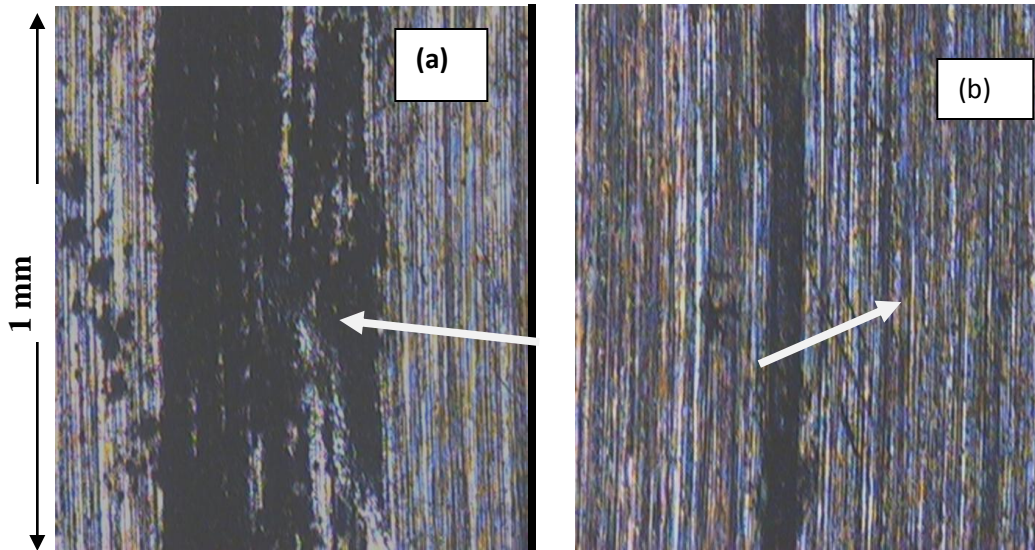
Figure 4.20 Laser ablation tracks caused by fundamental pulse (a) Aluminum (b) Iron with pulse energy of 50 µJ focused with a short focal length (18 mm) lens.

The target materials chosen were standard bulk pieces of metal and were not polished so they exhibit a rough and scratched surface. The fundamental pulse together with harmonic pulses was tested for the plasma generation using the schematic described in figure 3.16. The fundamental pulse at 1545 nm with 50 µJ, frequency doubled pulse with 15 µJ energy and the frequency quadrupled pulses with pulse energy 1 µJ were focused onto the rotating target mounted on a high speed computer hard disk drive. The rotational target was chosen because at high repetition rate the laser radiation rapidly digs a deep crater in a sample. The fundamental pulse focused onto the target was able to ablate and ionize the material and as plasma was generated. An IR InGaAs photodiode was used to

record the fundamental pulse and it was displayed onto the oscilloscope. A vacuum Si photodiode with the cutoff wavelength at 1.1 μm was used to display the plasma generation on the oscilloscope. Figure 4.21 shows the oscilloscope trace of the fundamental pulse focused onto the target and the plasma generated.
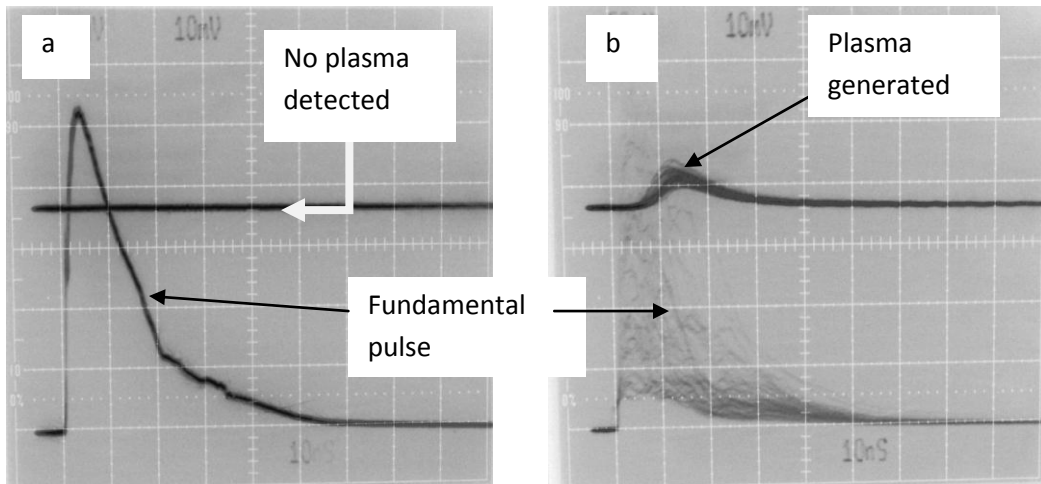
Figure 4.21 Oscilloscope trace of fundamental pulse with the energy of 46 μJ along with frequency doubled and quadrupled pulse focused onto the (a) non-moving target, (b) moving target. The horizontal scale is 10 ns/div. The traces are taken with a 1 GHz bandwidth oscilloscope.

In figure 4.21 the upper trace represents the plasma generation detected by the Si photodiode and the lower trace shows the incident fundamental pulse. In the case when the target was not moving, so there was no plasma generation detected as clear from figure 4.21 (a). After the target started moving we were able to see the ablation as it was very bright. As one can from the figure 4.21(b), that the scattered light from the fundamental pulse becomes unstable at this time because the target is moving. The other reason for this instability can be the undesirable

118

feedback from the target surface. The incident fundamental pulse is about 16 ns (FWHM).

For performing the dual pulse LIBS the frequency quadrupled pulse should be focused on the target after the plasma generation. The drawback of the present laser setup is this that it doesn't provide any provision so that we can introduce this time delay between the both laser pulses. Due to time limitations it was not possible to introduce a pulse separation and time delay scheme and thus we were not able to properly study the dual pulse LIBS with the current setup. However, as a first step the normal LIBS spectra were recorded for Iron (Fe) and Silver (Ag) using the fundamental pulse for the ablation. The single shot ablation spectra was recorded for the silver (Ag) and Iron (Fe) using the spectrometer and ICCD camera (Andor istar DH720). The gate width of the detector was kept at 1μs. The LIBS spectra are shown in figure 4.22 and 4.23 for Fe and Ag respectively. Only the fundamental laser pulse at an energy of 46 μJ was employed on the target in this case.
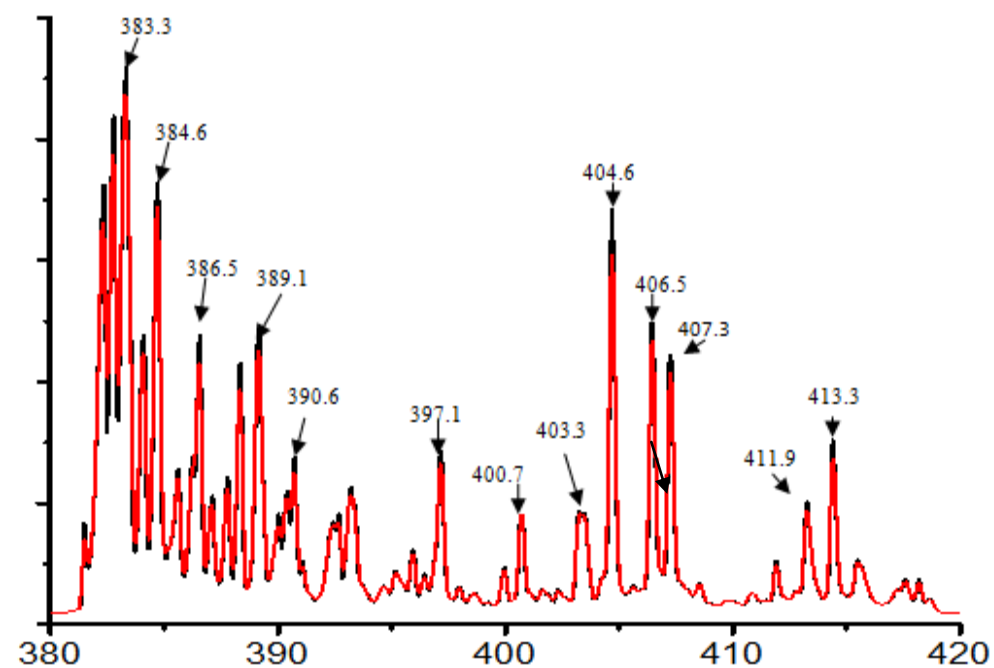
Figure 4.22 Single shot ablation spectra for Fe using 50 µJ 1545 nm pulses. The gate width of the detector was kept at 1 µs.
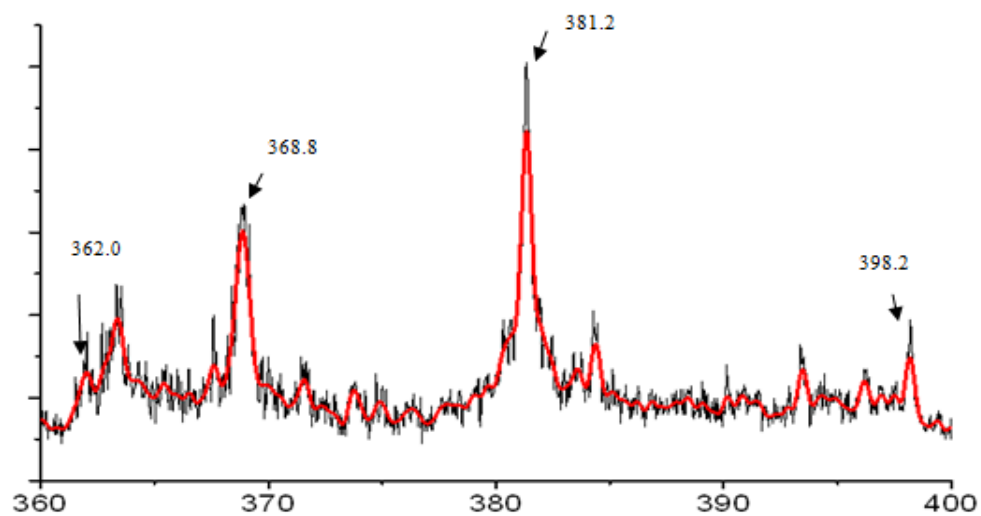
Figure 4.23 Single shot ablation spectra for Ag using 50 µJ 1545 nm pulses. The gate width of the detector was kept at 1µs.

The emission wavelengths obtained for Fe and Ag were compared with the emission wavelengths reported in literature and are summarized in Tables 4.1 and 4.2.

Position of strongest emission lines in present work (nm)	Emission wavelength in nm provided by National Institute of Standard and Technology [142]
414.4	414.38
413.3	413.20
411.9	411.85
407.3	407.17
406.5	406.35
404.6	404.58
403.3	403.26
400.7	400.72
397.1	397.13
390.6	390.64
389.1	389.33
388.3	388.43
386.5	386.55
385.6	385.63
384.6	384.68
383.3	383.42
382.2	382.18

Table 4.1 Emission wavelengths observed for Fe.

The emission wavelengths observed for Fe with the single shot laser pulse are in good agreement with the reported values in the literature within the ± 0.15 nm spectral calibration error.

Position of strongest emission lines in the present work (nm)	Emission wavelength of Ag(I) provided by National Institute of Standard and Technology (nm) [142]
362.0	362.46
368.8	368.25
381.2	381.09
398.2	398.15

Table 4.2 Emission wavelengths observed for Ag.

The emission wavelengths for Ag agree approximately with the expected values in Table 4.2. The first two values appear to deviate more than expected from the tabulated values and may indicate an inaccuracy in calibration of the spectrometer in the UV end of the spectrometer or contribution of emission lines from some trace elements in the silver. It can be seen that even single shot ablation gives enough emission to collect good spectra. The sensitivity can be greatly enhanced by multi shot accumulation. From the previous work on the application of LA-LIF [14,143] it is clear that atomic species will be formed as the plasma recombines and it should be possible to resonantly excite these species with the tunable UV probe pulse. In that work it was shown that signals could be obtained with fluorescent excitation pulse energies of the order of 1 to 10 μJ and thus it is

expected that the present fourth harmonic pulse energy of 1 µJ should be sufficient for resonant excitation of a fluorescent emission line.

4.6 Conclusions and Future Work

The aim of this dissertation was to develop and characterize a fiber laser system for a smart, portable and rugged LIBS and dual pulse LIBS fiber optic sensors. A multistage fiber amplifier system with a tunable DFB diode laser source was designed and characterized for this application. We were able to amplify the input laser pulse with pulse energy of 0.4 nJ to 4 µJ giving an gain of 40 ± 3 dB in the first stage double pass amplifier. The second stage of amplification was carried out with the help of double clad large node area polarization maintain (LMA-PM) Er/Yb doped fiber. The output energy of 46 µJ was obtained after the second stage amplification giving an overall gain of 51 dB. The first and second stages of the amplification were characterized by studying various parameters under different operating conditions. The amplified laser pulse was further focused onto a 10 mm long PPLN crystal for frequency up-conversion and then was further up converted with the help of a BBO crystal. When optimized we were able to achieve pulse energies of about 46 ± 5 µJ for the fundamental pulse (1545 nm), 15 ± 3 µJ frequency doubled (771.44 nm) and 1 ± 0.2 µJ frequency quadrupled (385.62 nm). Due to the narrow line width the fiber laser system that has been developed is subject to the onset of SBS instabilities. The details of SBS pulse manifestation with repetition rate, pulse width and other parameters has been investigated and it

has been found that the SBS pulse could be suppressed using high repetition rate ($\geq$ 10 KHz) and short seed pulse excitation ($\leq$ 60 ns). The developed laser system has small foot prints which make it potentially portable and relatively low cost. In addition, with operation at 1545 nm the fundamental wavelength is essentially eye safe.

CHAPTER 5

APPLICATION OF OPTICAL LOW COHERENCE REFLECTOMETRY (OLCR) TO HYDROCARBON SENSING IN HIGH PRESSURE CELLS

5.1 Motivation

In the oil industry, the characterization of crude oil is a key factor for optimization of the extraction and refining process. The natural gas and petroleum industries increasingly demand accurate high pressure phase equilibrium data of petroleum fluids from new oil deposits under development. But the detection of composition and phase transition can be challenging because of the high temperature (up to 250 C) and high pressure (30,000 psi). Some applications that exhibit challenges requiring improvements to the existing equipments are lean gas condensate fluids, where the amount of liquid dropout is minimal and the standard equipment does not allow accurate quantification of the accumulated liquid. Phase boundary detection in crude oil is another point of interest which is discussed in this project work. Phase separation can occur when the pressure (or temperature) causes gas or solids to precipitate when the thermodynamic conditions necessary for solution equilibrium are crossed. Due to the viscous nature of the heavy oil, though the separation has occurred, coalescence of the gas phase does not occur easily or quickly. Thus accurate determinations of the bubble point pressure and subsequent accumulation of gas phase/ liquid phase for volumetric measurements is difficult and sensitive to the test operator experience and skills. The main objective of this work is the development of an initial prototype fiber sensor for

detection of a number of the parameters already described above. Fiber optic sensors are widely investigating because they have several advantages over conventional sensors such as an immunity to electromagnetic interference, ability to operate in a wide range of environments, high sensitivity and the potential for multiplexing [144]. Most of the physical properties of various crude oils can be obtained from literature or are readily measured using established laboratory methods [145,146]. For example the refractive index (RI) measurements are of great interest in different fields of the industry for chemical analysis as well as for phase behavior. Most of the instruments used for the refractive index measurements are based in the accurate determination of the critical angle for the total internal reflection. Different systems have been developed to measure RI for various samples and variations of the Abbe refractometer have been widely used [147,148]. Implementation of total internal reflection and prism coupling are frequently used but the experimental sets up are complex and sensitive to external perturbation [149,150]. Several authors have proposed an intrinsic optical fiber sensor for the phase boundaries detection of the hydrocarbons. Rogerio et al [151] proposed a technique for the separation of oil, water and gas based on the reflectivity measurements from an angle cleaved fiber tip. Weize Wu et al [152] also measured the reflectivity signal based on the difference in refractive index between fiber and fluid and hence change in density. Avdeev et al [153] proposed a fiber optic reflectometer to monitor refractive index and density changes in gases, liquids and fluids. Most of the techniques are based on the reflectivity

measurements from the fiber tip and for this the fiber should be inserted into the solution.

A fiber sensor working on the principle of optical low coherence reflectometry (OLCR) for measuring phase boundaries and parameters (e.g. refractive index, physical thickness etc) for use in real industrial conditions has been build in the present work.   The fiber sensor developed has shown high accuracy in determining the amount of liquid (gas condensate) at the bottom of an industrial the high pressure test cell. In addition, the method used in the setup also has the capability of determining some optical parameters of the contents such as refractive index and optical uniformity (phase boundaries). The sensor to be inserted into the test cell has a small size (~3 mm in diameter) and can be introduced into the high pressure cells through the standard pressure fittings used in the oil industries.

5.2 Experimental Methodologies

The experimental system developed and described in this section is based on the basic principles of OLCR. The experimental setup developed demonstrated high accuracy in determining the amount of liquid (gas condensate) at the bottom of the high pressure test cell. In addition to the technique has the capability to determine some optical parameters of the contents. In doing so, it was necessary to alter some of the aspects of the conventional OLCR in order to optimize its use for this sensing technique.

5.2.1 Overview

Figure 5.1 shows the experimental set up for performing the Optical Low coherence Reflectometry. The Michelson interferometer arrangement, used as the basis for all OLCR setups, is evident from the diagram, as shown with four fiber arms (source, test, reference, and Receiver). The individual components utilized in each respective arm will be described in the separate four sections.

The amplified spontaneous emission output of an EDFA at 1550 nm was utilized as low the coherence light source for performing OLCR technique. The output from the low coherence source was split into two parts using a four port fiber coupler (FC1) which divides the low coherence beam into two parts with a ratio of 98:2. The 98% part was used as the source beam and the 2% part was used as the reference beam. The source beam fiber end was further spliced to port 1 of a 1550 nm 3-port circulator which is named as 'Circulator 1'. The circulator routes the incoming signals from port 1 to port 2 and incoming port 2 signals to port3. The port 2 of 'Circulator 1' was spliced to fiber pigtailed 'Grin lens 1'. The 'Grin lens 1' was used as the Test Arm. The Grin lens is a 1550 nm single mode fiber collimator (OEQuest). This collimator was used to launch the light into the target sample and then to receive back the reflected signal. The collimator has the dimensions of 12 mm (L) x2.4 mm (ϕ). The port 3 of 'Circulator 1' was spliced to another fiber coupler FC2 with ratio of 60:40. The reference beam was further spliced to one port of another 1550 nm 3-port circulator called 'Circulator 2'. The

port 2 of 'Circulator 2' was further spliced to another 1550 nm single mode fiber collimator named as 'Grin lens 2'. This arm is named as the Reference Arm. The port 3 of Circulator 2 was combined with the measurement signal in to the beam splitter FC2 (60:40). The output of the FC2 was used for recording and analyzing the signal and was spliced to a photodiode which was further connected to a digital oscilloscope for recording the signal which is named as the Receiver Arm. All the splicing has been done with the help of Fiberlign QFS-1001 fusion fiber splicer and heat shrinking protection sleeves were used to protect the splices. The different arms were connected with each other with the help of standard optical fiber connectors.
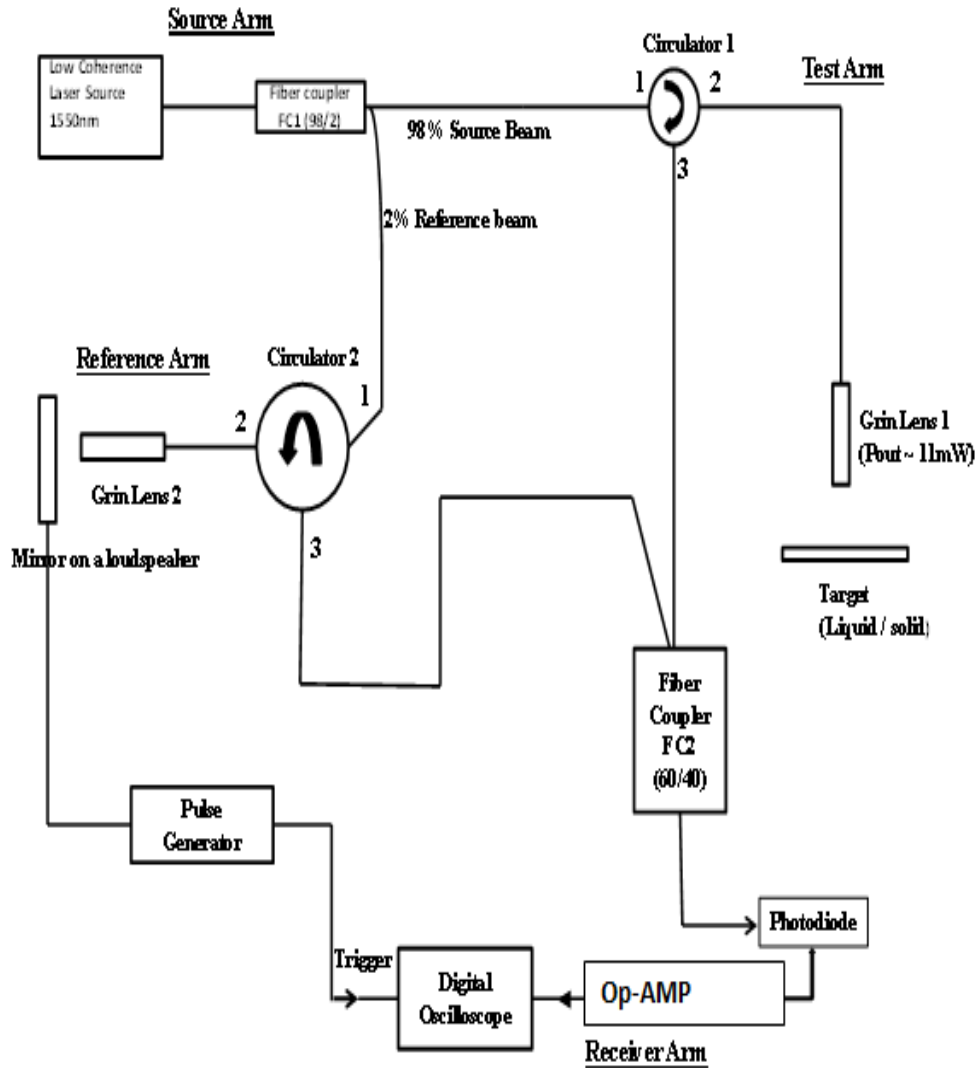
Figure 5.1 Experimental Set Up

5.2.2 Source Arm

The low-coherence light source for the system is provided by the commonly-utilized amplified spontaneous emission (ASE) from an EDFA. This light source was obtained using the schematic shown in figure 5.2. The fiber pigtailed 1480 nm pump laser diode (Fitel- FOL1404QQO) was used as the pump laser diode.

An external current driver and temperature controller were used for the pump laser diode. The 1480 nm pump laser diode was spliced to 10 m of single mode erbium doped fiber through a WDM. To avoid feedback and possible lasing which could result in long coherence length, an isolator was spliced on the other side of Er-fiber. An ASE signal with output power of about 13 mW was obtained from both ends with 55 mW pump power. This was then used as a low coherence source for the further work.
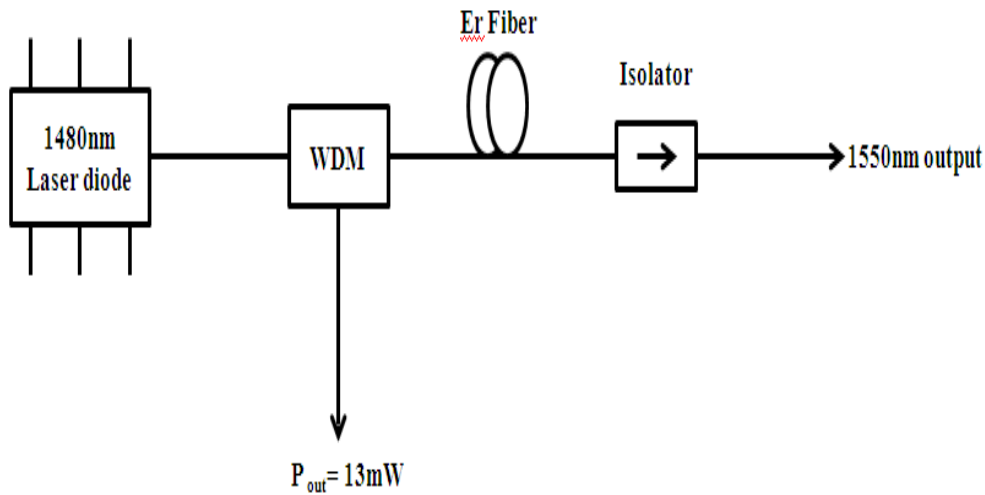
Figure 5.2 Low Coherence laser source

5.2.3 Reference Arm

The simplest way to implement a delay line is to have a movable mirror in the reference arm. For the reference channel a mirror was glued onto a loudspeaker as shown in figure 5.3. The output of the loudspeaker was connected to a function generator, which would cause the loud speaker to oscillate. The frequency and the

voltage of the function generator were optimized to get a large signal. The loudspeaker was driven at its resonant frequency which was found to be 73 Hz and the drive voltage was set at 100 mV$_{PP}$.
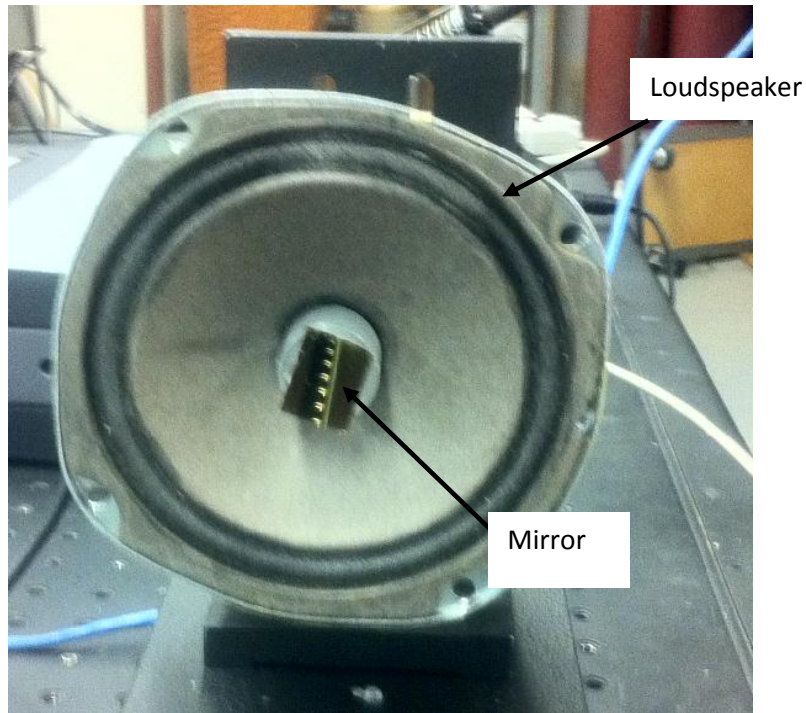
Figure 5.3 Mirror glued on the loudspeaker.

The reference grin lens was placed on an automatic translational stage as shown in figure 5.4. The translational stage used was a Thorlabs LTS300 long travel stage which can scan up to 300 mm distance.
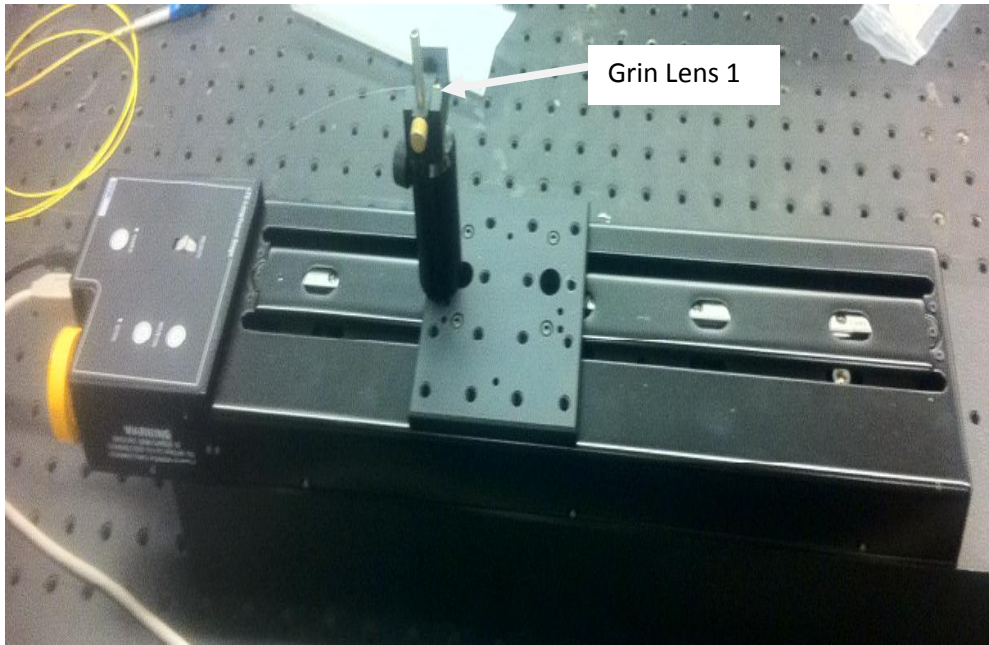
Figure 5.4 Reference Grin lens on a translational stage

5.2.4 Test Arm

The Grin lens 1 was used as the Test arm grin lens and it was used to scan various target samples. Different arrangements were used for different targets. The Grin lens was placed in a fiber holder for solid target tests as shown in figure 5.5.
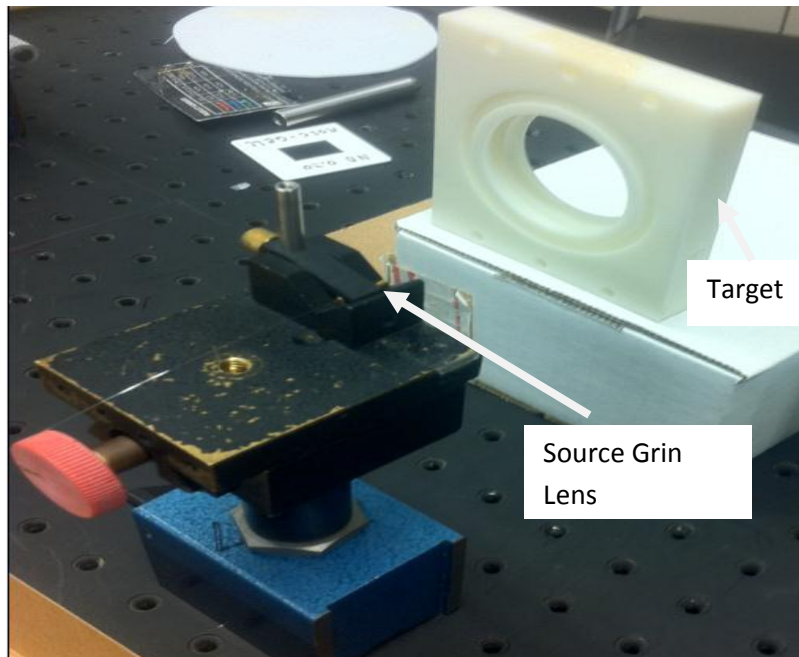
Figure 5.5 Test Grin lens placed in front of a test target sample.

Tests experiments were performed using various targets (solid and liquid). Foam polyethylene was used as a solid target to represent non uniform medium with phase boundaries. In the case of foam polyethylene multiple interference maxima that corresponded to the boundaries of the foam cells could be observed. For scanning liquids a measuring head was made using aluminum as shown in figure 5.6. Grin lens was inserted from one end and a glass filter was glued using high temperature epoxy to attenuate the signal.
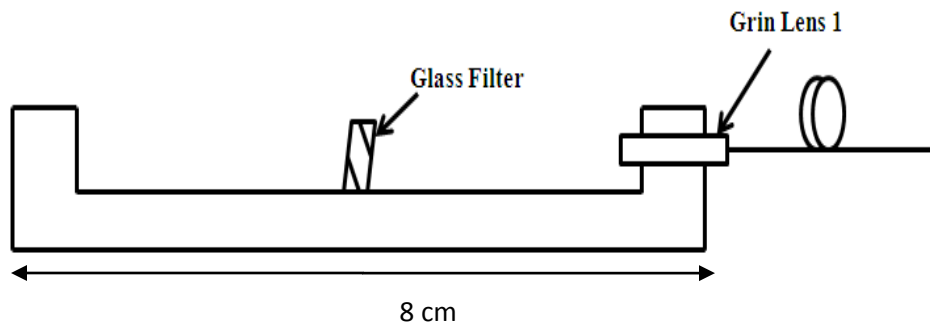
Figure 5.6 Measuring head

The measuring head was partially placed inside a measuring container as shown in figure 5.7 and the interference pattern was recorded for different liquids.
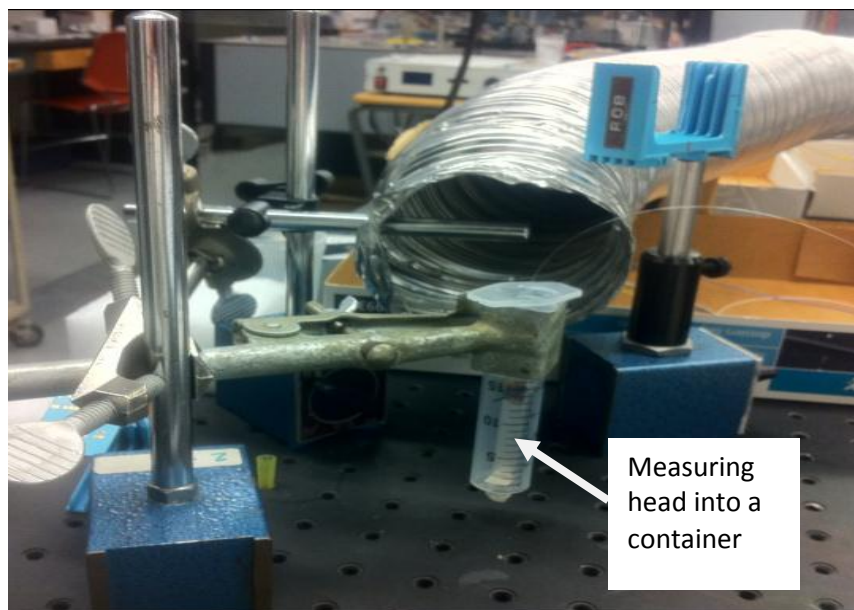
Figure 5.7 Measuring head into the measuring cylinder

With the help of the above measuring head it was not possible to measure large amounts of liquid so another glass cylinder was used as the measuring cylinder that allowed monitoring the test conditions visually and is shown in figure 5.8. To test the ability of the system to detect and measure a small liquid layer at the

bottom of the glass cylinder three different liquids were used: hexane, chloroform and crude oil (the crude oil was diluted 4 times with chloroform). During the test, first the position of the interference maxima for the empty cylinder was determined. Then the test liquid (hexane and chloroform) was added in small amounts and the corresponding change in the position where the maximum interference signal is observed has been recorded. Examples of the sinusidally modulated interference signal observed when the reference arm is adjusted close to the maximum interference signal distance are shown in figures 5.9 and 5.10.

Grin lens in fitted in a metal rod
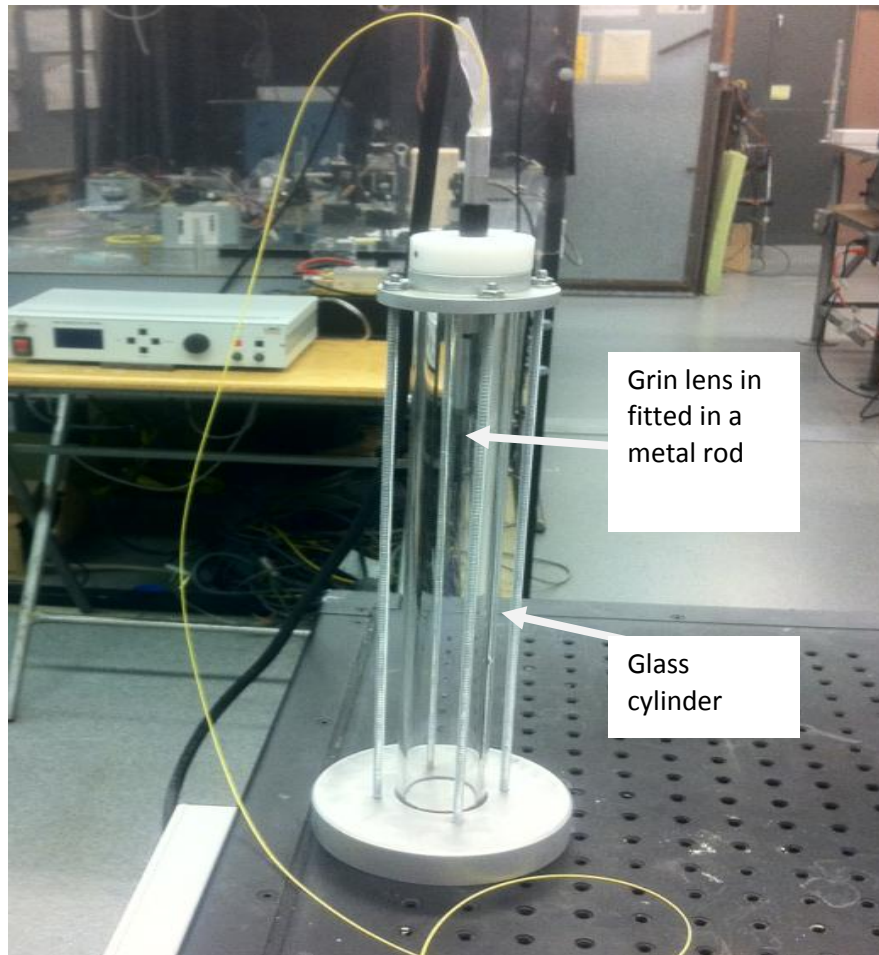
Glass cylinder

Figure 5.8 Glass Cylinder with source Grin lens
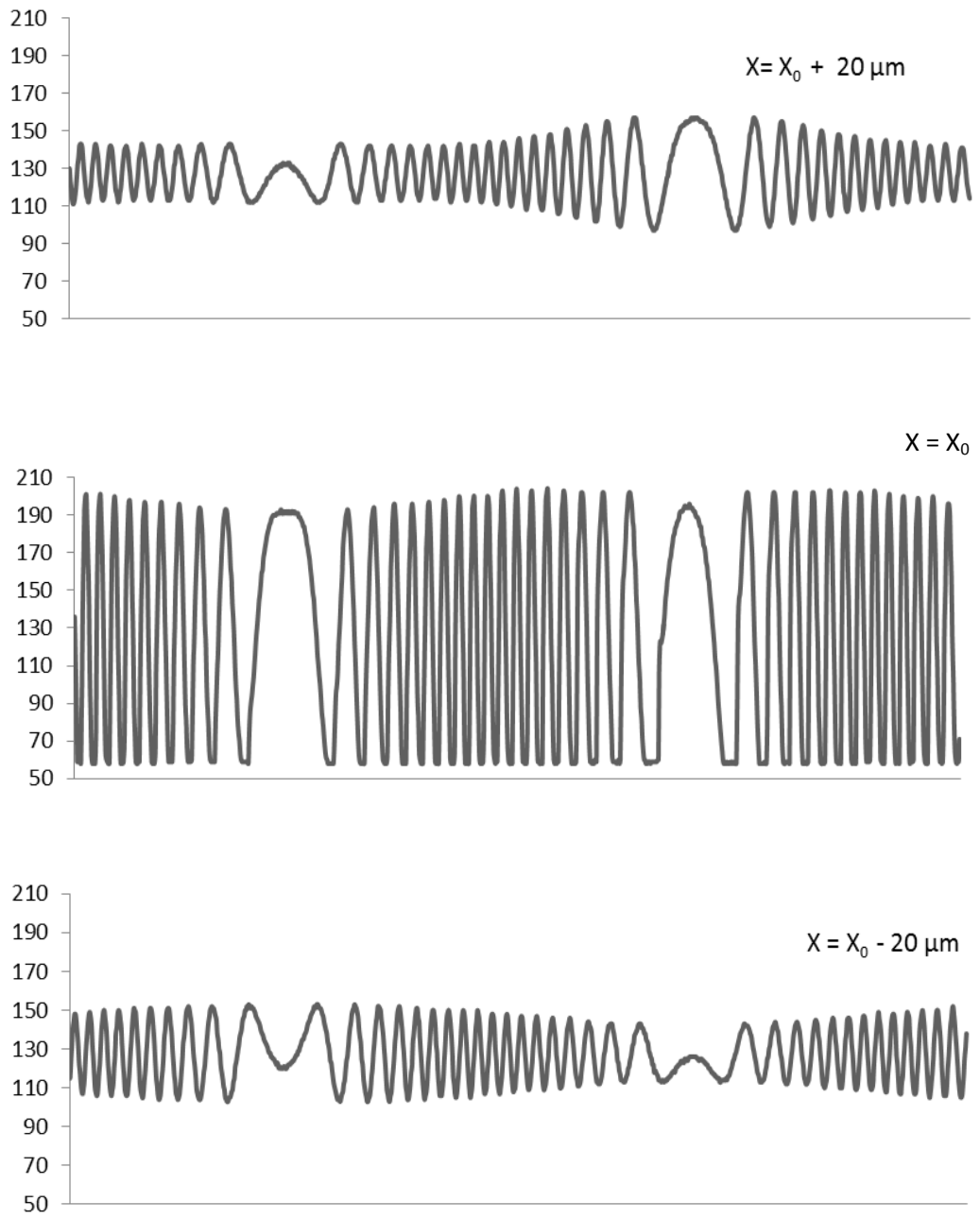
Figure 5.9 Interference signal in the empty glass cylinder with the maximum interference signal at $X_0 = 107.24$ mm and two other positions at a distance of 20 μm from the maximum.
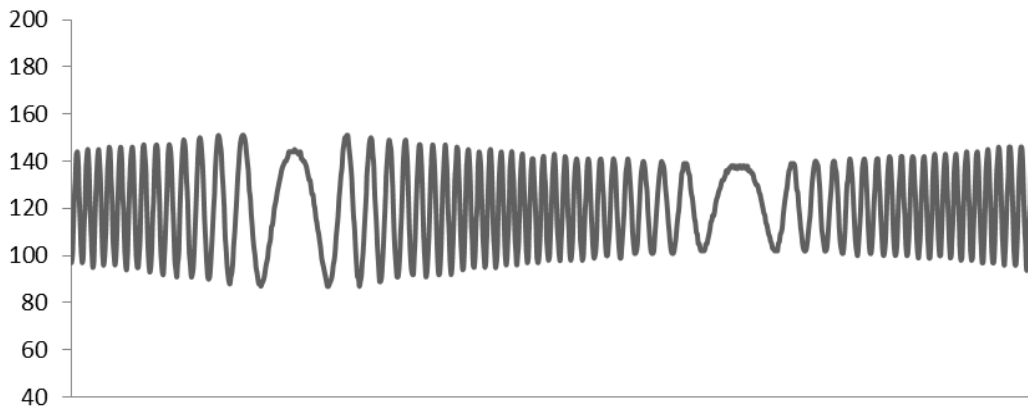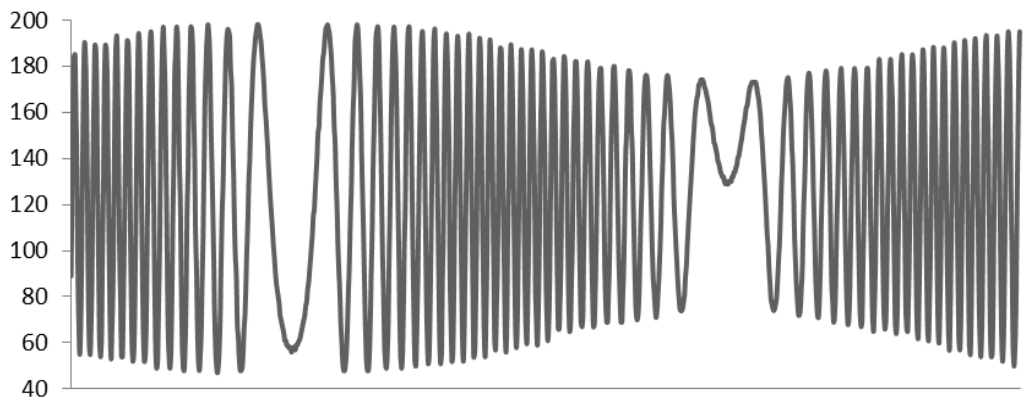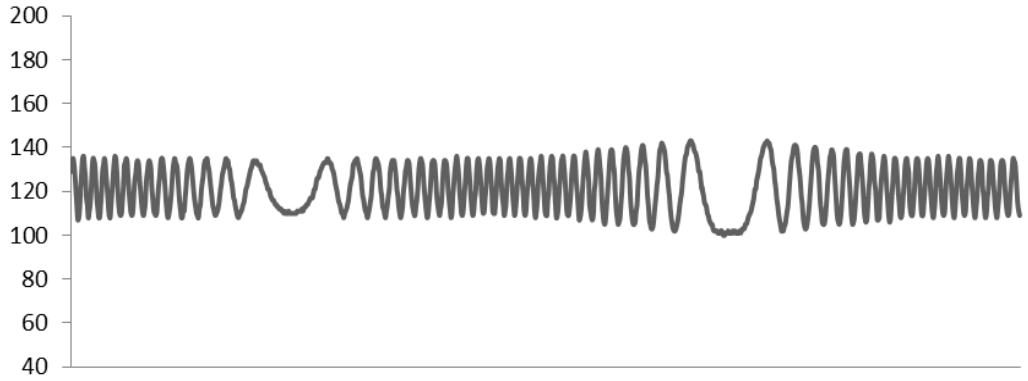
Figure 5.10 Interference signal in the hexane in the glass cylinder with the maximum interference signal at $X_0 = 106.00$ mm and two other positions at a distance of 20 μm from the maximum.

It was observed that after adding the liquid into the cylinder we obtained two maxima. The strength of one maximum was strong in comparison of other maxima. The strong peak was due to the light back reflected from the bottom surface of the cell and the weak peak from the light reflected from the bottom of the cell which was reflected back downwards from the top surface of the liquid and scattered again from the bottom of the cell. This will be discussed in detail later in the chapter. Then the same tests were performed in a high pressure steel test cell received from Weatherford Industry [154] which is shown in figure 5.11.

Figure 5.11 High pressure cell

The high pressure cell is an actual test cell used in the oil industry for determining phase boundaries and other conditions. For the high pressure cell a separate source test arm was made with the help of high temperature epoxy and metal fiber jacket so that the fiber pigtailed grin lens was robust enough to handle high pressure and high temperature under the real industrial test conditions.

5.2.5 Receiver Arm

The final part of the detector is the receiver arm where the reflected signals from the test and reference arm recombine and mix to create the desired interference signal. For the receiver arm a fiber pigtailed PIN InGaAS photodiode was used in connection with an Op-AMP amplifier circuit with the schematic as shown in figure 5.12.
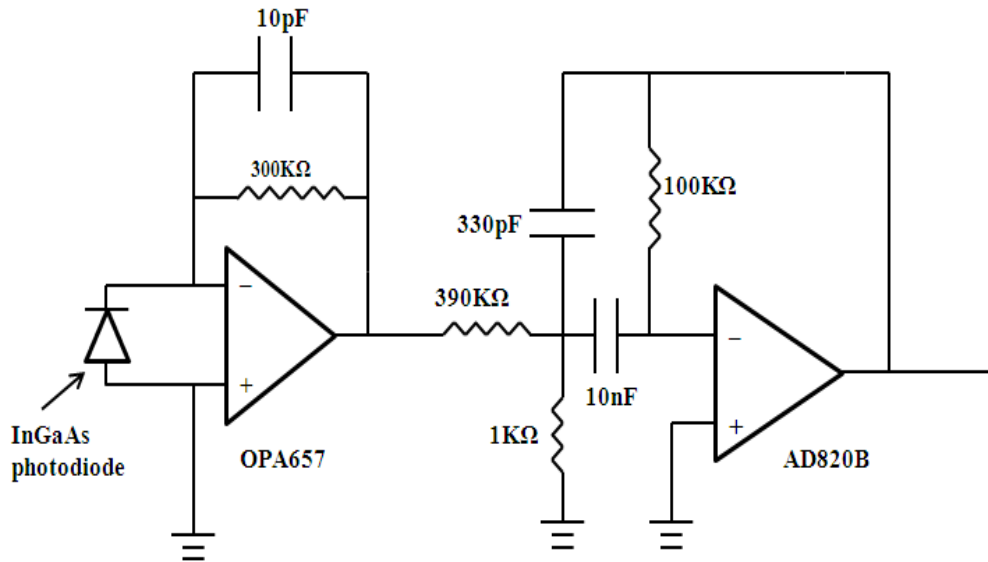
Figure 5.12 Recevier arm amplifier circuit

The first Op-Amp (OPA657) is a broadband transimpedance amplifier and the other Op-Amp (AD820B) works as a band pass amplifier with 3 dB band width of 5 KHz. The electrical signal acquisition from the receiver arm is provided by a data acquisition card interfaced with a personal computer. The signal output of each photodiode receiver board was sent to a National Instruments PC data-acquisition card, where they underwent an analog-to digital (A/D) conversion for processing by the PC. Within the PC, further signal processing is provided using LabVIEW Version 6 graphical programming software, from National Instruments. Additionally, this software supplies the tools needed to construct a graphical interface to display the experimental results.

5.2.6 Physical Assembly

This section will provide a comprehensive guide with respect to the operation of the previously described components as an entire system. A photograph of the assembled devices and enclosure that make up the experimental OLCR project system are shown in Figure 5.13. The power supplies shown are required for the operation of 1480 nm pump laser diode and for the receiver arm (photodiode with OP-AMP circuit). A separate power supply was used for controlling the temperature of the pump laser diode. The source arm, reference arm and the receiver arm were connected to the other fiber components (e.g. circulators, fiber coupler etc) with the help of connectors. All the fiber components were either fusion spliced or connected together to make the circuit more robust and compact.
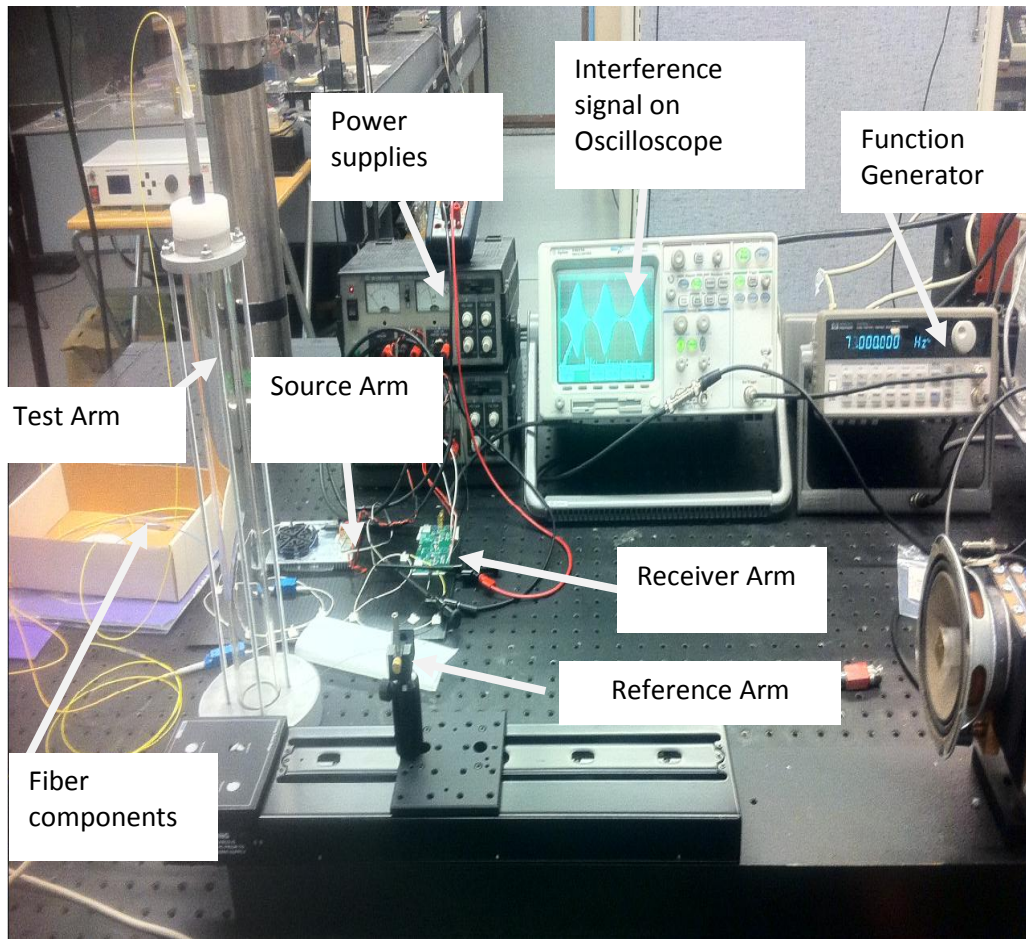
Figure 5.13 Experimental OLCR System

5.3 Thickness and refractive index measurements

With the OLCR setup various solid and liquid targets were tested by putting them in front of the test arm and scanning the reference arm to locate the maximum interference signal. Foam polyethylene was used as a solid target to represent a non-uniform medium with phase boundaries. In the case of foam polyethylene multiple interference maxima that corresponded to the boundaries of the foam cells could be observed. In the case of liquids simultaneous measurements of

physical thickness and refractive index were carried out. For these studies three liquids i.e. Hexane, Chloroform and diluted crude oil were used. These measurements were first done in the visible glass cylinder and then in a high pressure cell. During these measurements first the position of the interference maxima for the empty cylinder was determined and then with the addition of liquid the corresponding change in the maximum interference signal was recorded. Two maxima were observed after adding the liquid into the cylinder and one maximum is found stronger in comparison of other maxima as illustrated in figure 5.14. As shown in figure 5.15 the first strong maximum is the reflection from the bottom of the liquid in the cylinder. The second weak maximum is the double reflection from the bottom surface of the cell of light reflected from the bottom of the liquid layer. In case of clear liquid no reflection was observed reflected directly from the top surface of the liquid since the alignment was not adjusted perfectly perpendicular to this layer.
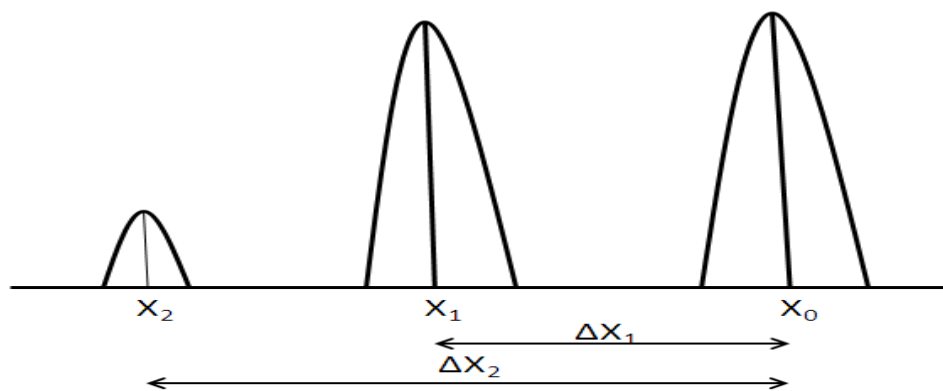
Figure: 5.14. Interference pattern observed after adding liquid into glass cylinder. X_0 is the position of interference maximum without any liquid in the cylinder; X_1 is the position of maximum when liquid was added and X_2 is the position of second maximum.

144
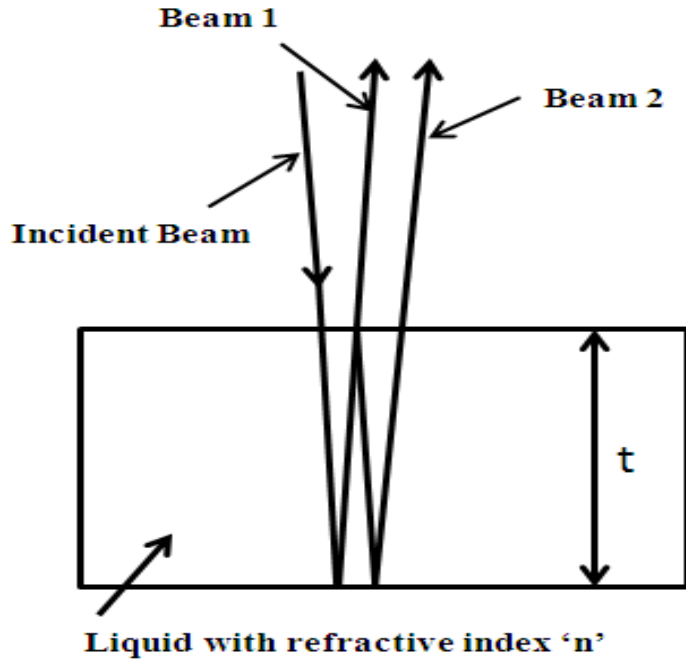
Figure 5.15 Reflection from the bottom of the liquid with refractive index n and thickness t; Beam 1 is the scattered beam from the surface at the bottom of the liquid; Beam 2 is the doubly scattered beam from the bottom of the top surface of the liquid.

Referring to figure 5.15 the extra optical path traveled by beam 1 is given as

$$\Delta X_1 = t.n- t \qquad\qquad (5.1)$$

And for beam 2 it is given as

$$\Delta X_2 = 2t.n-t \qquad\qquad (5.2)$$

Where 't' is the thickness and 'n' is the refractive index of the liquid. ΔX_1 and ΔX_2 are the total extra path lengths. So from the equations 5.1 and 5.2 we have two unknown parameters n and t and by solving these two equations algebraically we get the refractive index and the thickness of the liquid samples as given below:

145

$$t = \Delta X_2 - 2\, \Delta X_1 \tag{5.3}$$

$$n = \frac{\Delta X_2 - \Delta X_1}{\Delta X_2 - 2\Delta X_1} = = 1 + \frac{\Delta X_1}{\Delta X_2 - 2\Delta X_1} \tag{5.4}$$

 With the help of these equations measurements of the liquid parameters in the glass cylinder and the blind test cell were carried out. Due to the physical construction of the glass cylinder and the blind test cell they have some meniscus on the liquid layer and some extra liquid is needed to fill in small gaps in the bottom surface before getting the correct results. The amount of this extra liquid is called blind volume and it was also calculated in this work. The test experiments were performed with different liquids and the thickness and refractive index were calculated for these liquids as explained in the following sections.

5.3.1 Estimation of the longitudinal resolution

The longitudinal resolution depends on the coherence length of the light source. To estimate the accuracy of the peak position determination the test grin lens was placed on the top of the empty glass cylinder and the optical path lengths between both arms was made equal and the corresponding interference maximum is shown in figure 5.16. For the estimation of accuracy the test grin lens was placed on the top of the empty measuring cylinder and the reference arm was scanned to record the interference signal. The variation between distances moved by reference arm with the interference signal strength on the oscilloscope is shown in figure 5.16.

The variation of the interference signal strength versus distance moved by reference arm as observed on the oscilloscope is shown in figure 5.16.
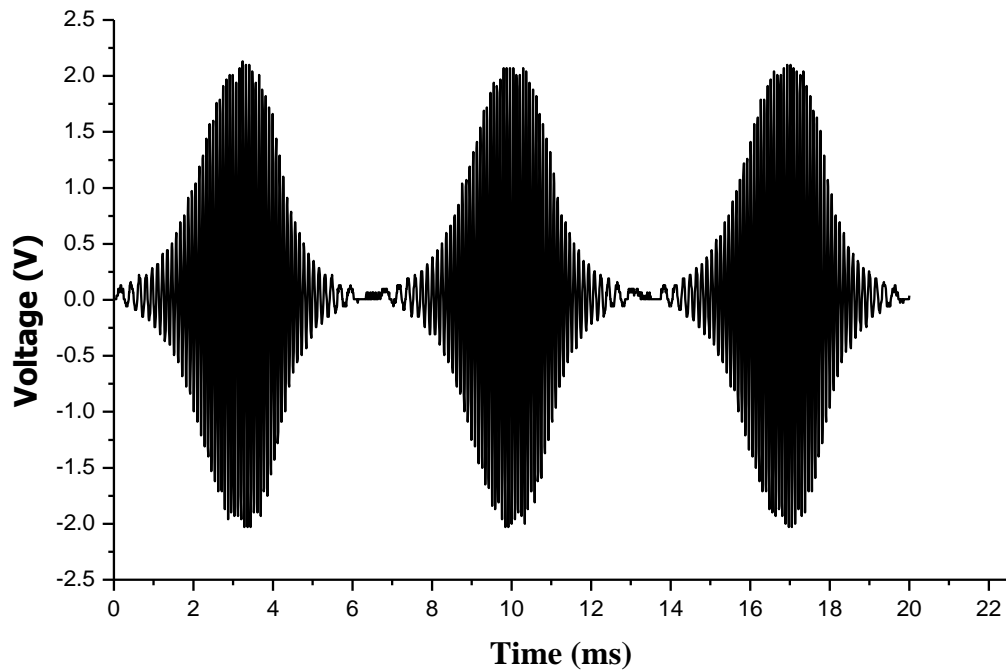
Figure 5.16 Interference pattern for the empty glass cylinder. Each peak corresponds to one transit of the loudspeaker surface.
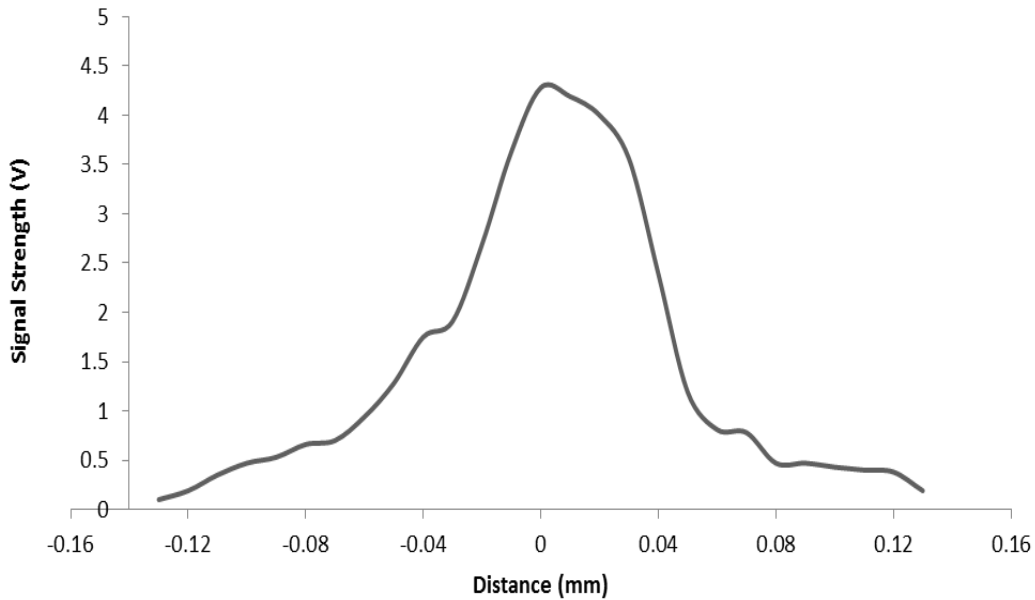
Figure 5.17 Signal strength versus reference arm position

The longitudinal peak signal width was estimated to be approximately 80 μm from the results shown in figure 5.17. However the centroid of the peak could be located to about one quarter of this width giving a measurement resolution of approximately ± 20 μm.

5.3.2 Hexane in the glass cylinder

The first test experiment was performed with hexane in the glass cylinder and the theoretical height for hexane in glass cylinder, h', was calculated using the expression given below:

$$h' = \frac{Volume\ of\ hexane\ in\ cylinder}{\pi r^2} \qquad (5.5)$$

Where r is the internal radius of the glass cylinder which was measured to be about 18 ± 0.5 mm.

The coherence length of the laser source was estimated to be about 30 µm from the longitudinal interference pattern. This coherence length corresponds to the spectral width of about 40 nm. The Grin lens 1 (Test arm) was placed in a metal rod and was placed on the top of glass cylinder and then the reference arm was scanned to get the maximum interference signal on the oscilloscope. The maximum interference signal strength was determined by the peak to peak voltage on the oscilloscope. The position of the reference grin lens was adjusted manually so as to get the maximum peak to peak value of the signal on the oscilloscope. The position of the reference grin lens on the translational stage was then recorded for each of the two reflected signals for each volume of the liquid added. Then the hexane was added in small amounts into the glass cylinder and the reference arm was again scanned for the maximum interference signal (peak to peak voltage). The position of the maximum interference signal was found to be moved from the initial position and the corresponding change in position was recorded. Also with the addition of Hexane a second maximum interference signal was observed. The maximum interference signal the oscilloscope Figure 5.18 shows variation of position of first and second maxima for the hexane in the glass cylinder with the amount of hexane added into the glass cylinder.
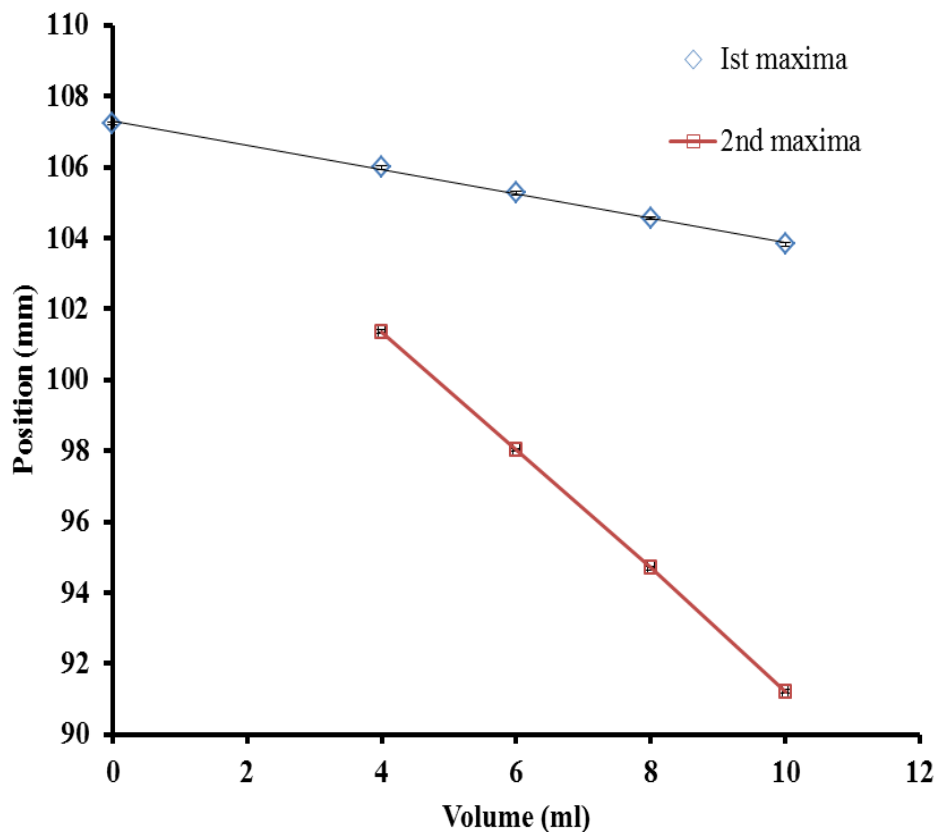
Figure 5.18 Variation of the first and second maxima with the volume of hexane added in the glass cylinder.

The refractive index and the thickness of the hexane were calculated using the position of first and second maxima from the values plotted in figure 5.18 using the equations 5.3 and 5.4 and are shown in figure 5.19 and 5.20 respectively. The calculated thickness and the theoretical height from equation 5.5 were found in good agreement as shown in figure 5.20.
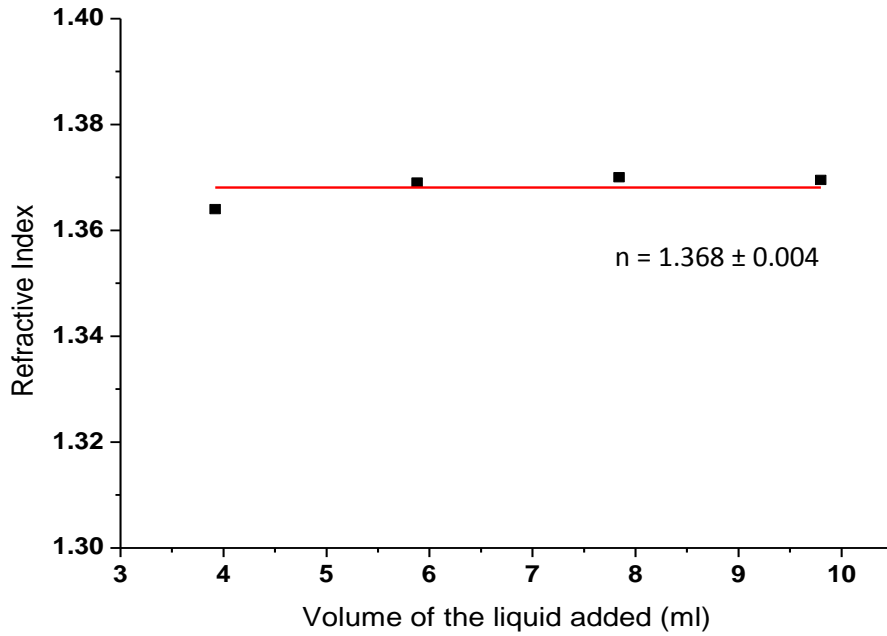
Figure 5.19: Refractive index versus Volume of the liquid added
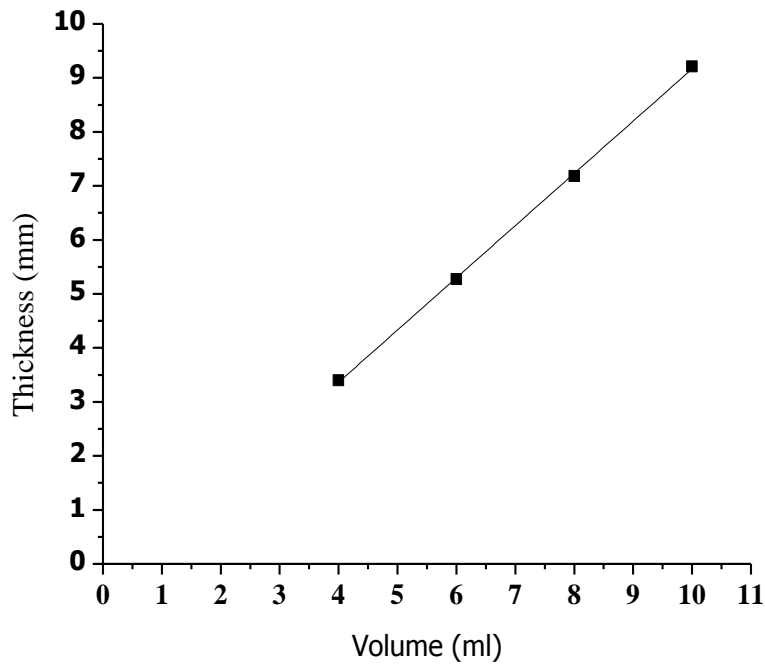
Figure 5.20: Physical thickness versus volume of the liquid added.

The experimentally calculated refractive index of the hexane 1.368 ± 0.004 is in approximate agreement with the known value already reported in literature of 1.365 at 1550 nm. The physical thickness of the sample (hexane) has a linear relationship with the volume of the liquid added as shown in figure 5.20. From this figure it is also possible to determine the blind volume in the glass cylinder which is 0.50 ± 0.09 ml. This blind volume is due to the physical shape of the cylinder as it has some negative meniscus at the bottom and some amount of fluid is needed just to fill any gaps in the bottom surface. The slope of the measurements gives a factor of 0.97 ± 0.02 mm per ml for the test cell. The error in the measurements of thickness is about 20 μm which is within the coherence length of our laser source. With this technique the refractive index of any unknown sample can be determined.

5.3.3 Hexane in the high pressure blind cell

To calibrate the big high pressure cell the same test was carried out by adding hexane in small amounts into it and by observing the change in position of interference maxima. Again the two maxima were observed after adding the hexane in the cylinder and the results obtained are shown in Figures 5.21 to 5.23 as shown below:
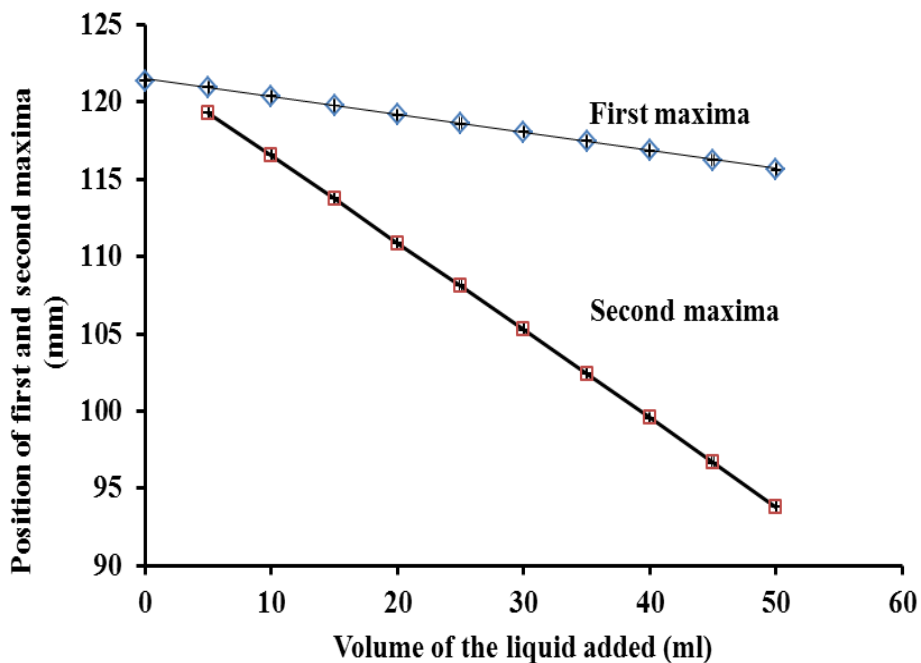
Figure 5.21 Variation of the first and second maxima with the volume of hexane added.
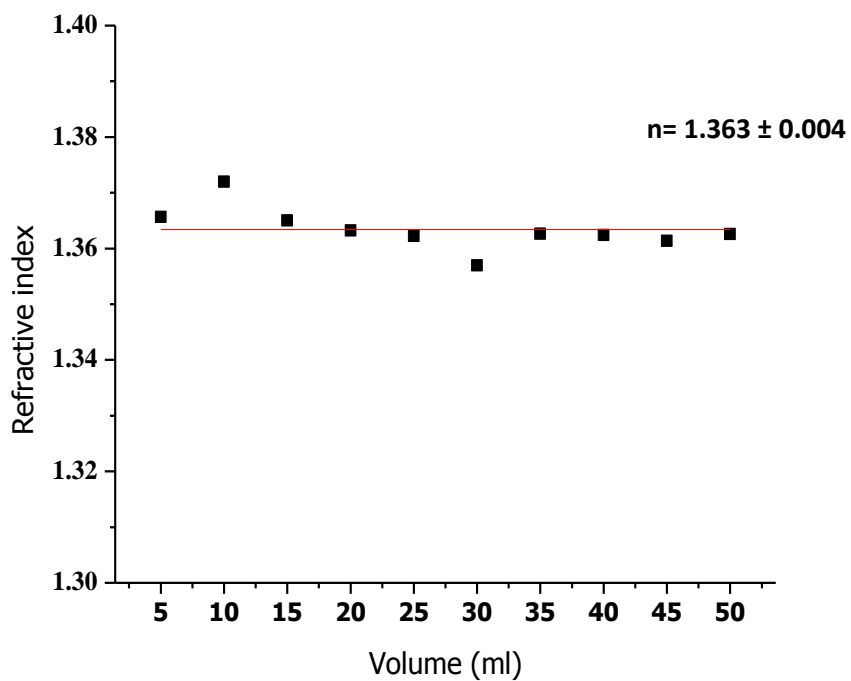
Figure 5.22: Refractive index vs Volume of the liquid added
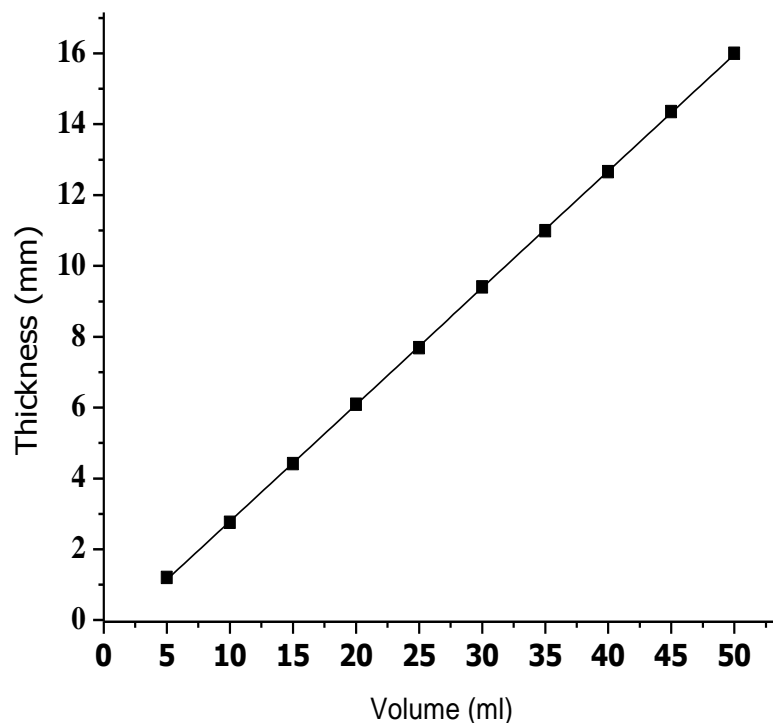
Figure 5.23: Physical thickness versus Volume of the liquid added

Figure 5.21 shows the variation of change in the position of first and second maxima while adding the hexane in the big cell. The variation of refractive index with the volume of hexane added is shown in figure 5.22. The experimentally measured refractive index value is 1.363 ± 0.004 which is slightly lower than the literature value of 1.365 and is consistent with the value which was observed with the glass cylinder. Figure 5.23 shows the variation of physical thickness of the liquid in the big cell with respect to the volume of the hexane added and the amount of blind volume was determined from the figure 5.23. The blind volume

in this case was 1.61 ± 0.09 ml. The slope of the measurement gives a factor of 0.32 ± 0.008 mm per ml for the test cell. Again the error in the measurement is of the order of 8 µm which is within the coherence length of the laser source.

5.3.4 Chloroform in the high pressure blind cell

The same experiment was repeated with chloroform in the blind steel cell and the thickness of the liquid and the refractive index were calculated using the equations 5.3 and 5.5 and the results obtained are shown in figures 5.24 and 5.25.
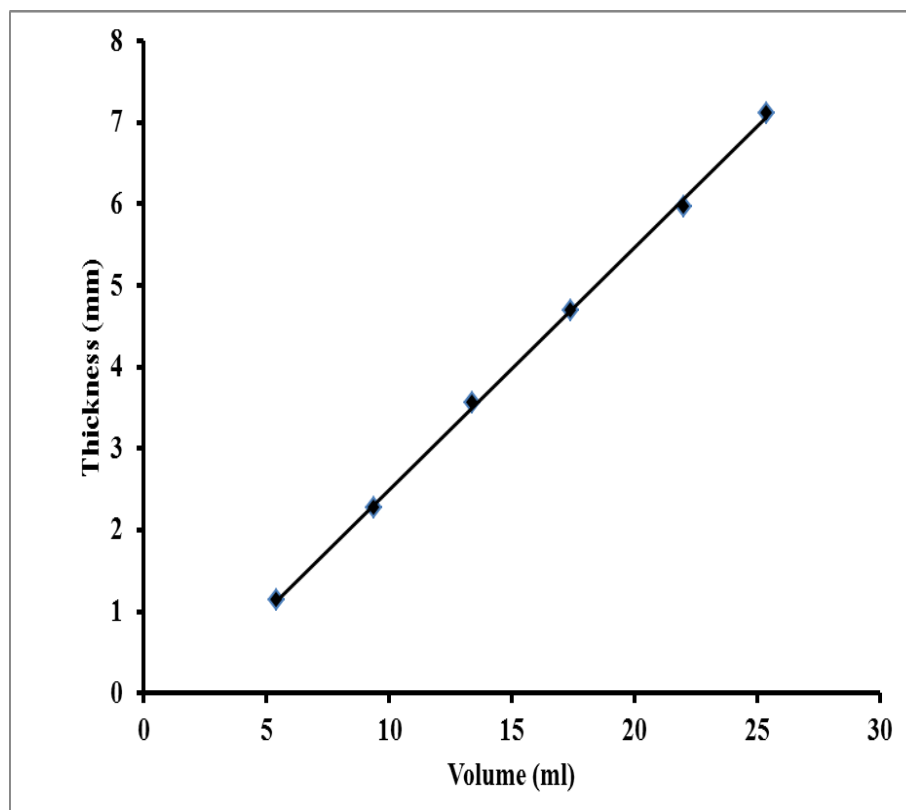
Figure 5.24 Physical thickness versus Volume of the chloroform added

Figure 5.24 shows the variation in measured thickness versus volume added. Again a blind volume of 1.59 ± 0.06 ml is measured for the blind cell. The scaling of volume with thickness is given by the slope of 0.30 ± 0.008 mm/ml. This compares reasonably with the coefficient of 0.32 ± 0.008 mm/ml measured for hexane presented earlier. Figure 5.25 shows the variation of refractive index with the volume of the chloroform added into the blind cell and the refractive index is found about 1.437 ± 0.004 which is in good agreement with the values of the refractive index already reported into the literature of 1.4366.
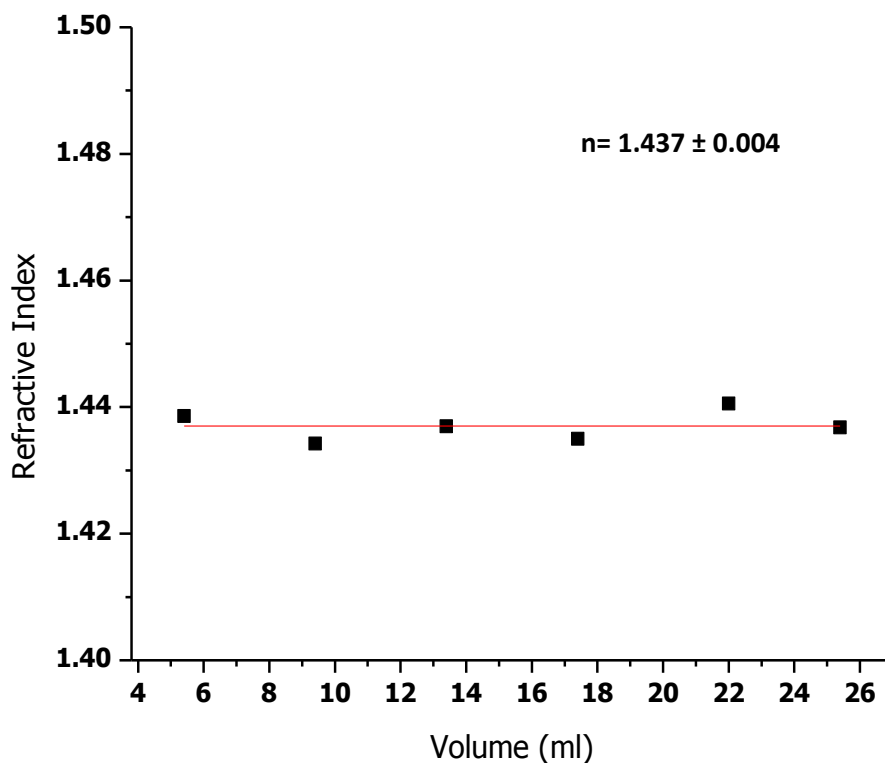
Figure 5.25 Refractive index vs Volume of the chloroform added

5.4 Testing at Weatherford Laboratories

One of the features of the measurement technique is that the sensor that has to be inserted into the test cell has a small size (~3 mm in diameter) and can be introduced into most of the high pressure cells through the standard pressure fitting. This sensor was tested in a real high pressure cell obtained from the Weatherford Laboratories, Calgary. For fitting into this high pressure and high temperature cell the test arm was modified and high temperature epoxy was used for fixing the sensor inside one of the gas filling tubes. It was also demonstrated that several fibers can be fed through this fitting tube and they remain in place even at high pressure. For this, a high pressure test was performed after gluing the three fibers into the small filling tube. The cylinder pressure was increased up to 15,000 psi without any failure of the fiber. It was found determined that with these fibers it is possible to work at high pressure.

5.5. Conclusions and future work

The main objective of the present work was to develop a fiber sensor which can be used in determination of the some important parameters (refractive index, thickness and the phase boundaries conditions etc) useful in the measurement of phase transitions in hydrocarbons at high temperature and pressures of interest to the oil industries. The fiber sensor developed here is based on the principle of Optical Low Coherence Reflectometry (OLCR). For the development of the fiber

sensor all standard fiber components such as fiber couplers, circulators, connectors, single mode fibers and collimators were used. These components are inexpensive and can be easily obtained which makes the system relatively cheap and robust. The developed fiber sensor was tested in a high pressure test cell used for real industrial testing and it is expected that after some modifications it could be implemented in the real oil industry.

The experimental results showed accuracy of a few percent determining the amount of liquid (gas condensate) at the bottom of the high pressure test cell. In addition to that the method used also has the capability to determine refractive index with an approximate accuracy of ± 0.004.

CHAPTER 6

CONCLUSIONS AND FUTURE WORK

The aim of this dissertation was to develop and characterize fiber laser sources based on the erbium doped amplifier for some sensing techniques. The first part of the work was based on the development of a fiber laser for smart, portable and rugged LIBS and dual pulse LIBS fiber optic sensors. A single channel amplifier system suitable for the dual pulse LIBS has been build and successfully demonstrated. A narrow line width DFB laser diode was used as the seed laser diode and its output laser pulse was amplified in a two stage amplifier system. The first stage amplifier was a double pass erbium doped fiber amplifier, in which the double pass amplification was achieved with the help of narrow FBG after the first stage. In the first stage amplification we were able to amplify the input laser pulse with pulse energy of 0.4 nJ to 4 µJ giving an gain of 40 dB. The first stage was characterized with respect to various parameters e. g. input energy and pulse width and ASE output energy were measured versus pump power.

A double clad large node area polarization maintain (LMA-PM) Er/Yb doped fiber was used for the further amplification as the second stage amplifier. The output pulse energy of 46 µJ was achieved after the second stage amplification giving an overall gain of 51 dB. The second stage of the amplification was also characterized by studying various parameters under different operating conditions. Frequency doubling of the output to form a tunable excitation pulse was achieved by focusing the amplified pulse onto a 10 mm long PPLN crystal and its output was further focused onto a BBO crystal for the

frequency quadrupling. In this way we were able to achieve the pulse energies of about 50 μJ for the fundamental pulse (1543 nm), 15 μJ frequency doubled (771.5 nm) and 1 μJ frequency quadrupled (385.7 nm). The onset of SBS pulse generation as a function of repetition rate and pulse width has been investigated and it has been found that the SBS pulse can be controlled by using high repetition rate ($\geq$ 10 KHz) and short seed pulse excitation ($\leq$ 60 ns).

The present laser system was tested in the production of laser breakdown and recording of single pulse LIBS signals. Using iron and silver targets it was demonstrated that good single shot spectra could be recorded in the range of 360 to 400 nm by focusing the fundamental frequency laser pulse on the surface. The system can be applied for the dual pulse LA-LIF application by further separation of UV pulse from the fundamental pulse and delay of this UV pulse in ultraviolet wavelength fiber in order to re-excite a given emission line of the target atomic species after a delay time of the order of 100-200 ns. In future work this two pulse system, one for the excitation and other for the probe, should be implemented to fully demonstrate the ability of a high sensitivity dual pulse LIBS system

In our system the most bulky and costly part is the second stage amplifier with LMA fiber and pump laser system. But the laser system can be further improved by using the optical inline coupler for the LMA fiber instead of pumping with free space optics. In the present system the narrow linewidth probe excitation pulse is used as the seed pulse for the high energy ablation pulse. In this case the synchronization between the probe and ablation pulse is absolutely fixed. However, further optics such as a UV fiber delay line would be required to delay

the excitation pulse by the order of 100 ns until the optimum time for excitation of the atomic species in the ablation plume. In the present system we used a laser diode which has tunability of only a few nm. The tunability range of the excitation pulse can be further increased by using laser diodes with broad tuning range. Telecom short pulse laser diodes are now available with tuning range of 40 nm which gives about 10 nm tunablilty ranges in UV range. The present laser system can be modified further to make it applicable for dual-pulse LIBS. It was shown that even single pulse ablation pulse provides enough emission for recording good quality LIBS spectra. In future work two channel system one for the excitation and other for the probe, should be implemented together with multi-pulse signal accumulation to fully demonstrate ability of dual pulse LIBS.

The second part of the present work was to develop a fiber sensor which can be used in determination of the some important parameters (refractive index, thickness and the phase boundaries conditions etc) useful in the measurement of phase transitions and condensation of hydrocarbon at high temperature and pressures of interest to the oil industries. The fiber sensor developed here is based on the principle of Optical Low Coherence Reflectometry (OLCR). For the development of the fiber sensor an erbium based ASE source was developed and all standard fiber components like fiber couplers, circulators, connectors, single mode fibers and collimators were used. These components are inexpensive and can be easily obtained which makes the system relatively inexpensive and robust.

The experimental results showed accuracy of few percent measurement of volume of liquid at the bottom of the test cell which would be used in determining

the amount of liquid condensate at the bottom of the high pressure test cell. In addition it was shown that the system has the capability to determine refractive index with an approximate accuracy of $\pm$ 0.004. The developed fiber sensor was first tested in the high pressure test cell used for real industrial testing and it is expected that after some modifications it could be implemented in the real tests of hydrocarbon samples.

Before adoption of the developed technique for the industrial applications several other questions should be addressed. Prior to testing a sample the test cell normally is shaken for a significant length of time. Currently the impact of the liquid mercury usually included in the test cell and rigorous shaking of the cell is not known. One of the drawbacks of the current setup is some sensitivity of the correlation signal to the twisting of the optical fibers used in the setup. This drawback originates from the use of the non-polarization maintaining fibers. The use of polarization maintaining fibers should eliminate this problem. The further development of the system should include the following.

1. High pressure test of the optical sensor in operation.
2. Study of the resistance of the optical sensor (grin lens) to the liquid mercury coating.
3. Study of the influence of the use of the polarization maintaining components on the reproducibility of the correlation signal.
4. Development of the software for analyzing of the correlation signal and controlling the setup.
5. Development of a robust design which can withstand rigorous shaking.

162

In conclusion the present thesis has advanced the required laser techniques for implementation of Erbium fiber amplifier technology for applications in dual pulse LIBS and in optical low coherence reflectometry monitoring of phase transitions in high pressure hydrocarbon test cells. Based on the present work the prospects look good for actual implementation of such systems in these application areas.

REFERENCES

1. B B Laud, "Lasers and Non-Linear Optics, second edition" New Age International Limited (2001).

2. D R Siebert, G A West and J J Barrett, Gaseous trace analysis using pulsed photoacoustic Raman spectroscopy", App. Cpt. 19, (1980) 53.

3. H Ransch, Single-Mode Optical Fiber Allows Almost-Lossless Lightwave Transmission
optic News, 10 (1984) 22.

4. F Brench and L Cross, "Optical Microemission Stimulated by a Ruby MASER" Appl. Spectrosc., 16 (1962) 59.

5. E R Runge, R W Minck and F R Bryan, "Spectrochemical analysis using a pulsed laser source" Spectrochim. Acta, B20 (1964) 733.

6. O Samek, D C S Beddows, J Kaiser, S V Kukhlevsky, M Liska, H H Telle and J Young, "Application of laser induced breakdown spectroscopy to in situ analysis of liquid samples" Opt. Eng. 38, (2000) 2248.

7. A K Rai, V N Rai, F Y Yueh and J P Singh, "Trends in Applied Spectroscopy" 4, Research Trends, Trivandrum, India, (2002) p. 165.

8. L J Radziemski and D A Cremers (Eds.)," Laser induced Plasmas and Applications" Marcel Dekker: New York (1989).

9. S Palenco, A Alises, J Cunat, J Baena, J J Laserna, "Development of a portable laser-induced plasma spectrometer with fully-automated operation and quantitative analysis capabilities" J Anal. At. Spectrom. 18, (2003) 933-938.

10. C Gautier, P Fichet, D Menut, J L Lacour, D L Hermite, J Dubessy, "Quantification of the intensity enhancements for the double-pulse laser induced breakdown spectroscopy in the orthogonal beam geometry" Spectrochim. Acta Part B, 60 (2005) 265-276.

11. C Gautier, P Fichet, D Menut, J L Lacour, D L Hermite, J Dubessy, "Study of the double pulse setup with an orthogonal beam geometry for laser-induced breakdown spectroscopy" Spectrochim Acta Part B, 59 (2004) 975-986.

12. L St-Onge, V Detalle and M Sabsabi, "Enhanced laser induced breakdown spectroscopy using the combination of fourth harmonic and fundamental Nd:YAG laser pulses" Spectrochim Acta Part B, 57 (2002) 121-135.

13. J Scaffidi, S M Angel, D A Cremers, "Emission enhancement mechanisms in dual pulse   LIBS" Anal. Chem., 78 (1) 2006 24-32.

14. S L Lui, Y Godwal, M T Taschuk, Y Y Tsui and R Fedosejeves, "Ultra Sensitive detection of   Lead in water using Laser-induced Breakdown spectroscopy with Laser induced   Fluorescence" Analytical Chemistry, 80 pp 1995-2000, 2008.

15. A E Pichahchy, D A Cremers and M J Ferris, "Elemental analysis of metals under water   Using laser-induced breakdown spectroscopy" Spectrochim. Acta B, 52 (1997) 25-39.

16. R Sattmann, V Sturn and R Noll, "Laser-induced breakdown spectroscopy of steel samples   using multiple Q-switch Nd:YAG laser pulses" J Phys. D 28, (1995) 2181-2187.

17. D N Stratis, K L Eland and S M Angel, "Effect of pulse delay time on a pre-ablation dual-   pulse LIBS plasma" Appl. Spectrosc., 55 (2001) 1297-1303.

18. D N Stratis, K L Eland and S M Angel, "Enhancement of Aluminum, Titanium, and Iron in   Glass Using Pre-ablation Spark Dual-Pulse LIBS" Appl. Spectrosc., 54 (2000)1719-1726.

19.   L St. –Onge, M Sabsabi and P Cielo, Analysis of solids using laser-induced plasma spectroscopy in double-pulse mode, Spectrochim. Acta B 53 (1998) 407-415.

20. L St. –Onge, V Detalle and M Sabsabi, "Enhanced laser-induced breakdown spectroscopy using the combination of fourth-harmonic and fundamental Nd:YAG laser pulses"   Spectrochim. Acta B, 57 (2002) 121-135.

21. E H Piepmeier and H V Malmstadt, "Q switched laser energy absorption in the plume of an aluminium alloy" Anal. Chem., 41 (1969) 700-707.

22. R H Scott and A Strasheim, "Laser-induced plasmas for analytical spectroscopy" Spectrochim. Acta Part B, 25 (1970) 311-332.

23. J Zayhowski, "Ultraviolet generation with passively Q-switched microchip lasers" Opt. Lett., 21 (1996) 588-590.

24. T Voss, D Scheel and W Schade, "A microchip-laser-pumped DFB-polymer-dye laser," Appl. Phys Appl. Phys. B, 73 (2001) 105-109.

25. C J Koester and E Snitzer, "Amplification in fiber lasers" Appl. Opt., 10 (1964) 1182-1186.

26. A. Tünnermann, T. Schreiber, F. Röser, A. Liem, S. Höfer, H. Zellmer, S. Nolte and J. Limpert, "The renaissance and bright future of fibre lasers" J. Phys. B: At. Mol. Opt. , Phys. 38, 681-693 (2005).

27. W. Schade, C Bohling, G Holl and M Reuter, "Fiber-optic laser prodder for mine detection and verification, MATEST 2004.

28. S Selvakennedy, M A Mahdi, P Poopalan and H Ahmad, "Pump wavelength's influence in Erbium doped Fiber amplifier performance" ICSE, 98 Proc. Nov. 1998, Bangi, Malaysia, 124-128.

29. Mears R J, "High gain rare earth doped fiber amplifier at 1.54 μm" Proc. Of Optical Fiber comm. Conf., 3 (12) 1987, 167-169.

30. F. Minko, L.Y ad and Chivel, Y.A., J. Opt. Technol., 63, 154, 1996.

31 G. Boardman, A.D., Cresswell, B and Anderson, " An analytical model for the laser ablation of the materials" J. Appl. Surf. Sci., 96-98, 55, 1996.

32. L.J. Radziemski and T.R. Loree., "Laser-Induced Breakdown Spectroscopy: Time-Resolved Spectrochemical Applications" Plasma Chemistry and Plasma Processing, Vol. 1:281 293, (1981).

33. D.A. Cremers and L.J. Radziemski. "Handbook of Laser-Induced Breakdown Spectroscopy" John Wiley & Sons, Ltd., 2006.

34. K. Song, Y.I. Lee and J. Sneddon, "Applications of Laser-Induced Breakdown Spectroscopy" Applied Spectroscopy Reviews, Vol. 32:183- 235, 1997.

35. D.A. Rusak, B.C. Castle, B.W. Smith and J.C. Winefordner, "Recent Trends and the future of laser-induced plasma spectroscopy" Trends in Analytical Chemistry, Vol. 17: 453-461, 1998.

36. J.C. Miller and R.F. Haglund. "Laser Ablation and Desorption" Academic Press, San Diego, California, 1998.

37. O N Krokhin in Laser Handbook, vol.2 ed. F T Arecchi and E O Schulz-duBois, Amsterdam, North Holland, 1972, pp 1371.

38. Annemie Bogaerts,Zhaoyang Chen, Renaat Gijbels and Akos Vertes, "Laser ablation for analytical sampling: what can we learn from modeling?" Spectrochimica Acta Part B- Atomic Spectroscopy, 58:1867- 1893, 2003.

39.   Laszlo Balazs, Renaat Gijbels and Akos Vertes, "Expansion of laser-generated plumes near the plasma ignition threshold" Analytical Chemistry, Vol. 63:314- 320, 1991.

40. Majidi V. and Joseph M.R, "Spectroscopic Applications of Laser-Induced Plasmas" Critical Reviews in Analytical Chemistry, 23:143-162, 1992.

41. Y I Lee, Y J Yoo and J Sneddon, Spectrosc. 13 (1998) 14.

42.   R. Knopp, F J Scherbaum and J I Kim, "Laser induced breakdown spectrometry (LIBS) as an analytical tool for the detection of metal ions in aqueous solution" Fresenius Journal of Analytical Chemistry, 335 (1996) 16-20.

43. J O Caceres, J Tornero Lopez, H H Telle and A Gonzalez Urena, Quantitative analysis of trace metal ions in ice using laser-induced breakdown spectroscopySpectrochimica Acta B, 56 (2001) 831-838.

44. L. J. Radziemski, T. R. Loree, D. A. Cremers, and N. M. Hoffman, "Time-resolved laser-induced breakdown spectrometry of aerosols," Anal. Chem. 55, 1246-1252 (1983).

45. U Panne, R.E. Neuhauser, M. Theisen, H. Fink and R. Niessner, "Analysis of heavy metal aerosols on filters by laser-induced plasma spectroscopy" Spectrochimica Acta B, 56 (2001) 839-850.

46. D Body and B L Chadwick, "Optimization of the spectral data processing in a LIBS simultaneous elemental analysis system" Spectrochimica Acta B 56 (2001) 725-736.

47. D A Cremers, R C Wiens, M J Ferris, R Brennetot and S Maurice, "Capabilities of LIBS for analysis of geological samples at stand-off distances in a Mars atmosphere". In: Trends in Optics and Photonics (TOPS) – Laser Induced Plasma Spectroscopy and Applications. Technical Digest, **81**. Optical Society of America, 5–7.

48. R.S. Harmon F. C. Delucia, C. E. McManus, N. J. McMillan, T. F. Jenkins, M. E. Walsh, and A. Miziolek, "Laser-induced breakdown spectroscopy: an emerging chemical sensor technology for real-time field-portable, geochemical, mineralogical, and environmental applications," Applied Geochemistry 21 (2006) 730–747.

49. D.A. Cremers J. Sca_di and S.M. Angel, "Emission enhancement mechanisms in dual-pulse LIBS" Anal. Chem., Vol. 78:24- 32, 2006.

50. J. Uebbing, J. Brust,W. Sdorra, F. Leis and K. Niemax, "Reheating of a laser produced plasma by a second pulse laser" Applied Spectroscopy, Vol. 45:1419-1423, 1991.

51. D.N. Stratis, K.L. Eland and S.M. Angel, "Dual-pulse LIBS using a preablation spark for enhanced ablation and emission" Appl. Spectrosc., Vol. 54:1270-1274, 2000.

52. C. Gautier, P. Fichet, D. Menut, J.L. Lacour, D.L Hermite and J. Dubessy," Quantification of Intensity enhancements for double-pulse laser-induced breakdown spectroscopy in orthogonal beam geometry" Spectrochimica Acta B, Vol. 60: 265-276, 2005.

53. J Scaffidi, J Pender, W Pearman, S R Goode, B W Colston Jr., J C Varter and S M Angel, "Dual pulse laser induced breakdown spectroscopy with combinations of femtosecond and nanosecond laser pulses" Appl. Opt. 42 (2003) 6099-6106.

54. V N Rai, F-Y Yueh and J P Singh, "Study of Laser-Induced Breakdown Emission From Liquid Under Double-Pulse Excitation" Appl. Opt., 42 (2003) 588.

55. Koester, C. J. and Snitzer E, "Amplification in a fiber laser" Appl. Opt., 3 (1963) 1182-1186.

56. Snitzer E," Neodymium glass laser" Proc. 3rd Int. Conf. on Solid state Lasers, Paris (1963) 999-1019.

57. J Limbert, T Schreiber, S Notle, H Zellmer and A Tunnermann, Optical Express, 11, 24 (2003), 3332.

58. S Selvakennedy, M A Mahdi, P Poopalan and H Ahmad, "Pump wavelength's influence in Erbium doped Fiber amplifier performance" ICSE, 98 Proc. Nov. 1998, Bangi, Malaysia,124-128.

59. Randy Giles and Tingye Li, "Optical amplifiers transform long distance lightwave telecommunications" Fellow IEEE, vol.84 no.6 (1996) 870-883.

60. C R Giles, E Desurvire and J. L. Zyskind, :"Noise performance of erbium doped fiber Amplifier pumped at 1.49μm, and application to signal prea,plification at 1.8 Gbits/s" IEEE   Photonics Technol. Letters, vol.1 No.11 (1989) 367-369.

61. C R Giles and E Desurvire, "Modeling Erbium doped fiber amplifers" Journal of Lightwave Technology, Vol.9 No.1 (1991) 271-283.

62. Mears R J, "High gain rare earth doped fiber amplifier at 1.54µm" Proc. Of Optical Fiber comm. Conf., 3 (12) 1987, 167-169.

63. Desurvire E, "Erbium doped fiber amplifier: Principles and Applications" John Wiley and Sons, Inc. New York (1994).

64. Lou Qi houg and Zhou Jun,"High power fiber lasers" Front. Phys. China, 2 (2007) 410-423.

65. Mears R J, Reekie L, Jauncey I M and Payne D N (1988), "Optical fiber amplifiers for 1.5µm operation" Proceedings of the Optical Fiber Comm., Conf. pp 3-5.

66. Becker P C, "Erbium doped fiber amplifiers Fundamentals and technology" Acad. Press (2002).

67. Grzegorz Sobon, Pawel Kaczmarek and Krzysztof M Abramski, "Erbium-ytterbium co-doped fiber amplifier operating at 1550 nm with stimulating lasing at 1064 nm" Optics Commun., 285 (2012) 1929-1933.

68. Federighi M and Di Pasquale F, "The effect of pair-induced energy transfer on the performance of silica waveguide amplifiers with high Er3+/Yb3+ concentrations" IEEE Photonics Technol Lett, (1995); 7 303-5.

69. Willimas L Barnes, Richard I Laming, Eleanor J Tarbox and P R Morkel, "Absorption and Emission cross sections of Er^{3+} doped silica fibers" IEEE J. Quantum Electronics vo. 27, No.4 (1991).

70. D E McCumber, "Theory of phonon-terminated optical masers," Phys. Rev. 134, A299 (1964).

71. W J Miniscalco and R S Quimby, "General procedure for the analysis of Er^{3+} cross sections" Opt. Lett. 16, 258 (1991).

72. Rosolem J B and Juriollo A A, "S Band EDFA using standard Erbium doped Fiber, 1450 nm pumping and Single Stage ASE Filtering" Int. Conf. Comm. Newt. Prof., 1-3.

73. Naji A W, Abidin M S Z, Kassir A M, Al-Mansoori M H, Abdullah M K and Mahdi M A, "Trade-off between single and double pass amplification schemes of 1480 nm pumped EDFA" J. Microw Opt. Tech. Lett., 43 (1): 38-40 (2004).

74.   Hidehiko Takara, Atushi Takada and Masatoshi Saruwatari, "A highly efficient two stage Er^{3+} doped optical fiber amplifier employing an optical gate to effectively reduce ASE" (1992).

75. B Desthieux, R I Laming and D N Payne, "111KW (0.5mJ) pulse amplification of 1.5 µm using a gated cascade of three erbium doped fiber amplifiers" Appl. Phys. Lett., 63 (1993)   (5).

76. Franken P A, Hill A E, Peters C W and Weinreich G, "Generation of optical harmonics" Phys. Rev. Lett. 7, (1961) 118-119.

77. Bloembergen N, "Wave propagation in nonlinear electromagnetic media" Proc. IEEE, 51 (1963) 124-131.

78. Franken P A and Ward J F, "Optical Harmonics and Nonlinear Phenomena" Rev. Mod. Phys., 35 (1963) 23.

79. R W Byod, "Nonlinear Optics" Academic Press, San Diego, 1992.

80. M V Hobden and J Warner, "The temperature dependence of the refractive indices of pure lithium niobate," Phys. Lett. 22, (1996) 243.

81. J. A. Armstrong, "Interactions between light waves in a nonlinear dielectric", Phys. Rev. 127 (6) 1918 (1962).

82. M Yamada, N Nada, M Saitoh and K Watanabe, "First-order quasi-phase matched LiNbO3 waveguide periodically poled by applying an external field for efficient blue second-harmonic generation," Appl. Phys. Lett., 62 (1993) 435.

83. E Lichtman, A A Friesem, R G Waarts and H H Yaffe, "Stimulated Brillouin scattering excited by two pump waves in single-mode fibers" J. Opt. Sco. Am. B,, 4 (1987) 1397.

84. Y Azuma, N Shibata, T Horiguchi and M Tateda, Electron. Lett. 24, 250 (1988).

85. R G Smith, "Optical Power Handling Capacity of Low Loss Optical Fibers as Determined by Stimulated Raman and Brillouin Scattering" Appl. Opt. 11, 2489-2494 (1972).

86. M. O. van Deventer and A. J. Boot, "Polarization properties of stimulated Brillouin scattering in single-mode fibers," J. Lightwave Technol. 12, 585-590 (1994).

87. L Mandel and E Wolf, "Optical Coherence and Quantum Optics" pp. 147-155, Cambridge University Press, Cambridge, England (1995).

88. C. R. Giles, "Lightwave Applications of Fiber Bragg Gratings," Journal of Lightwave Technology, vol. 15, No. 8, 1997.

89. K Takada, I Yokohama, K chida and J Noda, "New measurement system for fault location in optical waveguide devices based on an interferometric technique" Appl. Opt.,26, 1603-1606 (1987).

90. R C Youngquist, S Carr and D E N Davies, "Optical coherence domain reflectrometry" a new optical evaluation technique, Opt. Lett. 12, 158-160 (1987).

91. T Kubota, M Nara and T Yoshino, "Interferometer for measuring displacement and distance" Opt. Lett. 12, 310-312 (1987).

92. R C Youngquist, S Carr and D E N Davies, "Optical coherence domain reflectrometry, a new optical evaluation technique" Opt. Lett. 12, 158-160 (1987).

93. R P Novak, H H Gilgen, P Beaud and W Hodel, "Comparison between OTDR and OLCR with micrometer spatial resolution" Technical Digest of Symposium on Optical Fiber Measurement, Vol. 792, p 35 (1990).

94. D. Derickson, "Fiber Optic Test and Measurement" Prentice Hall PTR (1998).

95. B L Danielson and C D Whittenberg, "Guided-wave reflectometry with micrometer Resolution" Appl. Opt., vol. 26, p.2836-2842 (1987).

96. K Takada, K Yukimatsu, M Kobayashi and J Noda, "Rayleigh backscattering measurement of single mode fibers by low coherence optical time domain reflectometer with 14 μm spatial resolution" Appl. Phys. Lett., Vol. 59, p 143 (1991).

97. B L Danielson and C Y Boisrobert, "Absolute optical ranging using low coherence Interferometry" Appl. Opt. vol. 30, p 2975, (1991).

98. R Bohm and R Ulrich, "High accuracy fiber optic refractometer for fluids" Opt. Fiber Conf.- 7, Sydney, Australia, (1990) p 353.

99. C S Wang, W H Cheng, C J Huang, W K Burns and R Moeller, "High power low divergence superradiant diode" Appl. Phys. Lett., 41, 587 (1982).

100. H Ghafoori-Shiraz and T Okoshi, "Optical frequency domain Reflectometry" Opt. Quantum Electron., 18, 265-272 (1986).

101 . http://oequest.com/getproduct/18508/cat/1387/page/2

102 . http://www.teamwavelength.com/products/product.asp?part=5

103 . http://www.Fiteltech.com/pumplasers

104. Fibercore limited, http://www.fibercore.com

105. http://thorlabs.com/thorProduct.cfm?partNumber=6015-3

106. O/E Land Inc, Quebec Canada, http://www.o-eland.com

107 . http://www.afwtechnologies.com.au/band_pass_filter.html

108. Fiberlign, Nepean, Ontario, Canada.

109 . http://www.limo.de

110. http://www.newport.com/MS260i153-1-4-m-Imaging-Spectrograph/378347/1033/info.aspx

111 . http://www.andor-tech.com.

112. http://www.oceanoptics.com/products/nirquest.asp

113. E Desurvire, C R Giles and J R Simpson, "Gain Saturation in effects in high speed, multi channel erbium-doped fiber amplifier at 1.53 μm" J. Lightwave Technol., 7 (1989) 2095-2104.

114. C R Giles and D DiGiovanni, "Spectral dependence of gain and noise in erbium doped fiber amplifiers" IEEE Photon. Technol. Lett., 1 (1990) 797-800.

115. B Bouzid, M B Ali and M K Abdullah, "A high gain EDFA design using double pass amplification with a band pass filter" IEEE Photon. Technol. Lett., 5 (2003) 1195-1197.

116. S S Pathmanathan, H A Abdul-Rashid and P K Choudhury, "An experimental investigation   of double pass erbium doped optical amplifier with tunable band pass filter" Asian J. Phys.,   17(2008) 241-244.

117. H Meng, Y Liu, W Gao, H Zhang, s Yuan and X Dong, Microwave Opt. Technol. Lett. 36 (6) (2003) 510-503.

118. J cames A, S Mendoza V, E Kuzin, O Pottiez, C Garcia L and R Vazquez S, "High gain erbium doped fiber amplifier for the investigation of nonlinear processes in fibers" Optical Fiber Technology, 14 (2008) 237-241.

119. C R Giles, "Suppression of polarization holeburning-induced gain anisotropy in reflective EDFAs" Electron Lett., 30 (1994) 976-977.

120. V lauridsen, R Tadayoni, A Bjarklev, J H Povlsen, B Pedersen, "Gain and noise performance of fiber amplifiers operating in new pump configurations" Electron. Lett., 27 (1991) 327-329.

121. A Takada, K Iwatsuki and M saruwatari, "Picosecond laser diode pulse amplification upto 12W by laser diode pumped Erbium doped fiber" IEEE Photon. Technol. Lett., vol2 pp 122-124 (1990).

122. S S Pathmanathan, S Z Muhd-Yassin, H A Abdul-Rashid and P K Choudhury, "An experimental investigation of the gain spectrum of erbium-doped fiber amplifiers under various system configurations" Optik 121 (2010) 184-187.

123. Joon Tae Ahn, Min-Yong Jeon and Kyong Hon Kim, "Two stage reflective type erbium doped fiber amplifier with enhanced noise figure characteristics" Optics Communications, 197 (2001) 121-125.

124. Yeh C H, Lee C C and Chi S, "S-plus C-band erbium doped fiber amplifier in parallel structure" Opt. Commun, 2004, 241.

125. M Stephen, M Krainak, H Riris and G R Allan, "Narrowband, tunable, frequency doubled erbium doped fiber amplified transmitter" Opt. Lett., 32 (2007) 2073-2075.

126. C E Diley, M A Stephen and M P Savage-Leuchs, "High SBS-threshold, narrowband, erbium co-doped with ytterbium fiber amplifier pulses frequency doubled to 770 nm" Opt. Express, 15 14389-14395 (2007).

127. G P Agarwal, "Nonlinear Fiber Optics" Third Edition, (Academic, 2001).

128. .R G Smith, "Optical Power Handling Capacity of Low Loss Optical Fibers as Determined by Stimulated Raman and Brillouin Scattering" Appl. Opt., 11 (1972) 2489.

129 . D Neshev, I Velchev and W A Majevski, "SBS-pulse compression to 200 ps in a compact single cell setup" Appl. Phys. B, 68 (1999) 671-675.

130. M Laroche, H Gilles and S Girard, "High peak power nanosecond pulse generation by stimulated Brillouin scattering pulse compression in a seeded Yb-doped fiber amplifier" Optics Lett., 36 (2011) 241-243.

131. N G R Broderick, H L Offerhaus, D J Richardson and R A Sammut, "Power Scaling in Passively Mode-Locked Large-Mode Area Fiber Lasers" IEEE Photon. Technol. Lett., 10 (1998) 1718.

132. J Cames A, S Mendoza V, E Kuzin, O Pottiez, C Garcia L and R Vazquez S, "High gain erbium doped fiber amplifier for the investigation of nonlinear processes in fibers" Optical Fiber Technology, 14 (2008) 237-241.

133. H Takara, A Takada and M Saruwatari, "A highly efficient two stage Er^{3+} doped optical fiber amplifier employing an optical gate to effectively reduce ASE" IEEE Photonics Technol. Lett. , 43 (1992) 241-243.

134. M Yamada, N Nada, M Saitoh and K Watanabe, "First-order quasi-phase matched LiNbO3 waveguide periodically poled by applying an external field for efficient blue second-harmonic generation" Appl. Phys. Lett., 62, 435-436 (1993).

135. W K Burns, W McElhanon and L Goldberg, "Second harmonic generation in field poled, quasi-pahse-matched, bulk LiNbO3" IEEE photon. Technol. Lett., 6 (1994) 252-254.

136. Movva Sai Krishna, U S Tripathi, Ashok Kaul, K Thyagarajan and M R Shenoy, "Temperature tuning characteristics of periodically poled Lithium Niobate for secomd harmonic generation at 490 nm."

137. M A Arbore, M M Fejer, M E Fermann, A Hariharan, A Galvanauskas and D Harter, "Frequency doubling of femtosecond erbium fiber sloiton lasers in periodically poled lithium niobate" Optics Letters, 22 (1997) 13-15.

138 . Zhang Shuang Gen, Yao Jiang Hong, Shi Qing, Liu Yan Ge, Li Yong Nan, Tu Cheng Hou, Guo wen Gang and Lu Fu Yun, "Fiber format photonic source based on efficient frequency doubling of cw Erbium fiber laser amplifier" Chin. Phys. Lett., 25 (2008) 2873-2875.

139. R J Thompson, M Tu, D C Aveline, N Lundblad and L Maleki, "High power single frequency 780 nm laser source generated from frequency doubling of a seeded fiber amplifier in a cascade PPLN crystals" Optics Express, 11 (2003) 1709-1713.

140. http://www.newport.com/818-Series-Low-Power-Calibrated-Photodiode-Sensors/827082/1033/info.aspx.

141. Xiuwei Fan, Haitao Huang, Jijian Jiang and Jingliang He, "Generation of UV radiation at 335.5nm based on frequency quadrupling of a diode pumped Nd:YVO4 laser" Chinese Optics Letters, 6 (2008) 192-194.

142 . http://physics.nist.gov/cgi-bin/ASD/lines1.pl

143. Godwal, Yogesh, "Laser Ablation Laser Induced Fluorescence for the Sensitive Detection of Heavy Metals in Water" PhD thesis, University of Alberta (2010).

144. Chung E Lee and Henry F Taylor, Fellow, IEEE, "Fiber Optic Fabry-Perot Temperature sensor using a Low coherence light source" Journal of Light wave technology, vol. 9, N. 1 (1991) 129.

145. Hepler L G and Smoth R G, "The Alberta oil sands: industrial procedures for extraction and some recent fundamental research" Edmonton: Alberta Oil Sands technology and Research Authority (AOSTRA), 1994.

146. Annual book of ASTM standards, Philadelphia: American Society for Testing and Materials (ASTM), 1993.

147. Nottingk BE: Instrumentation reference book, 2nd ed. London: Butterworths; 1995.

148. Chiu M H, Lee J Y and Su DC, "Refractive-index measurement based on the effects of total internal reflection and the uses of heterodyne interferometry" Appl Opt, 36 (1997) 2936-9.

149. Shedd T A and Newell T A, "Automated optical liquid film thickness measurement method" Rev. Sci. Instrum, 69 (1998) 4205-13.

150. Jaaskelainen A, Silvennoinen R and Peiponen K E, Raty, "On measurements of complex refractive index of liquids by diffractive element based sensor" J. Opt. Commun, 178 (2000) 153-7.

151. Rogerio T Ramos, Andrew Holmes, Xu Wu and Elizabeth Dussan, "A Local optical probe using fluorescence and reflectance for measurement of volume fractions in multi-phase flows" Meas. Sci. Technol., 12 (2001) 871-876.

152. Weize Wu, Jie Ke and Martyn Poliakoff, "New design of fiber-optic reflectometer for determining the phase boundary of multicomponent fluid mixtures at high pressures and high temperatures" Review of Scientific Instruments, 77, 2006.

153. Mikhail V. Avdeev, Aleksei N. Konovalov, Viktor. N. Bagratashvili, Vladimir K. Popov, Svetlana I. Tsypina, Maia Sokolova, Jie Keb and Martyn Poliakoff, "The fibre optic reflectometer: A new and simple probe for refractive index and phase separation measurements in gases, liquids and supercritical fluids" Phys. Chem. Phys, 6, (2004) 1258-1263.

154. Weatherford Laboratories Ltd., Calgary, WWW.weatherfordlabs.com